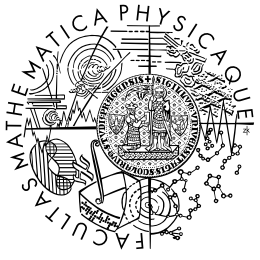

FACULTY
OF MATHEMATICS
AND PHYSICS
Charles University

DOCTORAL THESIS

Jakub Benda

Astrophysically important processes in collisions of electrons with hydrogen atoms

Institute of Theoretical Physics

Supervisor of the doctoral thesis:	RNDr. Karel Houfek, PhD.
Study programme:	Physics
Study branch:	Theoretical physics, astronomy and astrophysics

Prague 2017

I declare that I carried out this doctoral thesis independently, and only with the cited sources, literature and other professional sources.

I understand that my work relates to the rights and obligations under the Act No. 121/2000 Sb., the Copyright Act, as amended, in particular the fact that the Charles University has the right to conclude a license agreement on the use of this work as a school work pursuant to Section 60 subsection 1 of the Copyright Act.

In Prague on 23 June 2017

Jakub Benda

Title: Astrophysically important processes in collisions of electrons with hydrogen atoms
Author: Jakub Benda
Department: Institute of Theoretical Physics
Supervisor: RNDr. Karel Houfek, PhD.
Supervisor's e-mail address: karel.houfek@mff.cuni.cz

Abstract: This thesis focuses on calculations of the cross sections and other scattering quantities that characterize the outcome of collisions of electrons with hydrogen atoms. For the chosen energy range and atomic transitions the scattering process is solved within the non-relativistic quantum mechanics by discretization of the Schrödinger equation in the basis of B-splines, which transforms the equation into a linear-algebraic problem. The thesis discusses the boundary conditions, methods of solution of the linear system, preconditioning of the system and interpretation of results, including several original ideas that proved to be very beneficient for the calculations. The calculated data are provided by means of graphs at the end of the thesis. Also, a custom web-based scattering database containing the results has been set up, freely available to the expected audience of this project.

Keywords: electron scattering, atomic hydrogen, exterior complex scaling

Contents

Contents **5**

1 Introduction **13**

2 Physical description **17**
2.1 Physical approximations . . . 17
2.2 Hydrogen atom . . . 18
2.3 Scattering problem description . . . 18
2.4 Separation of spin and spin flip . . . 20
2.5 Arbitrary impact angle scattering . . . 22
2.6 Accidental degeneracy and fine structure transitions . . . 22
2.7 Ionization . . . 24

3 Design of the Hex package **27**
3.1 Hex modules . . . 27
3.2 Database structure . . . 28
3.3 VAMDC connection . . . 29

4 Hex-ecs: The low-energy program **33**
4.1 Theory . . . 33
4.1.1 Angular momentum expansion . . . 33
4.1.2 Exterior complex scaling . . . 36
4.1.3 B-spline basis . . . 39
4.1.4 Extraction of scattering information . . . 41
4.2 Implementation . . . 42
4.2.1 Solution of the linear system . . . 42
4.2.2 Preconditioning . . . 42
4.2.3 Kronecker product approximation preconditioner . . . 43
4.2.4 Preconditioner performance . . . 44
4.2.5 Parallelization . . . 46
4.3 Radial convergence . . . 47
4.3.1 *S*-model . . . 48
4.3.2 Higher angular momenta . . . 48
4.3.3 Potential splitting . . . 49
4.3.4 Extrapolation . . . 49
4.3.5 Channel reduction . . . 49
4.3.6 Domain decomposition . . . 55

5 Hex-db: Database interface **63**
5.1 Scattering T-matrices . . . 63
5.2 Derived scattering quantities . . . 64
5.3 Interpolation . . . 66

6 Results **67**
6.1 Scattering lengths . . . 67
6.2 S-wave model . . . 68
6.3 Resonances . . . 70
6.4 Results below the threshold $n = 2$ . . . 70
6.5 Results between $n = 2$ and $n = 3$ thresholds . . . 71
6.6 Between $n = 3$ and $n = 4$ thresholds . . . 76
6.7 Higher energies . . . 76
6.8 Differential cross section . . . 76
6.9 Validation of new results against existing data . . . 85

7 Conclusion **95**

Appendices **97**

A Chebyshev integration **99**

B Hex-ecs command line parameters **103**

C Hex-ecs input file **107**

Bibliography **111**

Index **116**

List of publications

Benda J., Houfek K., *Hydrogen–Electron Scattering for Astrophysical Applications*, in Šafránková J., Pavlů J., (Eds.), *WDS'13 Proceedings of Contributed Papers*, Part III – Physics, p. 19–24, Matfyzpress, Prague 2013, ISBN 978-80-7378-252-8.

Benda J., Houfek K., *Collisions of electrons with hydrogen atoms I. Package outline and high energy code*, Comput. Phys. Commun. **185** (2014), p. 2893–2902.

Benda J., Houfek K., *Collisions of electrons with hydrogen atoms II. Low-energy program using the method of the exterior complex scaling*, Comput. Phys. Commun. **185** (2014), p. 2903–2912.

Benda J., Houfek K., *New version of hex-ecs, the B-spline implementation of exterior complex scaling method for solution of electron–hydrogen scattering*, Comput. Phys. Commun. **204** (2016), p. 216–217.

Benda J., Houfek K., *Reducing the dimensionality of grid based methods for electron-atom scattering calculations below ionization threshold*, Comput. Phys. Commun. **213** (2017), p. 46–51.

Benda J., Houfek K., *Converged and consistent high-resolution low-energy electron-hydrogen scattering. I. Data below $n = 4$ threshold for applications in stellar physics*, At. Data Nucl. Data Tables **117?** (2017), p. ?–?.

Benda J., Houfek K., *Quantum collisions of electrons with hydrogen atoms*, in Pešatová K., Poláková B., Cawley J., (Eds.), *Supercomputing in Science and Engineering*, p. 210–212, IT4Innovations National Supercomputing Center, 2017, ISBN 978-80-248-4037-6.

Acknowledgements

There had been hardly any doctoral thesis finished just through the diligence of its solver. For each such single finished project there are dozens of people and institutions that participated, whether by directly helping out with a topic, or by providing access to information, to computational resources or funds, by creating a positive working atmosphere, offering interest and explicit support or just simple patience with the busy investigator. I could fill all these categories with lists of names.

My deepest thanks go to my family, which not only always tolerated, but even supported my obsession with science; to my great supervisor Karel Houfek, who was always in mood for discussion, and who gracefully steered my way through the post-graduate world; to my friends, and to the colleagues in the company where I work.

I had a great time twice visiting one of the most renowned atomic physics groups in the world—that of Andris Stelbovics, Igor Bray, Dmitry Fursa and Alisher Kadyrov at the Curtin University in Perth. I am greatly indebted to them for all warm and selfless support and for the opportunity to see how physics is done on the other side of the planet!

Finally, I would like to thank to Metacentrum, CERIT-SC and IT4Innovations for providing the computational resources and to the Grant Agency of the Charles University for supporting this project financially.

Nomenclature

A	matrix (sans serif)
$\mathbf{r}$	vector (bold face)
σ	cross section; spin state
n	principal quantum number (n_i initial, n_f final)
l	orbital quantum number; general angular momentum
m	magnetic quantum number
s	spin state (projection)
μ	reduced mass; combined projection of spin and orbital momentum
$\mathbf{k}$	wave vector
L	total angular momentum quantum number
M	total angular momentum projection
S	total spin projection
ℓ	angular momentum of a single electron
P_{nl}	regular hydrogen radial orbital, $P_{nl}(r) = rR_{nl}(r)$
$\hat{j}_l$	regular Riccati-Bessel function of the first kind, $\hat{j}_l(x) = xj_l(x) = \sqrt{\frac{\pi x}{2}} J_{l+1/2}(x)$
Ω	solid angle; collision strength
H	hydrogen atom
H	hamiltonian

Chapter 1

Introduction

The problem of collision of an electron with an isolated hydrogen atom has been a test bed of atomic physics for almost a century due to its outstanding simplicity and hence possibility of application of various direct methods of description and solution. Still, the underlying problem is a three-particle process and the dynamics of its constituents is unsolvable in a closed form both within the classical and quantum mechanics.

The area of application of the quantum electron-hydrogen scattering calculations lies mainly in the plasma physics. Stellar atmospheres contain free hydrogen atoms kept by the electromagnetic radiation from recombining into molecules, as well as the free electrons, whether slow—thermal—or fast—accelerated by magnetohydrodynamic forces in flare events. The effects of individual collisions resulting in excitations and de-excitations then combine to average level populations and to a big picture that manifests as a shape or polarization of spectral lines [1], [2], [3], [4].

Another astrophysical setting where the electron-hydrogen scattering plays a distinguished part is the cooling of the interstellar gas in the evolution of the Universe. The coupling between the gas temperature, radiation temperature and electron temperature were of different importance throughout the history and in some epochs the cooling of the interstellar gas by free electrons significantly contributed to the overall cooling rate. The interaction that coupled the temperatures of these two media was the low-energy spin-flip process [5], which is also discussed in this thesis.

Particularly in the astrophysical case the medium can be very thin and recombination unlikely. Low density is both an advantage and a disadvantage. On the one hand the interaction between atoms can be disregarded, which tremendously simplifies the description and solution of the system, effectively making the atom isolated. On the other hand, it also allows long-term existence of highly excited (Rydberg) states of the atoms. Such atoms then effectively span much larger space, making their numerical simulation even more challenging.

But collisions of electrons with hydrogen atoms and its isotopes have also industrial use. Neutral hydrogen beams are used for diagnostic purposes in the thermonuclear reactors. The application is done by injecting hydrogen gas into the working plasma, which is nothing else than a mixture of electrons and nuclei of hydrogen isotopes with traces of other elements. Collisions of the plasma with the neutral beam produce radiation, which can be analyzed and serves as another probe into the inner dynamics of the working gas [6], [7]. The importance of this topic can be well illustrated by the fact that the International Atomic Energy Agency (IAEA) regularly opens Coordinated Research Projects (CRPs) that include the topic of electrons colliding with hydrogen isotopes in the environment of the thermonuclear reactor, for example:

- 2009–2015 **CRP F43018**
  Light Element Atom, Molecule and Radical Behaviour in the Divertor and Edge Plasma Regions

- 2017–2021 **CRP F43023**
  Data for Atomic Processes Related to Neutral Beams in Fusion Plasma

The task of this thesis has been to collect, refine and employ several existing numerical methods, so that the scattering problem can be solved for:

1. *Most processes that can occur in the electron-hydrogen collisions*
   This includes the elastic scattering

   $$\mathrm{H}(n,l,m) + e^-(\mathbf{k}_i) \to \mathrm{H}(n,l,m) + e^-(\mathbf{k}_f)\,, \qquad |\mathbf{k}_i| = |\mathbf{k}_f|\,,$$

   excitation (or spin flip)

   $$\mathrm{H}(n_i,l_i,m_i,s_i) + e^-(\mathbf{k}_i,\sigma_i) \to \mathrm{H}(n_f,l_f,m_f,s_f) + e^-(\mathbf{k}_f,\sigma_f)\,,$$

   and fragmentation (ionization)

   $$\mathrm{H}(n_i,l_i,m_i) + e^-(\mathbf{k}_i) \to p^+(\mathbf{K}) + e^-(\mathbf{k}_1) + e^-(\mathbf{k}_2)\,.$$

   In general, the scattering system should also be coupled to the electromagnetic field, allowing for radiative processes like photo-ionization, radiative attachment, or even Bremsstrahlung at higher energies. These processes were not considered in this work.

2. *Broad range of energies*
   The electron in the hydrogen atom can be stripped by projectile with impact energy greater than the ionization threshold, which is approximately 13.6 eV. This energy marks a boundary between the resonant low-energy scattering and intermediate-to-high-energy scattering. Coverage of a considerable surrounding of this transition energy to both directions is necessary. Both regions are complicated: The resonant region requires fine sampling of the impact energy parameter, so that the resonances are represented in a sufficient detail, whereas the high energy region requires careful handling of rapidly oscillating wave functions.

The ultimate goal of this project is to build as complete database of electron-hydrogen scattering cross sections as possible, so that it can be used in the applications by astrophysicists and plasma physicists. Moreover, the accuracy of the produced results should be superior to the presently available data; the estimated error should not exceed 5 %.

Similar effort had been exerted before by several researchers and currently there is a large body of data already present to compare with. Still, the desired degree of completeness had not yet been achieved, as the available data exist just for a specific selection of energies, for transitions between the lowest atomic states and only for some of the possible processes. While the fundamental theory of the electron-hydrogen collisions is very straightforward, the long-range character of the inter-particle forces prevented (and to some degree still prevents) a direct numerical solution of the equation of motion of the system—the Schrödinger equation—for all possible initial and final configurations of the two electrons involved.

The first noteworthy collection of accurate elastic and non-elastic data is due to Callaway [8], who used the straightforward close-coupling calculation with a handful of

states to calculate the cross sections for the transitions $1s-1s$, $1s-2s$ and $1s-2p$. Even though only total angular momenta $L \leq 3$ were included in the calculation, they are remarkably accurate and compare well with more recent calculations. The following calculation by the same author [9] presented for the first time the cross sections for scattering on excited states.

Aggarwal *et al* [10] published collision-strength datasets for all transitions $n \to n'$, where $n \leq n'$, $n' = 1, 2, 3, 4$, at energies from the transition threshold to a few electron-volts above the ionization threshold. Their data are very finely sampled and contain a large amount of physical resonances, which have correct positions. In the review by Callaway [11] the accuracy of [10] has been disputed, mentioning the omission of the continuum channels from the R-matrix basis as a possible cause for discrepancies.

Another recalculation of the three lowest transitions $1s-1s$, $1s-2s$ and $1s-2p$ between the $n = 2$ and $n = 3$ thresholds has been done by Bartschat [12] using the R-matrix with pseudo-states (RMPS) method. These data were compared to the results of the converged close-coupling method (CCC, [13]) and belong currently among the reference data for electron-hydrogen scattering.

Anderson *et al* [14] used the RMPS method to calculate the cross sections for transitions $n, l \to n', l'$, where $n < n'$, with the aim to produce relevant data for fusion plasma simulations. They used 15 physical states, 24 pseudo-states and $R_A = 140\, a_0$ as the radius of the inner region. However, this radius is not appropriate for transitions between highly excited states.

Bartlett [15] calculated the cross sections for transitions from the ground state to all $n = 3$ states at a small range of energies to demonstrate the accuracy of the propagating exterior complex-scaling (PECS) method.

To sum up, some of the existing publications focus on providing rich variety of datasets, some focus on accuracy of the results for a few particular transitions, some illustrate an efficient solution method, but none of them does really combine all these viewpoints together, with explicit consideration of consistency of the datasets and their good convergence.

There are also a few on-line databases that contain the scattering data of interest. The most comprehensive is the dataset in the Aladdin database [16] calculated by Bray and Stelbovics [17] using the CCC method. Their data for elastic transitions are in perfect agreement with [12], but according to the information in Aladdin the same calculation setup has been used for higher transitions (up to $n = 4$), which raises doubts, whether they are sufficiently converged with respect to the basis size. Some, mainly elastic data are contained in LXcat database [18]. Another database is that of NIST [19], which contains only optically allowed transitions from the ground state (up to $n = 10$), produced by BE-scaling of the plane wave Born approximation results [20], [21]. NIST data are not meant for the low-energy usage and there are very few points below the ionization threshold, if any. There is also another database by NIST [22] containing ground state elastic data produced by Salvat *et al* [23], based on the Dirac equation with a model potential.

Chapter 2

Physical description

This opening chapter is devoted to a summary of the basic physical and formal concepts used further. The electron-hydrogen scattering problem is solved by a time-independent quantum-mechanical method, which—depending on the particular method employed—provides either directly the scattering statistical quantities, or a stationary scattering wave function, from which the data can be extracted. Even though this thesis contains mostly low-energy results, presented in the last chapter, the long-term intent of the project is to cover all scattering energies from zero impact velocity to the region where first Born approximation yields satisfactory results, which is around 1 keV. The physical model must be such as to allow valid description for all these energies.

The first section of this chapter presents the physical approximations used, consistent with the aim of 5 % accuracy. The second chapter deals with hydrogen eigenstates needed for preparation of the initial state and analysis of the final state. Third section introduces fundamental scattering quantities that are to be obtained, followed by definitions of a selection of derived quantities, including the spin-flip cross section in the fourth section, the direction-dependent scattering amplitude in the fifth section and fine-structure transition amplitudes in the sixth section. The sixth section also explains which transitions result in non-physical cross sections under approximations done on the way. Finally, the last, seventh, section presents description of the break-up process.

2.1 Physical approximations

To start with, we are interested in energies comparable to the ionization energy. The structure of proton is irrelevant for impact energies in this domain [24] and the whole composit can be regarded as an elementary particle. All elementary particles are deemed point-like sources of electromagnetic field. Heavier isotopes of hydrogen have larger nuclei, but not so dramatically as to violate this assumption [25].

The rest mass of electron is around 511 keV, which is also orders of magnitude larger that the interesting impact energies. Relativistic effects have been thus neglected and non-relativistic Schrödinger equation has been used, with the hamiltonian [26]

$$H = \frac{p_1^2}{2\mu} + \frac{p_2^2}{2\mu} + \frac{\mathbf{p}_1 \cdot \mathbf{p}_2}{m_p} - \frac{\alpha\hbar c}{r_1} - \frac{\alpha\hbar c}{r_2} + \frac{\alpha\hbar c}{r_{12}}\,, \tag{2.1}$$

where $\mu = m_e m_p/(m_e + m_p)$ is the reduced mass of the electron-proton system.

Finally, the proton to electron rest mass ratio is around 1800. Within some degree of accuracy the proton can be thought of as having infinite mass compared to the electron. The presence and motion of electrons then do not alter the kinematic state of the proton

and the hydrogen nucleus can be therefore considered as a static point source (in a convenient frame of reference). This is equivalent to neglecting the *mass polarization* term $(\mathbf{p}_1 \cdot \mathbf{p}_2)/m_p$. The hamiltonian of the system is then

$$H = \frac{p_1^2}{2m_e} + \frac{p_2^2}{2m_e} - \frac{\alpha\hbar c}{r_1} - \frac{\alpha\hbar c}{r_2} + \frac{\alpha\hbar c}{r_{12}}\,. \tag{2.2}$$

In dimensionless atomic units, used in all following equations, is $\hbar = m_e = \alpha c = 1$, leading to

$$H = \frac{p_1^2}{2} + \frac{p_2^2}{2} - \frac{1}{r_1} - \frac{1}{r_2} + \frac{1}{r_{12}}\,. \tag{2.3}$$

2.2 Hydrogen atom

The neutral hydrogen (deuterium, tritium) atom is the scattering target for all considered processes. In the non-relativistical description it is possible to obtain both its bound and continuum eigenstates in a closed form. Both can be also easily generalized to the situation of a charged hydrogen-like ion.

In this work the bound hydrogen wave functions are used in the form

$$\langle \mathbf{r}|\psi_{nlm}\rangle = R_{nl}(r)Y_l^m(\hat{\mathbf{r}})\,, \tag{2.4}$$

where $Y_l^m(\hat{\mathbf{r}})$ is the standard spherical harmonic function and the radial part is

$$R_{nl}(r) = \frac{1}{r}P_{nl}(r) = \sqrt{\left(\frac{2}{n}\right)^3 \frac{(n-l-1)!}{2n(n+l)!}} \left(\frac{2r}{n}\right)^l L_{n-l-1}^{(2l+1)}\left(\frac{2r}{n}\right) \mathrm{e}^{-r/n}\,, \tag{2.5}$$

where $L_n^{(\alpha)}(x)$ is the generalized Laguerre polynomial. The bound states exponentially decrease with distance once the so-called *classical turning point* is reached. This, however, does not prevent a quadratic inflation of the effective radius of the orbital with the increase of the principal quantum number n at fixed angular momentum l ([26], §3.20). Extensive atomic orbitals contribute to the large polarizability of the atom, making the scattering calculations rather difficult.

The free states are used in ionization processes, or in place of plane waves in case that the target is charged. For unit nuclear charge ($Z = 1$) they are described by the functions

$$\langle \mathbf{r}|\psi_{\mathbf{k}}^{(+)}\rangle = \frac{1}{(2\pi)^{3/2}} \sum_{lm} 4\pi \mathrm{i}^l F_l(-1/k, kr) Y_l^m(\hat{\mathbf{r}}) Y_l^{m*}(\hat{\mathbf{k}})\,, \tag{2.6}$$

where the Coulomb (partial) wave function $F_\ell(\eta, \rho)$ is defined as ([27], §33.2)

$$F_\ell(\eta,\rho) = \frac{2^\ell \mathrm{e}^{-\pi\eta/2}|\Gamma(\ell+1+\mathrm{i}\eta)|}{(2\ell+1)!}\rho^{\ell+1}\mathrm{e}^{-\mathrm{i}\rho}{}_1F_1\left(\begin{matrix}\ell+1-\mathrm{i}\eta \\ 2\ell+2\end{matrix}\middle|\, 2\mathrm{i}\rho\right)\,, \tag{2.7}$$

in terms of the confluent hypergeometric function ${}_1F_1$.

2.3 Scattering problem description

Given the hamiltonian (2.3) of the electron-hydrogen system one can search for a subset of its eigenstates coinciding with stationary scattering states. These can be obtained by solution of the time-independent Schrödinger equation

$$\mathsf{H}|\Psi_i^+\rangle = E_{\mathrm{tot}}|\Psi_i^+\rangle \tag{2.8}$$

with a scattering boundary condition, or as a solution of the Lippmann-Schwinger equation

$$|\Psi_i^+\rangle = |\Psi_i\rangle + \mathsf{G}_0^{(+)}\mathsf{H}_{\rm int}|\Psi_i^+\rangle\,, \tag{2.9}$$

where $|\Psi_i\rangle$ is the initial state (atom + incident projectile plane wave), the full hamiltonian H is given by (2.3) and the interaction hamiltonian $\mathsf{H}_{\rm int}$ is the following part of H:

$$\mathsf{H}_{\rm int} = \mathsf{H} - \mathsf{H}_{\rm free} = -\frac{1}{r_{\rm proj}} + \frac{1}{r_{12}}\,, \tag{2.10}$$

The equation (2.8) is often written in the "scattering form"

$$(E - \mathsf{H})\big|\Psi_{\rm sc}^+\big\rangle = \mathsf{H}_{\rm int}|\Psi_i\rangle\,, \tag{2.11}$$

which follows from the definitions $\big|\Psi_i^+\big\rangle = |\Psi_i\rangle + |\Psi_{\rm sc}^+\rangle$ and $(\mathsf{H} - \mathsf{H}_{\rm int})|\Psi_i\rangle = E|\Psi_i\rangle$. This is actually a very prominent equation in the mathematical physics. Written in the coordinate representation it reads

$$\left(\triangle_{6D} + \mathsf{k}^2(\mathbf{r}_1, \mathbf{r}_2)\right)\Psi_{\rm sc}^+(\mathbf{r}_1, \mathbf{r}_2) = \chi_i(\mathbf{r}_1, \mathbf{r}_2)\,, \tag{2.12}$$

which is the (six-dimensional) *Helmholtz equation*, an equation routinely used in the classical propagation, or scattering, of electromagnetic field. Due to the industrial importance of electromagnetism there is an extremely active research activity going on around the Helmholtz equation, part of which has been used to the advantage of this thesis. This includes an effective separation-of-variables preconditioner and a domain decomposition approach, both explained in chapter 4.

The scattering boundary condition mentioned above has different form for discrete scattering (elastic and excitation processes) and for ionization. Ionization boundary condition is described at the end of this chapter, here we focus only on discrete transitions, when just one of the two electrons goes away to infinity. Assuming that the scattered electron is labeled "2", whereas the atomic one "1", the scattering boundary condition has the form

$$\Psi(\mathbf{r}_1, \mathbf{r}_2) \sim \frac{1}{(2\pi)^{3/2}}\psi_i(\mathbf{r}_1)\mathrm{e}^{\mathrm{i}\mathbf{k}_i\cdot\mathbf{r}_2} + \sum_j f_{ji}(\hat{\mathbf{k}}_j)\psi_j(\mathbf{r}_1)\frac{\mathrm{e}^{\mathrm{i}k_j r_2}}{r_2}\,. \tag{2.13}$$

Here ψ is the state of the atomic electron, $\mathbf{k}_i$ is the projectile initial wave vector and $\mathbf{k}_j$ the final wave vector. This must hold when $r_2 \to +\infty$. Analogous boundary condition with indices "1" and "2" swapped holds for $r_1 \to +\infty$. The scattering amplitude f_{ji} characterizes the scattering process. From the quantum scattering theory it can be deduced that it is related to a T-matrix, or element of the T-operator. In this work we use the notation

$$f_{ji} = -\frac{1}{2\pi}\langle\Psi_f|\mathsf{H}_{\rm int}\big|\Psi_i^+\big\rangle = -\frac{1}{2\pi}\langle\Psi_f|\mathsf{T}|\Psi_i\rangle = -\frac{1}{2\pi}T_{ji}\,. \tag{2.14}$$

The cross section is a quantity expressing effectivity of the scattering. The differential cross section is the number of projectiles (N) scattered by a target (originally in state i, leaving in state j) into specific direction per unit of time (t), normalized by the incoming flux density (J). The formal definition of the differential cross section is

$$\frac{\mathrm{d}\sigma_{ji}}{\mathrm{d}\Omega} = \frac{1}{J}\frac{\mathrm{d}N_{ji}}{\mathrm{d}t}\,. \tag{2.15}$$

The integral cross section is (2.15) integrated over all angles,

$$\sigma_{ji} = \int \frac{\mathrm{d}\sigma_{ji}}{\mathrm{d}\Omega}\mathrm{d}\Omega\,. \tag{2.16}$$

The differential cross section can be related to the scattering amplitude as

$$\frac{\mathrm{d}\sigma_{ji}}{\mathrm{d}\Omega} = |f_{ji}|^2\,. \tag{2.17}$$

The T-matrix introduced in (2.14) is indexed by initial and final states, including the magnetic quantum numbers. This quantity can be transformed to a "canonical" T-matrix indexed only by energy and angular momentum of the scattering channels. For the canonical T-matrix it then holds

$$T_{nm} = S_{nm} - \delta_{nm}\,, \tag{2.18}$$

where S-matrix is the unitary *scattering* matrix. This is more thoroughly discussed in chapter 6.

2.4 Separation of spin and spin flip

The wave function of two indistinguishable fermions must be antisymmetrical with respect to exchange of the particles (their full quantum states, i.e. their positions, quantum numbers etc.),

$$|\Psi(1,2)\rangle = -|\Psi(2,1)\rangle\,. \tag{2.19}$$

To enforce the antisymmetry of the solution Ψ_i^+ of (2.11) it is enough to put in an antisymmetrized right hand side $\mathcal{A}\mathsf{H}_{\mathrm{int}}\Psi_i$, because the full hamiltonian itself is symmetrical. The Schrödinger equation (2.8) does not depend on spins of the electrons. Linear combination of solutions with the same spatial part and different spin parts is thus again a solution. Without loss of generality we can cosider two classes of solutions: those with antisymmetric spin part (and symmetric spatial part) and those with symmetric spin part (and antisymmetric spatial part). The former are called the *singlet* states

$$|\Psi_{\mathrm{singlet}}\rangle = \left|\Psi^{0,0}(\mathbf{r}_1,\mathbf{r}_2)\right\rangle\left|\Xi^{0,0}\right\rangle,$$

the latter the *triplet* states

$$|\Psi_{\mathrm{triplet}}\rangle = \left|\Psi^{1,M}(\mathbf{r}_1,\mathbf{r}_2)\right\rangle\left|\Xi^{1,M}\right\rangle,$$

where $M \in \{-1,0,1\}$ is the projection of the total spin. The singlet and triplet spin parts are

$$\begin{aligned}
\left|\Xi^{0,0}\right\rangle &= \frac{1}{\sqrt{2}}\left(\left|\tfrac{1}{2},+\tfrac{1}{2}\right\rangle_1\left|\tfrac{1}{2},-\tfrac{1}{2}\right\rangle_2 - \left|\tfrac{1}{2},-\tfrac{1}{2}\right\rangle_1\left|\tfrac{1}{2},+\tfrac{1}{2}\right\rangle_2\right),\\
\left|\Xi^{1,-1}\right\rangle &= \left|\tfrac{1}{2},-\tfrac{1}{2}\right\rangle_1\left|\tfrac{1}{2},-\tfrac{1}{2}\right\rangle_2,\\
\left|\Xi^{1,0}\right\rangle &= \frac{1}{\sqrt{2}}\left(\left|\tfrac{1}{2},+\tfrac{1}{2}\right\rangle_1\left|\tfrac{1}{2},-\tfrac{1}{2}\right\rangle_2 + \left|\tfrac{1}{2},-\tfrac{1}{2}\right\rangle_1\left|\tfrac{1}{2},+\tfrac{1}{2}\right\rangle_2\right),\\
\left|\Xi^{1,+1}\right\rangle &= \left|\tfrac{1}{2},+\tfrac{1}{2}\right\rangle_1\left|\tfrac{1}{2},+\tfrac{1}{2}\right\rangle_2.
\end{aligned}$$

The states classified by the total spin satisfy the relation (2.19) and are useful for the calculation. The initial and final state, however, are generally not eigenstates of total

spin angular momentum, they only have a fixed spin of the atomic electron (s) and projectile electron (s'). Antisymmetrizazion of such a state results in

$$|\Psi_i, s_i, s_i'\rangle = \frac{1}{\sqrt{2}}\left(|\psi_i\rangle_1|\beta_i\rangle_2\big|\tfrac{1}{2}, s_i\big\rangle_1\big|\tfrac{1}{2}, s_i'\big\rangle_2 - |\beta_i\rangle_1|\psi_i\rangle_2\big|\tfrac{1}{2}, s_i'\big\rangle_1\big|\tfrac{1}{2}, s_i\big\rangle_2\right),$$

where ψ is an atomic orbital and β an incident plane wave state. This wave function can be expressed in terms of the singlet and triplet spatial parts

$$|\Psi_{i,\text{singlet}}\rangle = \frac{1}{\sqrt{2}}\left(|\psi_i\rangle_1|\beta_i\rangle_2 + |\beta_i\rangle_1|\psi_i\rangle_2\right) \quad \text{and} \quad |\Psi_{i,\text{triplet}}\rangle = \frac{1}{\sqrt{2}}\left(|\psi_i\rangle_1|\beta_i\rangle_2 - |\beta_i\rangle_1|\psi_i\rangle_2\right)$$

using one of the rows in the table 2.1.

s	s'	$\lvert\Psi_i\rangle$
$-\frac{1}{2}$	$-\frac{1}{2}$	$\lvert\Psi_{i,\text{triplet}}\rangle\lvert\Xi^{1,-1}\rangle$
$-\frac{1}{2}$	$+\frac{1}{2}$	$\frac{1}{\sqrt{2}}(\lvert\Psi_{i,\text{triplet}}\rangle\lvert\Xi^{1,0}\rangle - \lvert\Psi_{i,\text{singlet}}\rangle\lvert\Xi^{0,0}\rangle)$
$+\frac{1}{2}$	$-\frac{1}{2}$	$\frac{1}{\sqrt{2}}(\lvert\Psi_{i,\text{triplet}}\rangle\lvert\Xi^{1,0}\rangle + \lvert\Psi_{i,\text{singlet}}\rangle\lvert\Xi^{0,0}\rangle)$
$+\frac{1}{2}$	$+\frac{1}{2}$	$\lvert\Psi_{i,\text{triplet}}\rangle\lvert\Xi^{1,+1}\rangle$

Table 2.1: Antisymmetrized initial state expressed in terms of the singlet/triplet spatial combinations and total spin eigenstates.

If we now introduce the spin transition T-matrix element

$$T_{ji,s_j s_j' s_i s_i'} = \big\langle \Psi_j, s_j, s_j'\big|\mathsf{T}\big|\Psi_i, s_i, s_i'\big\rangle$$

and total spin T-matrices

$$T_{ji}^0 = \big\langle \Psi_{j,\text{singlet}}, \Xi^{0,0}\big|\mathsf{T}\big|\Psi_{i,\text{singlet}}, \Xi^{0,0}\big\rangle \quad \text{and} \quad T_{ji}^1 = \big\langle \Psi_{j,\text{triplet}}, \Xi^{1,M}\big|\mathsf{T}\big|\Psi_{i,\text{triplet}}, \Xi^{1,M}\big\rangle,$$

of which $T_{ji,s_j s_j' s_i s_i'}$ is the interesting physical quantity, whereas T_{ji}^S are more straightforward to calculate, we can write the following relations between these expressions:

$$T_{ji,\pm\frac{1}{2},\pm\frac{1}{2},\pm\frac{1}{2},\pm\frac{1}{2}} = T_{ji}^1 \qquad \text{[maximal projection]} \tag{2.20}$$

$$T_{ji,\pm\frac{1}{2},\mp\frac{1}{2},\pm\frac{1}{2},\mp\frac{1}{2}} = \frac{1}{2}(T_{ji}^1 + T_{ji}^0) \qquad \text{[spin-elastic]} \tag{2.21}$$

$$T_{ji,\pm\frac{1}{2},\mp\frac{1}{2},\mp\frac{1}{2},\pm\frac{1}{2}} = \frac{1}{2}(T_{ji}^1 - T_{ji}^0) \qquad \text{[spin-flip]} \tag{2.22}$$

From the above T-matrices, which are proportional to the scattering amplitudes (2.14), we can obtain the spin-flip cross section

$$\frac{\mathrm{d}\sigma_{ji}^{\text{spin-flip}}}{\mathrm{d}\Omega} = \frac{1}{4}|f_{ji}^1 - f_{ji}^0|^2\,. \tag{2.23}$$

It is also possible to obtain spin-averaged cross section for unpolarized initial states. Averaging over initial spin configurations and summing over final spin configuration we obtain

$$\frac{\mathrm{d}\sigma_{ji}}{\mathrm{d}\Omega} = \frac{1}{4}\sum_{s_j, s_j'=\pm\frac{1}{2}}\sum_{s_i, s_i'=\pm\frac{1}{2}}|f_{ji,s_j,s_j',s_i,s_i'}|^2 = \frac{1}{4}|f_{ji}^0|^2 + \frac{3}{4}|f_{ji}^1|^2\,. \tag{2.24}$$

Often we talk about singlet or triplet cross section, which is one of the resulting terms in (2.24) multiplied by the spin weight,

$$\frac{\mathrm{d}\sigma_{ji}^{S}}{\mathrm{d}\Omega} = \frac{2S+1}{4}|f_{ji}^{S}|^2\,, \tag{2.25}$$

or the angle-integrated value of this expression.

2.5 Arbitrary impact angle scattering

In the following sections we will use a specific quantization axis (chosen as the third, z, axis). All projections are considered with respect to this axis. For example the hydrogen magnetic quantum number is a projection of the angular momentum into this axis. Also, the projectile is always described as a plane wave coming in the direction of the quantization axis, so that the projection of its orbital momentum onto the quantization axis can be set to zero.

In general applications, however, the impacting electron can approach a polarized atom from any spatial direction. Fortunately, the scattering amplitudes for those configurations can be obtained as a linear combination of amplitudes of scattering in the idealized single-axis case. The key idea is that a given angular momentum state

$$|\psi\rangle = |l, m\rangle$$

in one coordinate frame will transform to a combination of states

$$|\psi'\rangle = \sum_{m'} D^{l}_{m,m'}(\alpha,\beta,\gamma)|l, m'\rangle$$

after rotation given by the Euler angles α, β and γ. The symbol $D^{l}_{m,m'}(\alpha,\beta,\gamma)$ is the Wigner matrix and apart from phase factors it is equal to the "small d" Wigner matrix $d^{l}_{m,m'}(\beta)$. Here β is the angle between the original quantization axis and the new quantization axis.

Using these observations, scattering amplitude for the reaction

$$\mathrm{H}(n_i, l_i, m_i) + e^- \to \mathrm{H}(n_j, l_j, m_j) + e^-\,,$$

where the impact direction and the atom's quantization axis make angle β, can be written in terms of z-aligned scattering amplitude as

$$f_{n_j,l_j,m_j\leftarrow n_i,l_i,m_i}(\beta) = \sum_{m_i'} f_{n_j,l_j,m_j\leftarrow n_i,l_i,m_i'}(0)\, d^{l_i}_{m_i',m_i}(\beta)\,. \tag{2.26}$$

2.6 Accidental degeneracy and fine structure transitions

In spectroscopy, the notation $|\psi\rangle = |nlj\mu\rangle$ rather than $|\psi\rangle = |nlms\rangle$ is used. For heavier atoms, where the relativistic effects play larger role than in the case of hydrogen, the spin-orbital coupled quantum numbers l, j and μ are better than simple l, m and s. However, as we have neglected all relativistic effects, description using lms and $lj\mu$ are equivalent and related by a unitary transformation given by Clebsch-Gordan coefficients.

Using the relation

$$\langle l_j j_j \mu_j | \mathsf{T} | l_i j_i \mu_i \rangle = \sum_{m_j m_i s_j s_i} C^{j_j \mu_j}_{l_j m_j, \frac{1}{2} s_j} C^{j_i \mu_i}_{l_i m_i, \frac{1}{2} s_i} \langle l_j m_j s_j | \mathsf{T} | l_i m_i s_i \rangle$$

it follows

$$f_{n_j, l_j, j_j, \mu_j \leftarrow n_i, l_i, j_i, \mu_i} = \sum_{m_j m_i s_j s_i} C^{j_j \mu_j}_{l_j m_j, \frac{1}{2} s_j} C^{j_i \mu_i}_{l_i m_i, \frac{1}{2} s_i} f_{n_j, l_j, m_j, s_j \leftarrow n_i, l_i, m_i, s_i} \,. \tag{2.27}$$

In the non-relativistic approximation used in this work the states $2s_j$ and $2p_{j'}$ have exactly equal energy irrespective of the values of j and j'. This phenomenon is called the *accidental degeneracy* and corresponds to the existence of another quantum number related to the Runge-Lenz vector, that commutes with energy in case of the pure Coulomb potential.[1] The energy degeneracy of the levels with the same principal quantum number has an unpleasant consequence that the cross sections for processes $\mathrm{H}(n, l) \to \mathrm{H}(n, l \pm 1)$ are infinite. Here follows a short explanation inspired by [29] and [30].

It will be shown later that the Schrödinger equation for the unknown two-electron scattering function $\Psi(\mathbf{r}_1, \mathbf{r}_2) = (r_1 r_2)^{-1} \sum_{\ell_1 \ell_2 L M} \psi^{LM}_{\ell_1 \ell_2}(r_1, r_2) \mathcal{Y}^{LM}_{\ell_1 \ell_2}(\hat{\mathbf{r}}_1, \hat{\mathbf{r}}_2)$ can be written as

$$\sum_{\ell_1' \ell_2'} \left[(E_{\mathrm{tot}} - T_{\ell_1} - T_{\ell_2}) \, \delta^{\ell_1'}_{\ell_1} \delta^{\ell_2'}_{\ell_2} - \sum_{\lambda} V^{\lambda}_{\ell_1 \ell_2 \ell_1' \ell_2'; L} \right] \psi^{LM}_{\ell_1' \ell_2'} = \chi^{LM}_{\ell_1 \ell_2} \,,$$

where T_ℓ are the operators of kinetic energy and the multipole potential is

$$V^{\lambda}_{\ell_1 \ell_2 \ell_1' \ell_2'; L} = f^{\lambda}_{\ell_1 \ell_2 \ell_1' \ell_2'; L} \left(-\frac{\delta^0_\lambda}{r_1} - \frac{\delta^0_\lambda}{r_2} + \frac{r^\lambda_<}{r^{\lambda+1}_>} \right) .$$

Now consider such a two-electron wave function at energies below the $n = 3$ threshold. The atomic electron can be either in s-state, or p-state, other orbital momenta are not allowed. We will also restrict ourselves to states with $n = 2$. The radial components then must asymptotically tend to (for large projectile coordinates $r_2 = r$)

$$\begin{aligned} \psi_{0,\ell}(R, r) &\to P_{2s}(R) F^s_\ell(r) \,, \\ \psi_{1,\ell-1}(R, r) &\to P_{2p}(R) F^p_{\ell-1}(r) \,. \end{aligned}$$

When we substitute these asymptotic conditions to the equation above and project them on the two considered hydrogen states, we get

$$\begin{aligned} \left(k^2 + \frac{\mathrm{d}^2}{\mathrm{d}r^2} - \frac{\ell(\ell+1)}{r^2} \right) F^s_\ell(r) &= 2 \langle 2s | V^0_{0,\ell,0,\ell;\ell} | 2s \rangle F^s_\ell(r) + 2 \langle 2s | V^1_{0,\ell,1,\ell-1;\ell} | 2p \rangle F^p_{\ell-1}(r) \,, \\ \left(k^2 + \frac{\mathrm{d}^2}{\mathrm{d}r^2} - \frac{\ell(\ell-1)}{r^2} \right) F^p_{\ell-1}(r) &= 2 \langle 2p | V^0_{1,\ell-1,1,\ell-1;\ell} | 2p \rangle F^p_{\ell-1}(r) + 2 \langle 2p | V^1_{1,\ell-1,0,\ell;\ell} | 2s \rangle F^s_\ell(r) \,, \end{aligned}$$

where $k^2 = 2(E_{\mathrm{tot}} - E_{2s}) = 2(E_{\mathrm{tot}} - E_{2p})$ and the specific indices on $V^{\lambda}_{\ell_1 \ell_2 \ell_1' \ell_2'; L}$ follow from the properties of the angular integral $f^{\lambda}_{\ell_1 \ell_2 \ell_1' \ell_2'; L}$. The multipole potential $V^{\lambda}_{\ell_1 \ell_2 \ell_1' \ell_2'; L}$ is

[1] This additional symmetry is broken by spin-orbit and radiative corrections, which are of relative order α^2 in energy, see [28].

short-range for $\lambda = 0$, but it evaluates to a long-range dipole potential when $\lambda = 1$. After keeping only the long-range parts and relabeling the angular momentum of $F^p_\ell(r)$ it is

$$\left(k^2 + \frac{\mathrm{d}^2}{\mathrm{d}r^2} - \frac{\ell(\ell+1)}{r^2}\right) F^s_\ell(r) = \frac{A}{r^2} F^p_\ell(r)\,,$$
$$\left(k^2 + \frac{\mathrm{d}^2}{\mathrm{d}r^2} - \frac{\ell(\ell+1)}{r^2}\right) F^p_\ell(r) = \frac{A}{r^2} F^s_\ell(r)\,.$$

These equations have been solved by Seaton in [29] by combining them into an equation for $F_{\ell+} = F^s_\ell + F^p_\ell$ and an equation for $F_{\ell-} = F^s_\ell - F^p_\ell$; they result in the scattering T-matrix

$$T_{2s-2p,\ell} = T_{2p-2s,\ell} \sim \frac{A}{2\ell+1} \qquad [\ell \to \infty]\,.$$

The corresponding partial cross section

$$\sigma_{2s-2p,\ell} = \sigma_{2p-2s,\ell} \sim (2\ell+1)|T_{2p-2s,\ell}|^2 \sim \frac{A^2}{2\ell+1} \qquad [\ell \to \infty]$$

behaves as ℓ^{-1} for large partial waves and as such it does not sum to a final total cross section. The situation changes when the states $2p$ and $2s$ have even a tiny energy shift $\Delta\varepsilon$. As shown by Gailitis and Damburg in [30], the total cross section is then proportional to

$$\sigma_{2s-2p} \sim -\ln \Delta\varepsilon\,.$$

2.7 Ionization

The fragmentation process needs a different description. It is not compatible with the discrete transition boundary condition (2.13), where only one of the electrons is allowed to escape to infinite distance. Instead one has to use the ionization boundary condition, which was summarized e.g. in [31]. There are several possible output configurations:

- Uniform ionization (Ω_0): Both electrons escape into infinity and become also well separated from each other. The conditions for Ω_0 are $\rho^2 = r_1^2 + r_2^2 \to +\infty$ and neither r_1/ρ, nor r_2/ρ approaches zero. Or, equivalently, r_1/r_2 converges neither to zero, nor to infinity.

- First electron isolation (Ω_1): In this configuration the first electron has been accelerated significantly more than the other one. The electrons escape ($\rho \to +\infty$), but the second tarries behind ($r_2/r_1 \to 0$).

- Second electron isolation (Ω_2): As above, but with swapped roles. Now the second electron is the faster one and $r_1/r_2 \to 0$.

- Nuclear isolation (Ω_3): Finally, it can happen that the electrons are ejected into a similar direction, making their correlation very important. This happens when $\rho \to +\infty$, but $|\mathbf{r}_1 - \mathbf{r}_2|/\rho \to 0$.

Every Ω_i must be handled separately, which has been done in [31] in Jacobi coordinates, i.e. in terms of the three-particle relative positions and canonically conjugated momenta.

For the case of uniform ionization (Ω_0) the asymptotic form of the wave function is (see also [32])

$$\Psi^+_{sc}(\mathbf{r}_\alpha, \boldsymbol{\rho}_\alpha) \sim \frac{(2\pi\mathrm{i})^{1/2}}{(2\pi)^3} f\left(\frac{\mu_\alpha}{m}\frac{\kappa}{\rho}\mathbf{r}_\alpha, \frac{M_\alpha}{m}\frac{\kappa}{\rho}\boldsymbol{\rho}_\alpha\right) \frac{(\mu_\alpha M_\alpha)^{3/2}}{m^2}\frac{\kappa^{3/2}}{\rho^{5/2}} \mathrm{e}^{\mathrm{i}\kappa\rho - \mathrm{i}\lambda_0 \ln(2\kappa\rho) - \mathrm{i}\sigma_0}\,. \qquad (2.28)$$

In this formula: $\mathbf{r}_\alpha$ is relative position of particles β and γ; $\boldsymbol{\rho}_\alpha$ is the position of particle α with respect to the centre of mass of particles β and γ; μ_α is the reduced mass of the particles β and γ; M_α is the reduced math of particle α and the $\beta\gamma$ pair; z_α is the electric charge of particle α in terms of the elementary charge; m is an optional positive constant with dimension of mass. Function f is the ionization amplitude in Jacobi coordinates. The remianing variables are defined here:

$$\eta_\alpha = z_\beta z_\gamma \mu_\alpha\,, \qquad \kappa = (2mE_{\mathrm{tot}})^{1/2}\,, \qquad \rho = \left(\frac{\mu_\alpha}{m}r_\alpha^2 + \frac{M_\alpha}{m}\rho_\alpha^2\right)^{1/2}\,,$$

$$\lambda_0 = \frac{1}{\kappa}\sum_{\nu=\alpha,\beta,\gamma}\left(\frac{m}{\mu_\nu}\right)^{1/2}\frac{\eta_\nu}{\sin\varphi_\nu}\,, \qquad \sigma_0 = \frac{2}{\kappa}\sum_{\nu=\alpha,\beta,\gamma}\left(\frac{m}{\mu_\nu}\right)^{1/2}\frac{\eta_\nu \ln\sin\varphi_\nu}{\sin\varphi_\nu}\,,$$

$$\varphi_\alpha = \arctan\left[\left(\frac{\mu_\alpha}{M_\alpha}\right)^{1/2}\frac{r_\alpha}{\rho_\alpha}\right].$$

When one of the particles is "infinitely heavy" compared to the other two, the formula greatly simplifies. If $\alpha = 2$ is one of the electrons, then $\mathbf{r}_\alpha$ reduces to $\mathbf{r}_1$ and $\boldsymbol{\rho}_\alpha$ to $\mathbf{r}_2$. Picking $m = m_e = 1$ we obtain

$$\Psi^+_{sc}(\mathbf{r}_1, \mathbf{r}_2) \sim \frac{1}{(2\pi)^{5/2}} f\left(\kappa\frac{\mathbf{r}_1}{\rho}, \kappa\frac{\mathbf{r}_2}{\rho}\right)\frac{\kappa^{3/2}}{\rho^{5/2}}\mathrm{e}^{\mathrm{i}\kappa\rho - \mathrm{i}\lambda_0\ln(2\kappa\rho) - \mathrm{i}\sigma_0 + \mathrm{i}\pi/4}\,. \qquad (2.29)$$

The function f is the ionization amplitude. In the limit of $r_1 \to +\infty$ and $r_2 \to +\infty$ it is equal to $f(\mathbf{k}_1, \mathbf{k}_2)$, with no dependence on the coordinates. The conservation of energy

$$\frac{1}{2}\left(k_1^2 + k_2^2\right) = \frac{1}{2}\left[\left(\kappa\frac{r_1}{\rho}\right)^2 + \left(\kappa\frac{r_2}{\rho}\right)^2\right] = \frac{1}{2}\kappa^2\frac{r_1^2 + r_2^2}{\rho^2} = E_{\mathrm{tot}}$$

results as a byproduct.

Chapter 3

Design of the Hex package

3.1 Hex modules

The original conception was to create a single computer program that would be able to calculate the T-matrix or cross section for arbitrary energy and transition. Such program would be valuable and user-friendly for the applied researchers in astrophysics and plasma physics. Very soon it became apparent that this idea would lead to a program too complex and computationally too demanding for any serious application. Another way has been chosen, which is summarized in this chapter.

The principal change has been the separation of the production of the data into two phases:

- Solution of the scattering equations and production of the scattering T-matrices as an intermediate result.
- Calculation of derived scattering quantities from the T-matrices, particularly various cross sections.

In the first phase the T-matrices are calculated by an expert in quantum scattering theory and stored in an intermediate database, which is then accessed by the database *interface program* in the second phase by other researchers needing the data. The calculation of the T-matrices in the first phase is managed by several *computational modules*, which are computer programs that implement various solution methods. Every method is valid (or computationally feasible) only over a specific energy interval. Determination of overlaps of the implemented methods was a necessary part of the first phase.

The schematic layout of the package is presented in a form of a graph in the figure 3.1. There are several computational modules of varying degree of completeness. Here is a short overwiew.

- The scattering at low and intermediate energies is found by a direct solution of the Schrödinger equation in the basis of B-spline functions, with the *exterior complex scaling* approach used to avoid explicit usage of the scattering boundary condition (program hex-ecs). The use of B-splines in the Schrödinger equation (2.11) converts the differential equation into a large matrix equation. This low-energy part received most attention in this work and the rest of the text is dedicated almost exclusively to its explanation and to the results calculated by this method.
- The scattering quantities for high energies are obtained by the perturbation method of the Born approximation of the second or first order (programs hex-pwba2 and

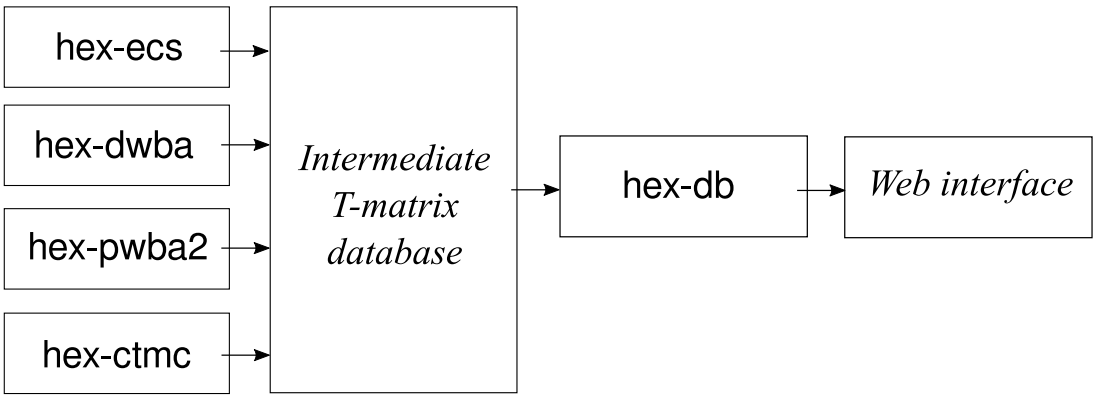

Figure 3.1: Hex package scheme. The programs are written in an upright font. Other infrastracture is in italics.

hex-dwba). These programs were not yet optimized for serious runs, neither used for production calculations. Their description has already been done in the master thesis [**33**] and was thus omitted from this text. The same also holds for the planned program hex-ctmc, intended for high energies and high partial waves, implementation of which did not yet start.

The interface program hex-db is command-line based, which allows its easy inclusion in various scripts. Even more, the main part of the program is separated into a shared library. The library can be linked to derived programs and offer full functionality of the database interface. There is also a web front-end to the database interface at the web pages of the Institute of Theoretical Physics, archiving all final results of calculations done during this work:

`http://utf.mff.cuni.cz/data/hex`

At the same page one can also obtain the latest frozen releases of the programs. The most up-to-date sources and binaries can be found at the SourceForge repository:

`https://sourceforge.net/projects/hecs`

3.2 Database structure

For the database the SQLite [34] format has been chosen. It is a well-established database format used in a vast amount of computer software. SQLite is dedicated to the public domain, free of patents and copyright issues and with prospect of being maintained for decades. The format is binary and the data are manipulated using calls to the SQLite library. The calls have a form of the text SQL statements. "SQL" is an abbreviation of the *Structured Query Language*, which is a standardized form of accessing a database.

The database consists of three tables—ordered sets of key-value pairs—which contain the data and its indices. The database tables are listed in table 3.1. The tables are created using the following statements:

```
CREATE TABLE IF NOT EXISTS 'tmat'
(
    ni INTEGER, li INTEGER, mi INTEGER,
    nf INTEGER, lf INTEGER, mf INTEGER,
```

```
    L  INTEGER, S  INTEGER,
    Ei DOUBLE PRECISION,
    ell INTEGER,
    Re_T_ell DOUBLE PRECISION,
    Im_T_ell DOUBLE PRECISION
    PRIMARY KEY (ni,li,mi,nf,lf,mf,L,S,Ei,ell)
);

CREATE TABLE IF NOT EXISTS 'ics'
(
    ni INTEGER, li INTEGER, mi INTEGER,
    nf INTEGER, lf INTEGER, mf INTEGER,
    S  INTEGER,
    Ei DOUBLE PRECISION,
    ell INTEGER,
    sigma DOUBLE PRECISION
    PRIMARY KEY (ni,li,mi,nf,lf,mf,S,Ei,ell)
);

CREATE TABLE IF NOT EXISTS 'ionf'
(
    ni INTEGER, li INTEGER, mi INTEGER,
    L  INTEGER, S  INTEGER,
    Ei DOUBLE PRECISION,
    l1 INTEGER, l2 INTEGER,
    cheb BLOB,
    PRIMARY KEY (ni,li,mi,L,S,Ei,l1,l2)
);
```

The meaning of the individual variables will be clear from further chapters. Only the last table contains non-trivially stored radial part $f^{LS}_{\ell_1,\ell_2}(k_1,k_2)$ of the ionization amplitude, see (4.17), which should be clarified here. The function $f^{LS}_{\ell_1,\ell_2}(k_1,k_2)$, even though it appears to have two arguments, is essentially one-dimensional, because the two linear momenta k_1 and k_2 are bound by the conservation of energy

$$k_1^2 + k_2^2 = k_i^2 - \frac{1}{n_i^2}\,.$$

The linear momenta can be parametrized by the hyperangle α, or by its cosine $x = \cos\alpha$, as $k_1 = k_{\max}x$, $k_2 = k_{\max}\sqrt{1-x^2}$, where $k_{\max} = \sqrt{2E_{\rm tot}}$. The one-dimensional function $f^{LS}_{\ell_1,\ell_2}(k_1(x),k_2(x))$ is approximated using the Chebyshev polynomials, see the Appendix A. The array of the Chebyshev expansion coefficients is then stored in a raw binary form as the element `cheb` in the table `ionf`. No endianness management is done, so if one transfers the database between big- and little-endian operating systems, it will not be compatible. Most commonly used operating systems (Linux, Windows) are little-endian, though.

3.3 VAMDC connection

VAMDC (*Virtual Atomic and Molecular Centre*, [35]) is a European project that centralizes various atomic and molecular databases offered by different scientific groups and

Title	Contents	Indexed by
tmat	T-matrices (real and imaginary part)	$n_i, l_i, m_i, n_f, l_f, m_f, L, S, \ell, E_i$
ionf	ionization amplitude (see (4.17))	$n_i, l_i, m_i, L, S, \ell_1, \ell_2, E_i$
ics	partial cross section	$n_i, l_i, m_i, n_f, l_f, m_f, L, S, E_i$

Table 3.1: Hex database structure. The symbols indicate the initial atomic state (n_i, l_i, m_i), final atomic state (n_f, l_f, m_f), total electron angular momentum L, total electron spin S, incoming electron angular momentum ℓ, incoming electron energy E_i and outgoing electron angular momenta ℓ_1 and ℓ_2.

institutes. It allows users of the VAMDC web portal to query all included databases simultaneously for required data.

The communication between VAMDC and individual databases takes form of *VAMDC SQL subset version 2* queries (*VSS2*) and XML responses. A typical query can look like this:

```
SELECT
    AtomStates, Processes, Sources, Methods
WHERE
    reactant1.StateEnergy = -1 AND
    product1.StateEnergy <= -0.25
```

This request is sent by accessing the database server at address:

```
http://[server]/sync?REQUEST=doQuery&LANG=VSS2&FORMAT=XSAMS&QUERY=[query]
```

where "[server]" is the database server address (e.g. utf.mff.cuni.cz/data/hex) and "[query]" is the above VSS2 statement.

The response of the database server is a XML document, which (in the case of Hex) contains a list of hydrogen initial and final states, the restricted list of processes they participate in, and references to sources and methods explaining the origin of the data. Also, for each process it contains available datasets, in this particular case the energy-dependent integral cross sections. A truncated example is in the following listing; ellipsed parts have been replaced by "(...)".

```
<?xml version="1.0" encoding="UTF-8"?>
<XSAMSData xmlns="http://vamdc.org/xml/xsams/1.0"
        xmlns:xsi="http://www.w3.org/2001/XMLSchema-instance"
        xsi:schemaLocation="http://vamdc.org/xml/xsams/1.0 http://vamdc.org/xml/xsams/1.0">
    <Species>
        <Atoms>
            <Atom>
                <ChemicalElement>
                    <NuclearCharge>1</NuclearCharge>
                    <ElementSymbol>H</ElementSymbol>
                </ChemicalElement>
                <Isotope>
                    <Ion speciesID = "X.H">
                        <IonCharge>0</IonCharge>
                        <AtomicState stateID = "S.1s0">
                            <Description>1s (m = 0)</Description>
                            <AtomicNumericalData>
                                <StateEnergy><Value units = "Ry">-1</Value></StateEnergy>
                            </AtomicNumericalData>
                            <AtomicQuantumNumbers>
                                <TotalAngularMomentum>0</TotalAngularMomentum>
                                <MagneticQuantumNumber>0</MagneticQuantumNumber>
```

```
                        </AtomicQuantumNumbers>
                    </AtomicState>
                    (...)
                    <InChIKey>YZCKVEUIGOORGS-UHFFFAOYSA-N</InChIKey>
                </Ion>
            </Isotope>
        </Atom>
    </Atoms>
    <Particles>
        <Particle speciesID = "X.e" name = "electron"/>
    </Particles>
</Species>
<Processes>
    <Collisions>
        <CollisionalTransition id = "P.1s0.1s0">
            <ProcessClass>
                <Code>elas</Code>
                <IAEACode>EDX</IAEACode>
            </ProcessClass>
            <Reactant><SpeciesRef>X.H</SpeciesRef><StateRef>S.1s0</StateRef></Reactant>
            <Reactant><SpeciesRef>X.e</SpeciesRef></Reactant>
            <Product><SpeciesRef>X.H</SpeciesRef><StateRef>S.1s0</StateRef></Product>
            <Product><SpeciesRef>X.e</SpeciesRef></Product>
            <Threshold><Value units = "Ry">0</Value></Threshold>
            <DataSets>
                <DataSet dataDescription = "crossSection">
                    <TabulatedData>
                        <Description>
                            Cross section for reaction e + H[1s0] -> e + H[1s0]
                        </Description>
                        <X units = "Ry"><DataList count = "230"> (...) </DataList></X>
                        <Y units = "au"><DataList> (...) </DataList></Y>
                        <ReferenceFrame>TargetFrame</ReferenceFrame>
                    </TabulatedData>
                </DataSet>
            </DataSets>
        </CollisionalTransition>
        (...)
    </Collisions>
</Processes>
<Sources>
    <Source sourceID="B.HexII">
        <Category>journal</Category>
        <SourceName>Comput. Phys. Commun</SourceName>
        <Year>2014</Year>
        <Authors>
            <Author><Name>Benda J.</Name></Author>
            <Author><Name>Houfek K.</Name></Author>
        </Authors>
    </Source>
</Sources>
<Methods>
    <Method methodID="M.calc">
        <Category>theory</Category>
        <Description>Exterior complex scaling</Description>
    </Method>
</Methods>
</XSAMSData>
```

Chapter 4

Hex-ecs: The low-energy program

4.1 Theory

The program hex-ecs implements direct numerical solution of the Schrödinger equation in the basis of B-spline functions on a radial grid transformed by *exterior complex scaling* (ECS). The details are discussed in this chapter.

This method was published in articles **[36]** and **[37]**, which build on the seminal work of McCurdy and Martín [38] (see also [39]), advancing their method with several improvements. The current implementation is an alternative to the successful PECS (*propagating ECS*) approach of Bartlett [15]. While PECS uses a fixed-order discretization rule, hex-ecs—through the use of B-splines—allows a choice of arbitrary discretization order and makes the grid setup more straightforward. The domain decomposition preconditioner presented at the end of the chapter acts as a counterpart to the propagation technique introduced in PECS.

This first section deals with the theoretical aspects of the method, from the basic equation to its linear-algebraic formulation. The next section discusses the numerical solution and properties. The last section, finally, deals with the pressing problem of the radial convergence of scattering quantities.

4.1.1 Angular momentum expansion

The scattering solution $|\Psi_{sc}\rangle$ of the Schrödinger equation (2.11) is expanded in bi-polar spherical functions,

$$\Psi_{sc}(\mathbf{r}_1, \mathbf{r}_2) = \langle \mathbf{r}_1 \mathbf{r}_2 | \, \Psi_{sc} \rangle = \frac{1}{r_1 r_2} \sum_{LM\ell_1\ell_2} \psi^{LM}_{sc,\ell_1\ell_2}(r_1, r_2) \mathcal{Y}^{LM}_{\ell_1\ell_2}(\hat{\mathbf{r}}_1, \hat{\mathbf{r}}_2) \,, \tag{4.1}$$

where

$$\mathcal{Y}^{LM}_{\ell_1\ell_2}(\hat{\mathbf{r}}_1, \hat{\mathbf{r}}_2) = \sum_{m_1 m_2} C^{LM}_{\ell_1 m_1 \ell_2 m_2} Y^{m_1}_{\ell_1}(\hat{\mathbf{r}}_1) Y^{m_2}_{\ell_2}(\hat{\mathbf{r}}_2) \,. \tag{4.2}$$

By projecting the equation (2.11) on a complete set of the bi-polar spherical harmonics (4.2) one transforms the original single six-dimensional differential equation to an infinite set of two-dimensional differential equations numbered by the angular momenta ℓ_1, ℓ_2 and L,

$$\sum_{\ell_1'\ell_2'} \left[(E - \mathsf{H}_1 - \mathsf{H}_2) \delta^{\ell_1'}_{\ell_1} \delta^{\ell_2'}_{\ell_2} - \langle (\ell_1\ell_2) LM | \frac{1}{r_{12}} | (\ell_1'\ell_2') LM \rangle \right] \psi^{LM}_{sc,\ell_1'\ell_2'}(r_1, r_2) = \chi^{LM}_{\ell_1,\ell_2}(r_1, r_2) \,. \tag{4.3}$$

The quantum number M does not raise the number of equations, because in the configuration used the projectile approaches along the z-axis and thus has no component of angular momentum in that axis. The total angular momentum projection M is then always equal to the initial magnetic quantum number of the target.

The system of equations is not coupled in total angular momentum, which is a consequence of conservation of this quantum number. We can thus correct the previous observation and state that there is an infinite number ($L = 0, 1, \ldots$) of infinite coupled systems of differential equations numbered by ℓ_1 and ℓ_2.

The coupling of the equations is due to the two-electron term

$$\langle(\ell_1\ell_2)LM|\frac{1}{r_{12}}|(\ell_1'\ell_2')LM\rangle = \langle\ell_1\ell_2\|\frac{1}{r_{12}}\|\ell_1'\ell_2'\rangle_L = \sum_\lambda f^\lambda_{\ell_1\ell_2\ell_1'\ell_2';L}\frac{r_<^\lambda}{r_>^{\lambda+1}}\,, \tag{4.4}$$

$$f^\lambda_{\ell_1\ell_2\ell_1'\ell_2';L} = (-1)^{L+\ell_2+\ell_2'}\begin{Bmatrix}\ell_1 & \ell_2 & L\\ \ell_2' & \ell_1' & \lambda\end{Bmatrix}\begin{pmatrix}\ell_1 & \lambda & \ell_1'\\ 0 & 0 & 0\end{pmatrix}\begin{pmatrix}\ell_2 & \lambda & \ell_2'\\ 0 & 0 & 0\end{pmatrix}\times$$
$$\times\sqrt{(2\ell_1+1)(2\ell_2+1)(2\ell_1'+1)(2\ell_2'+1)}\,.$$

The braces and parentheses denote the standard Wigner 6j and 3j symbols, respectively.

When we organize the set of the equations into a matrix equation, where the rows and columns are indexed by ℓ_1 and ℓ_2, the only off-diagonal elements are those where some $f^\lambda_{\ell_1\ell_2\ell_1'\ell_2';L} \neq 0$. The angular function f^λ then determines the structure of the $(E\mathsf{1} - \mathsf{H})$ matrix. It has the following properties:

- The function $f^\lambda_{\ell_1\ell_2\ell_1'\ell_2';L}$ is zero whenever the triplet $\{\ell_1, \ell_2, L\}$ or $\{\ell_1', \ell_2', L\}$ violates triangle inequality that requires $|\ell_1 - \ell_2| \leq L$ and $\ell_1 + \ell_2 \geq L$.

- It is also identical zero whenever the operator r_{12}^{-1} would couple angular states of different parity. This means that $f^\lambda_{\ell_1\ell_2\ell_1'\ell_2';L}$ is non-zero only if $(-1)^{\ell_1+\ell_2} = (-1)^{\ell_1'+\ell_2'}$.

Putting these rules together, we can draw a graphical representation of the matrix $(E\mathsf{1} - \mathsf{H})$. An example for $L = 2$ and $\ell_{1,2} \leq 5$ is given in the figure 4.1. The original matrix has 36 diagonal components. The lack of even-odd parity coupling is clearly visible. The system can be split into two smaller systems. The separated even/odd parts have 13 and 8 diagonal components, respectively. Some angular momentum configurations are completely non-interacting (forbidden), because the electron angular momenta in these configuration cannot add up to the total angular momentum L. Omission of these 15 rows and columns is an advantageous step for an efficient solution.

A simple algorithm how to choose the contributing angular configurations, ordered in descending order according to importance of their contribution to the dynamics of the system, has been shown in [40]. The (ℓ_1, ℓ_2) pairs are organized into sets with a constant sum, $\ell_1 + \ell_2 = k_L$. As these angular momenta must be able to compose the total angular momentum L, there is a lower bound on the sum, $k_L \geq L$, and upper bound at the difference, $|\ell_1 - \ell_2| \leq L$. In the first group is $k_L = L$ and the electron angular momenta are for a given parity $\Pi \in \{0, 1\}$ the following: (Π, L), $(\Pi + 1, L - 1)$, $(\Pi + 2, L - 2)$, …, (L, Π). In the next group the sum k_L will increase by two so that states with different parity are skipped. The table 4.1 shows examples of this scheme.

There are infinitely many angular momentum groups, because k_L is not bounded by anything from above. For the actual calculation the number is truncated, the total number of different groups considered is denoted by $n_L + 1$. Due to decreasing importance with rising k_L the convergence in n_L is possible. The original algorithm from [40] can be even

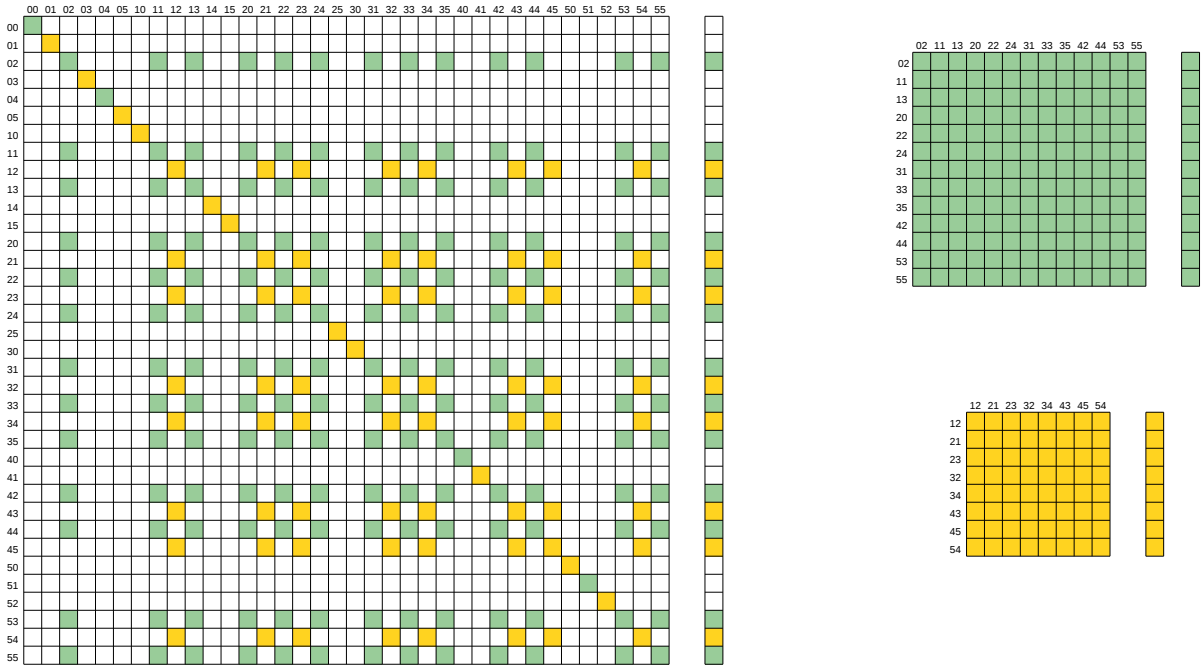

Figure 4.1: Graphical representation of the matrix $(E\mathsf{1} - \mathsf{H})$ of the set of equations, and the right hand side χ, for $L = 2$ and maximal allowed ℓ equal to five. The green colour indicates a natural parity component, i.e. $(-1)^{l_1+l_2+L} = (-1)^{l_1'+l_2'+L} = 1$, and the yellow is an un-natural parity component. White components are zero due to the angular momentum conservation. The two-digit pairs along the borders, $(l_1 l_2)$, denote the angular momenta of the electrons. This system can be split into two independent systems, as shown right.

k_L	Natural parity $\Pi = 0$	Un-natural parity $\Pi = 1$
4	(0,4) (1,3) (2,2) (3,1) (4,0)	(1,4) (2,3) (3,2) (4,1)
5	(1,5) (2,4) (3,3) (4,2) (5,1)	(2,5) (3,4) (4,3) (5,2)
6	(2,6) (3,5) (4,4) (5,3) (6,2)	(3,6) (4,5) (5,4) (6,3)
7	(3,7) (4,6) (5,5) (6,4) (7,3)	(4,7) (5,6) (6,5) (7,4)
...	...	...

Table 4.1: Coupled angular states for $L = 4$ with leading contribution.

improved. Not all angular pairs in a single row corresponding to some n_L are equally important. For example, at high total angular moment L, say $L = 40$, the angular basis will contain (among others) the angular pairs (0,40) and (20,20) for $n_L = 0$. But the situation where both electrons have $\ell_1 = \ell_2 = 20$ is very unlikely compared to the situation where the atomic electron has $\ell_1 = 0$ and the projectile partial wave has $\ell_2 = 40$. It is thus possible to introduce another limiting parameter n_L', which will also ensure that $\ell_1 \leq n_L'$ or $\ell_2 \leq n_L'$. It is possible to seek convergence also with respect to this parameter.

The right-hand side of (4.3) is

$$\chi^{LM}_{\ell_1\ell_2}(r_1, r_2) = \sum_{\ell\lambda} \frac{\sqrt{2\pi(2\ell+1)}}{k_i} \mathrm{i}^\ell C^{LM}_{l_i m_i \ell 0} \left(\chi_{\mathrm{dir}} + (-1)^{S+\Pi}\chi_{\mathrm{exc}}\right), \tag{4.5}$$

$$\chi_{\mathrm{dir}} = f^\lambda_{\ell_1\ell_2 l_i \ell; L} \left(\frac{1}{r_{12}} - \frac{1}{r_2}\right) P_{n_i l_i}(r_1) \hat{j}_\ell(k_i r_2), \tag{4.6}$$

$$\chi_{\mathrm{exc}} = f^{\lambda}_{\ell_1\ell_2\ell l_i;L}\left(\frac{1}{r_{12}} - \frac{1}{r_1}\right)\hat{j}_\ell(k_i r_1)P_{n_i l_i}(r_2)\,, \tag{4.7}$$

where $\Pi = l_i + \ell + L$ is the total conserved parity. Here, l_i is the initial atomic orbital quantum number and ℓ is the projectile partial wave. Apparently, we have a symmetry (or antisymmetry)

$$\chi^{LM}_{\ell_1\ell_2}(r_1, r_2) = (-1)^{S+\Pi}\chi^{LM}_{\ell_2\ell_1}(r_2, r_1)\,. \tag{4.8}$$

Similarly, the solution $\psi^{LM}_{sc,\ell_1\ell_2}(r_1, r_2)$ must be symmetric or antisymmetric, depending on its total spin state and parity. It is then possible to only solve for states with e.g. $\ell_1 \leq \ell_2$; the remaining states with $\ell_1 > \ell_2$ can be obtained by transposition and application of the sign factor $(-1)^{S+\Pi}$. In further text S and Π are added to the labels of ψ and χ.

The importance of the electron-electron multipole potential $V^\lambda = r^\lambda_< / r^{\lambda+1}_>$ in (4.4) decreases with rising multipole moment λ, see the figure 4.2. In the region where r_1 and r_2 are comparable, however, the contribution cannot be neglected ever for high λ. This is an unavoidable feature of the the original singular term $V_{12} = |\mathbf{r}_1 - \mathbf{r}_2|^{-1}$.

4.1.2 Exterior complex scaling

The differential equation (2.11), or its angular expansion (4.3), need a specification of a boundary condition in order to yield a unique solution. In scattering theory the boundary condition is the expression (2.13) or (2.29). The method of the exterior complex scaling (ECS) uses the observation that if we—instead of the real coordinate r—use a complex coordinate $\rho = \mathrm{Re}\,\rho + \mathrm{i}\,\mathrm{Im}\,\rho$ with uniformly increasing positive imaginary part, the resulting expression will be exponentially damped,

$$\mathrm{e}^{\mathrm{i}k\rho} = \mathrm{e}^{\mathrm{i}k\,\mathrm{Re}\,\rho}\mathrm{e}^{-\mathrm{k}\,\mathrm{Im}\,\rho}\,. \tag{4.9}$$

The canonical way how to obtain this complexified coordinate is a rotation of a part of the coordinate axis into the complex plane using the expression (also see fig. 4.3)

$$\rho(r) = \begin{cases} r & [r \leq R_0]\,, \\ R_0 + (r - R_0)\mathrm{e}^{\mathrm{i}\theta_{\mathrm{ECS}}} & [r > R_0]\,. \end{cases} \tag{4.10}$$

The scattering part of the wave function (2.13) (i.e. the second term) subject to the transformation (4.10) rapidly decreases when the distance of the projectile from origin significantly exceeds the radius R_0 in magnitude. In a sufficient distance beyond the turning radius R_0 the function can be considered effectively equal to zero. Also the asymptotic ionization wave function (2.29) contains an oscillatory term, which will behave exactly the same—the oscillations will be transformed to an exponential damp factor. See also the figure 4.4.

When using the ECS approach, the equation (4.3) for $\psi^{LM}_{sc,\ell_1'\ell_2'}$ can be supplemented with the pure Dirichlet boundary condition: we require that the solution is zero when $r_1 = 0$ or $r_2 = 0$ (thanks to separation of the term $\frac{1}{r_1 r_2}$ in (4.1)) and also when $r_1 \geq R_{\max}$ or $r_2 \geq R_{\max}$ (thanks to (4.9)). This allows introduction of a finite basis on the rectangle $(0, R_{\max}) \times (0, R_{\max})$, discretization of the differential operators and ultimate transformation of the problem into a (large) system of linear-agebraic equations.

For completeness, we should note that the *exterior* complex scaling is not the only possible approach. It evolved from the *smooth* complex scaling [41], which, nevertheless, has been recently demonstrated to yield as good results as ECS [42].

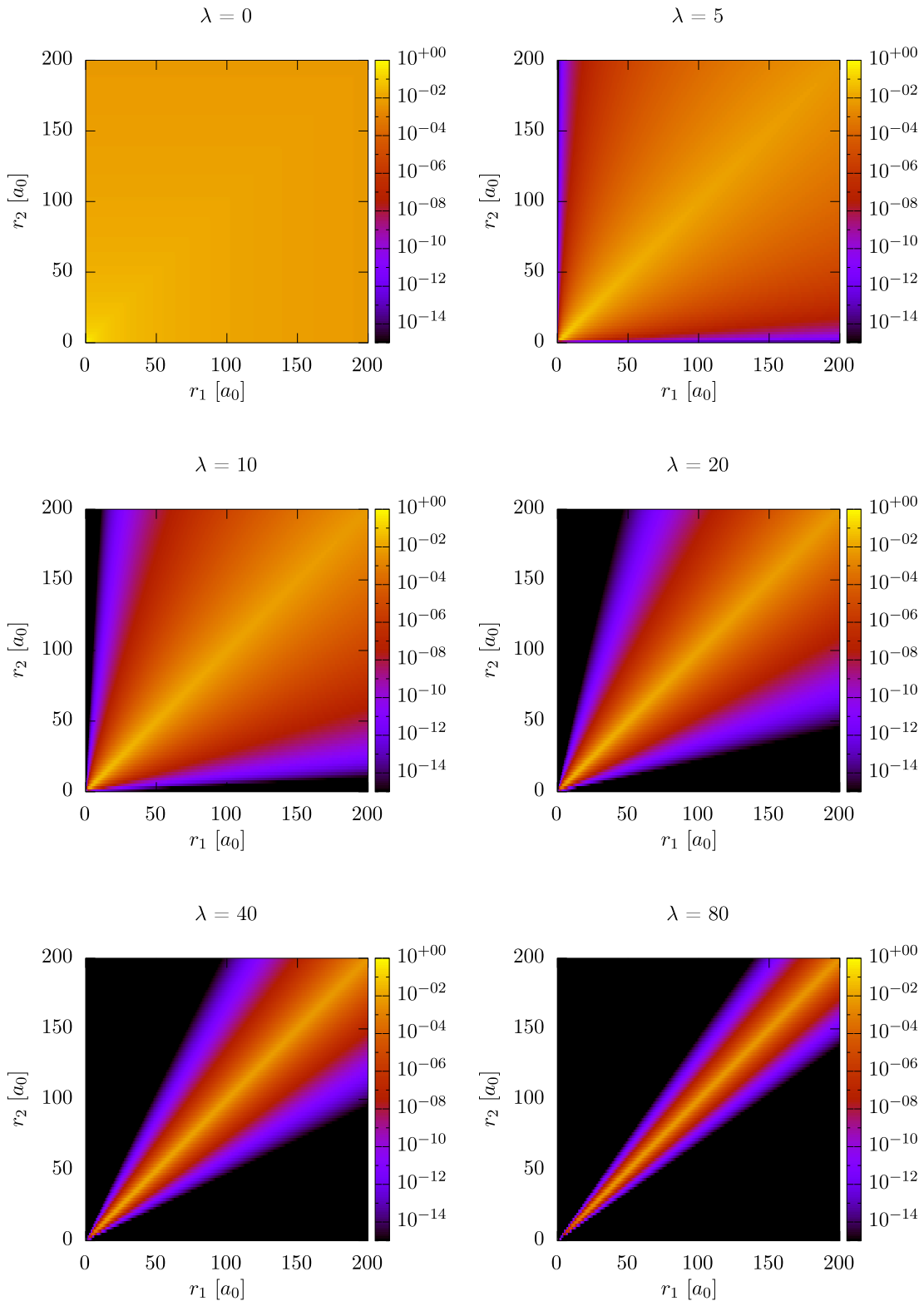

Figure 4.2: Magnitude of the coupling potential $r_<^\lambda / r_>^{\lambda+1}$ for different values of the multipole λ. For high multipoles the contribution comes only from the region where r_1 is comparable to r_2.

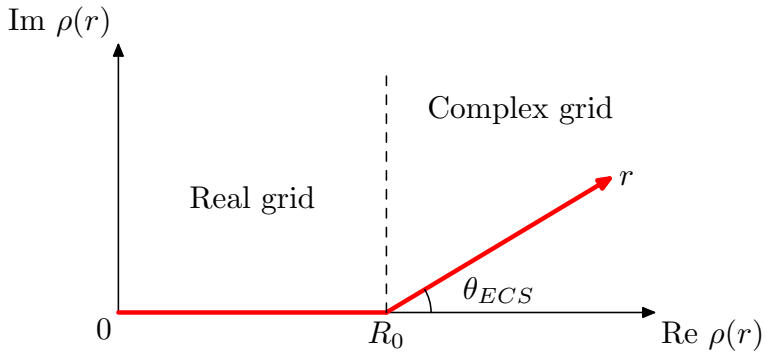

Figure 4.3: Exterior complex scaling contour—the complex-rotated radial coordinate.

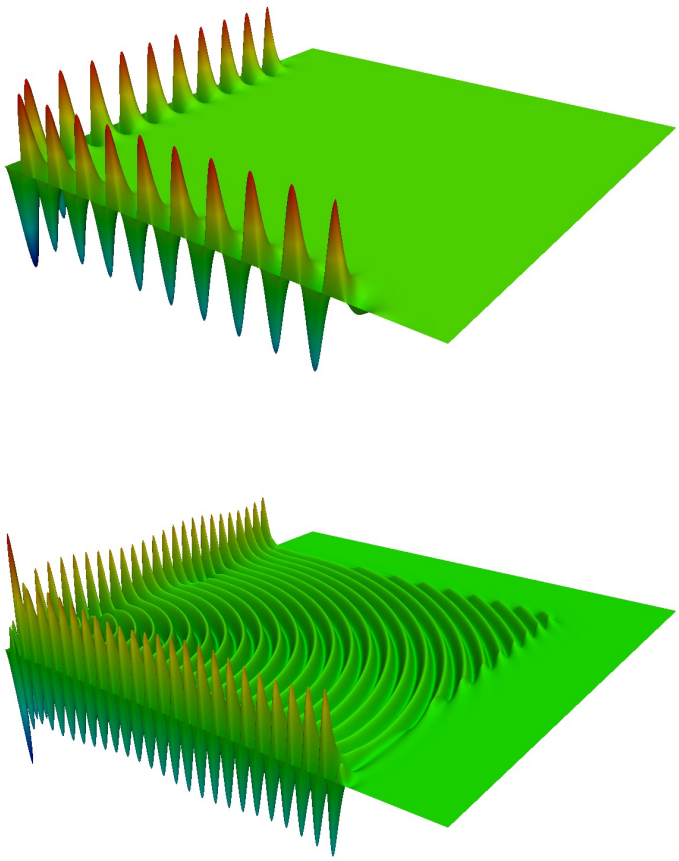

Figure 4.4: A radial part of the two-electron wavefunction for spin $S = 0$ and total angular momentum $L = 0$. The top panel is for total energy $E_{\text{tot}} = -0.4$ Ry, whereas the bottom panel for the total energy $E_{\text{tot}} = 4$ Ry. The notable difference is the oscillation pattern in the right figure that corresponds to non-zero probability of both electrons retreating to continuum. The left figure does not allow that option, it contains only the *evanescent* waves running along the boundaries. See also the discussion in [43].

4.1.3 B-spline basis

B-splines (*basis splines*) are a special class of piecewise polynomial functions of a real variable with compact support. They are defined by their order K and an ordered sequence of knots t_i, $i = 1, \ldots, N_{\mathrm{knot}}$. The mathematical properties of the B-splines have been reviewed by de Boor in [44]. The application of the B-splines in atomic and molecular physics has been discussed by Bachau in [45].

The defining prescription is a recursive formula (called *de Boor formula*)

$$B_i^K(x) = \frac{x - t_i}{t_{i+K} - t_i} B_i^{K-1}(x) + \frac{t_{i+K+1} - x}{t_{i+K+1} - t_{i+1}} B_{i+1}^{K-1}(x)\,, \tag{4.11}$$

with the seed value

$$B_i^0(x) = \begin{cases} 1 & [t_i \le x < t_{i+1}]\,, \\ 0 & \text{otherwise.} \end{cases}$$

The derivative of a B-spline is a combination of B-splines with lower order,

$$\frac{\mathrm{d}}{\mathrm{d}x} B_i^K(x) = \frac{K}{t_{i+K} - t_i} B_i^{K-1}(x) - \frac{K}{t_{i+K+1} - t_{i+1}} B_{i+1}^K(x)\,. \tag{4.12}$$

B-splines are composed of polynomials of degree equal to their order K. For this reason, integration of a product of two B-splines can be done efficiently using the Gauss-Legendre quadrature with number of points equal to the splines' order. Furthermore, the formula (4.11) is friendly to vector processing on modern CPUs (e.g. using AVX instructions); thanks to the simple operations a single B-spline can be effectively evaluated in several points at once if x and $B(x)$ are considered vectors and the operations componentwise. If the knot sequence is non-decreasing, with point multiplicity not exceeding the B-spline order, then all B-splines span exactly $K + 1$ knots or K inter-knot intervals.

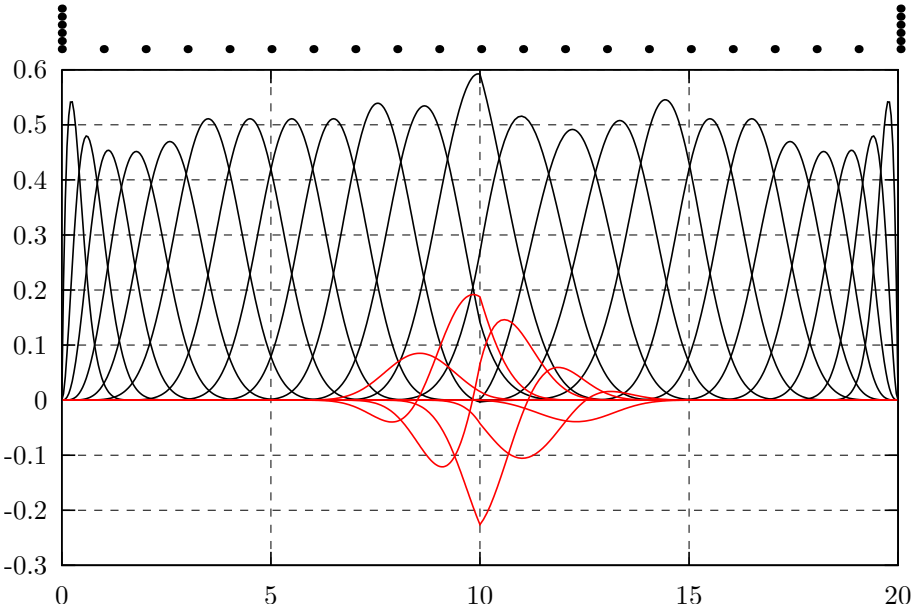

Figure 4.5: Example of a B-spline set of order 6 and knot sequence 0 [6×], 1, 2, 3, 4, 5, 6, 7, 8, 9, 10, $10+1\mathrm{e}^{\mathrm{i}\pi/4}$, $10+2\mathrm{e}^{\mathrm{i}\pi/4}$, $10+3\mathrm{e}^{\mathrm{i}\pi/4}$, $10+4\mathrm{e}^{\mathrm{i}\pi/4}$, $10+5\mathrm{e}^{\mathrm{i}\pi/4}$, $10+6\mathrm{e}^{\mathrm{i}\pi/4}$, $10+7\mathrm{e}^{\mathrm{i}\pi/4}$, $10+8\mathrm{e}^{\mathrm{i}\pi/4}$, $10+9\mathrm{e}^{\mathrm{i}\pi/4}$, $10+10\mathrm{e}^{\mathrm{i}\pi/4}$ [6×]. Real part is black, imaginary part red. The horizontal axis shows the length of the semi-complex coordinate contour, bullets indicate horizontal positions of the knots.

Originally, the knot sequence has been considered only real, but McCurdy and Martín [38] showed that if the knots are chosen along the semi-complex ECS contour (i.e. initially real and beyond R_0 rotated into the complex plane), the resulting set is an excellent basis for the solution of the Schrödinger equation in the ECS method, because it already contains the sharp feature at $\rho = R_0$, which would require much finer basis around $\rho = R_0$ otherwise. Example of such a basis set is presented in the figure 4.5. The discontinuity of the derivative at the turning point $R_0 = 10$ is apparent.

Using this basis is advantageous in the ECS method also due to the fact that it automatically enforces the desired boundary condition: zero at the origin and at the end of the grid. In the present problem the equations are two-dimensional, hence we are using a product basis of the one-dimensional bases. The property of the chosen B-splines then ensures that the solution is zero at the boundary of the grid. Note that to allow different shapes of the solution at the origin ($r_1 = 0$ or $r_2 = 0$), it is necessary to use the maximal knot multiplicity there, i.e. the multiplicity equal to the order of the B-splines.

The matrix elements of various operators can be computed as integrals of B-splines,

$$\langle B_i | B_k \rangle = \int B_i(r) B_k(r) \, \mathrm{d}r = S_{ik} \,,$$

$$\langle B_i | \left(-\frac{\mathrm{d}^2}{\mathrm{d}r^2} \right) | B_k \rangle = + \int \frac{\mathrm{d}B_i(r)}{\mathrm{d}r} \frac{\mathrm{d}B_k(r)}{\mathrm{d}r} \mathrm{d}r = D_{ik} \,,$$

$$\langle B_i | r^\alpha | B_k \rangle = \int B_i(r) r^\alpha B_k(r) \, \mathrm{d}r = M^{(\alpha)}_{ik} \,,$$

$$\langle B_i B_j | \frac{r_<^\lambda}{r_>^{\lambda+1}} | B_k B_l \rangle = \int\int B_i(r_1) B_j(r_2) \frac{r_<^\lambda}{r_>^{\lambda+1}} B_k(r_1) B_l(r_2) \mathrm{d}r_1 \mathrm{d}r_2 = R^\lambda_{ijkl} \,.$$

Using these matrices the equation (4.3) can be written in a matrix form,

$$\sum_{\ell_1' \ell_2'} \mathsf{A}^L_{\ell_1 \ell_2 \ell_1' \ell_2'} \boldsymbol{\psi}^{LMS\Pi}_{sc,\ell_1'\ell_2'} = \boldsymbol{\chi}^{LMS\Pi}_{\ell_1\ell_2} \,, \tag{4.13}$$

where

$$\mathsf{A}^L_{\ell_1 \ell_2 \ell_1' \ell_2'} = \left(E \mathsf{S} \otimes \mathsf{S} - \mathsf{H}_1 \otimes \mathsf{S} - \mathsf{S} \otimes \mathsf{H}_2 \right) \delta^{\ell_1'}_{\ell_1} \delta^{\ell_2'}_{\ell_2} - \sum_\lambda f^\lambda_{\ell_1 \ell_2 \ell_1' \ell_2'; L} \mathsf{R}^\lambda \,, \tag{4.14}$$

$$\mathsf{H}_n = \frac{1}{2}\mathsf{D} + \frac{1}{2}\ell_n(\ell_n+1)\mathsf{M}^{(-2)} - \mathsf{M}^{(-1)}$$

and

$$\boldsymbol{\chi}^{LMS\Pi}_{\ell_1\ell_2} = \sum_{\ell\lambda} \frac{\sqrt{2\pi(2\ell+1)}}{k_i} \mathrm{i}^\ell C^{LM}_{l_i m_i \ell 0} \left(\boldsymbol{\chi}_{\mathrm{dir}} + (-1)^{S+\Pi} \boldsymbol{\chi}_{\mathrm{exc}} \right) , \tag{4.15}$$

$$\boldsymbol{\chi}_{\mathrm{dir}} = f^\lambda_{\ell_1 \ell_2 l_i \ell; L} \left(\mathsf{R}^\lambda - \delta^0_\lambda \delta^{l_i}_{\ell_1} \delta^\ell_{\ell_2} \mathsf{S} \otimes \mathsf{M}^{(-1)} \right) (\mathsf{p} \otimes \mathsf{j}) \,,$$

$$\boldsymbol{\chi}_{\mathrm{exc}} = f^\lambda_{\ell_1 \ell_2 \ell l_i; L} \left(\mathsf{R}^\lambda - \delta^0_\lambda \delta^\ell_{\ell_1} \delta^{l_i}_{\ell_2} \mathsf{M}^{(-1)} \otimes \mathsf{S} \right) (\mathsf{j} \otimes \mathsf{p}) \,,$$

with p and j being the vectors of B-spline expansion of the respective one-dimensional radial function $P_{n_i l_i}(r)$ or $j_\ell(k_i r)$. The block structure of (4.13) has been discussed in the section 4.1.1 and in the figure 4.1.

4.1.4 Extraction of scattering information

Once the solution to the Schrödinger equation is found, it is possible to extract information on the scattering processes that originate from the initial state contained in the right-hand side. For discrete transitions one uses the formula for the T-matrix element

$$T_{fi} = \langle \Psi_f | \mathsf{T} | \Psi_i \rangle = \langle \Psi_f | \mathsf{H}_{\mathrm{int}} | \Psi_i^{(+)} \rangle \,.$$

Thanks to the assumption that the potentials are terminated at the end of the real grid, the radial integrals in the above formula can be terminated at the same radius R_0, too.

$$T_{fi} = \langle \Psi_f | \mathsf{H}_{\mathrm{int}} | \Psi_i^{(+)} \rangle_{R_0} = \langle \Psi_f | \mathsf{H}_{\mathrm{full}} - \mathsf{H}_{\mathrm{free}} | \Psi_i^{(+)} \rangle_{R_0} \,.$$

The stationary scattering state $\Psi_i^{(+)}$ is an eigenstate of $\mathsf{H}_{\mathrm{full}}$ with eigenenergy E_{tot}, so that

$$T_{fi} = \langle \Psi_f | E_{\mathrm{tot}} - \mathsf{H}_{\mathrm{free}} | \Psi_i^{(+)} \rangle_{R_0} \,.$$

In the coordinate representation this can be simplified to

$$T_{fi} = \sum_\ell T_\ell Y_\ell^{m_i - m_f}(\hat{\mathbf{k}}_f) \,, \qquad T_\ell = \sum_L T_\ell^L \,,$$

$$T_\ell^L = \frac{1}{\sqrt{2}} \frac{4\pi}{k_f} \mathrm{i}^{-\ell} C^{Lm_i}_{l_f m_m \ell m_i - m_f} \left(\Lambda_\ell^{(1)Lm_i} + \Lambda_\ell^{(2)Lm_f} \right)$$

$$\Lambda_\ell^{(1)Lm_i} = \int_0^{R_0} P_{n_f l_f}(r_1) \mathcal{W} \left[\psi^{Lm_i}_{\mathrm{sc},l_f,\ell}(r_1, \bullet), \hat{j}_\ell(k_f \bullet) \right]_{R_0} \mathrm{d}r_1 \,,$$

$$\Lambda_\ell^{(2)Lm_i} = \int_0^{R_0} \hat{j}_\ell(k_f r_2) \mathcal{W} \left[\psi^{Lm_i}_{\mathrm{sc},l_f,\ell}(\bullet, r_2), P_{n_f l_f}(\bullet) \right]_{R_0} \mathrm{d}r_2 \,,$$

where $\mathcal{W}[f(x), g(x)]_{x_0} = f'(x_0)g(x_0) - f(x_0)g'(x_0)$ is the wronskian of two functions evaluated at the given point. In the limit $R_0 \to +\infty$ the second radial integral $\Lambda_\ell^{(2)Lm_i}$ is effectively zero, because it is proportional to the hydrogen radial orbital $P_{n_f l_f}$ evaluated at R_0, or to its derivative at that point. In hex-ecs it is neglected.

The extraction of the ionization exmplitude is much more challenging, because the partial wave expansion of (2.29) is complicated. It has been shown, though, that a reasonably good approximation (at least in Ω_0) is an assumption that the final state can be approximated as a product of two non-interacting Coulomb waves, $\phi_1\phi_2$. This is the method known as the Peterkop surface integral [46]. Then we have

$$F(\mathbf{k}_1, \mathbf{k}_2) = \sum_{\ell_1 \ell_2 LM} \mathrm{i}^{-\ell_1 - \ell_2} \mathrm{e}^{\mathrm{i}(\sigma_1 + \sigma_2)} \mathcal{Y}^{LM}_{\ell_1 \ell_2}(\hat{\mathbf{k}}_1, \hat{\mathbf{k}}_2) f^{LM}_{\ell_1 \ell_2}(k_1, k_2) \,, \tag{4.16}$$

$$f^{LM}_{\ell_1 \ell_2}(k_1, k_2) = \frac{2}{\sqrt{\pi}} \frac{\rho}{k_1 k_2} \int_0^{\pi/2} \left(\phi_1 \phi_2 \frac{\partial}{\partial \rho} \psi^{LM}_{\mathrm{sc},\ell_1 \ell_2} - \psi^{LM}_{\mathrm{sc},\ell_1 \ell_2} \frac{\partial}{\partial \rho} \phi_1 \phi_2 \right) \mathrm{d}t \,. \tag{4.17}$$

Whereas the discrete T-matrices are extracted from a line at $(r_1, r_2) = (R_0, r_2)$, the ionization amplitude is extracted from a quarter-circle $(r_1, r_2) = (\rho \cos t, \rho \sin t)$. The hyper-radius ρ is chosen to be equal to R_0. This last oscillatory integral is integrated using the Clenshaw-Curtis quadrature, see Appendix A.

4.2 Implementation

4.2.1 Solution of the linear system

The system (4.13) is generally huge. If there are N basis functions (B-splines) in each dimension and A angular momentum pairs, then the rank of the set of equations is N^2A. For a moderate calculation is $N \approx 10^3$ and $A \approx 10^1$, which gives a rank of 10^7. Such a matrix cannot be solved by a simple application of a LAPACK routine, already for the reason that such a large dense matrix does not fit into commonly available computer memory. Fortunately, thanks to the compact support of the basis functions the matrix is very sparse. The one-electron matrices S, $\mathsf{M}^{(\alpha)}$ and D have $2K+1$ diagonals in the central band, where K is the order of the B-splines. The two-electron matrices R and A have $(2K+1)^2$ diagonals and have a two-level recursive structure: They are composed of blocks, which are either identically zero, or with the same structure as the one-electron matrices. Technically, the structure of the two-electron matrices is the same as the structure of the tensor product of two one-electron matrices. All matrices are symmetric, however indefinite.

The solution algorithm used in hex-ecs is the PCOCG algorithm (preconditioned conjugate orthogonal conjugate gradients) [47], which is a slightly modified standard PCG algorithm (preconditioned conjugate gradients). The only difference between CG and COCG is that the scalar products $\mathsf{a} \cdot \mathsf{b}$, which are in CG computed as $\sum_i a_i^* b_i$, are replaced by non-conjugated $\sum_i a_i b_i$, which enables the algorithm to converge also for non-positive-definite complex symmetric linear systems. The plain CG solution method typically converges for sparse two-dimensional problems in $O(n^{3/2})$ iterations when n is the rank of the matrix [48]. However, the number of iterations can be considerably reduced by preconditioning.

4.2.2 Preconditioning

The preconditioning is done by solution of a simplified system where the coupling between different (ℓ_1, ℓ_2) blocks is neglected. This assumption is equivalent to replacing $\mathsf{A}_{\ell_1\ell_2\ell_1'\ell_2'}$ in equation (4.13) by $\mathsf{A}_{\ell_1\ell_2\ell_1'\ell_2'}\delta_{\ell_1}^{\ell_1'}\delta_{\ell_2}^{\ell_2'}$. The solution of the large linear system of rank N^2A then reduces to solution of A systems of rank N^2. These block-diagonal systems are slightly smaller, though generally still very large for a straightforward direct solution. Hence the iterative method is employed here for the second time. And again with a preconditioner.

A standard choice of the nested preconditioner is the incomplete LU factorization and back-substitution [49]. The factorization is done once before the iterative solver starts, and then reused on every preconditioner application. In hex-ecs one can choose from several options when using the ILU preconditioner. The factorization can be done by MUMPS [50], PARDISO [51], UMFPACK [52], SuperLU [53] or SuperLU_DIST [54]. All these libraries use similar workflow: the matrix is analyzed and permuted, so that the fill-in (number of new non-zero elements in LU factors) will be as low as possible, and then decomposed into the L and U factors. In the case of the *incomplete* LU factorization elements outside of the sparse pattern of the original matrix are compared to a given tolerance and dropped if their magnitude falls below the tolerance. This action reduces the memory required to hold the LU factors, though introducing irregularity in the memory storage and hence preventing vectorization of the linear-algebraic operations. The existing decomposition can be then used for fast solution of the linear system with varying right-hand sides. Note that—depending on the drop tolerance used—the ILU preconditioner is

very efficient and mostly results only in a single iteration of the nested conjugate gradients, hence effectively in a direct solution of the preconditioner system.

The figure 4.6 compares factorization and running times for a particular setup dominated by outer region (see the section "Channel reduction") for different LU decomposition libraries. The properties of the individual libraries in calculations dominated by the inner region are demonstrated in the next figure 4.7. General conclusion is that the PARDISO solver is fastest, whereas the UMFPACK library produces smallest LU factors.

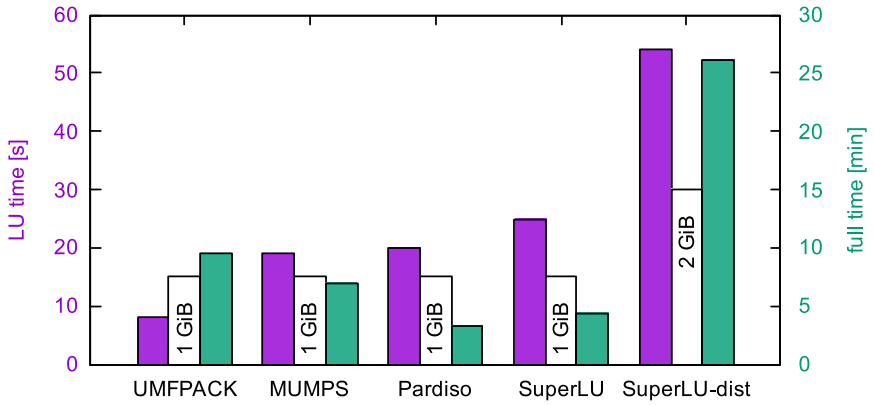

Figure 4.6: Comparison of numerical performance of various LU decomposition numerical libraries for an outer-region-dominated calculation. The test calculation is as in the last row of table 4.3, only with angular momenta limited to $\ell_{1,2} \leq 3$. The "LU time" is the time for LU decomposition of the largest $\ell_1 = \ell_2 = 0$ block of rank 3'886'188, while the "full time" is the LU-backsubstitution-dominated running time of the iterative solver for the whole system of rank 7'865'688. The gigabytes (white columns) indicate the memory consumed by the LU factorization of the first diagonal block.

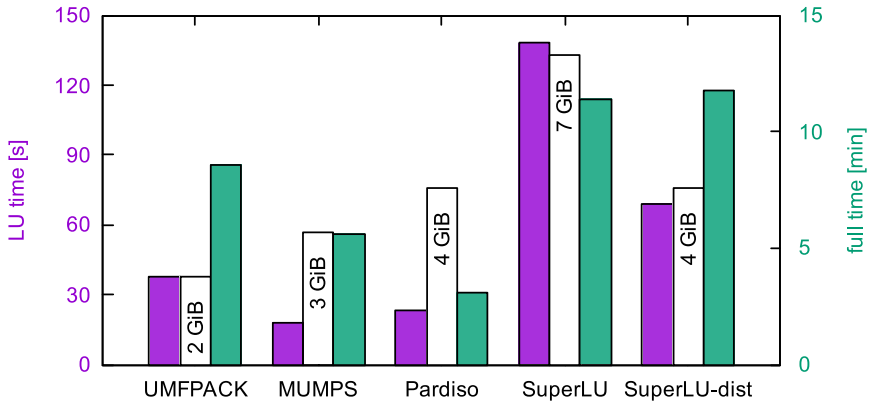

Figure 4.7: Comparison of numerical performance of various LU decomposition numerical libraries for an inner-region-dominated calculation. The test calculation is as in the second row of table 4.3, only with angular momenta limited to $\ell_{1,2} \leq 3$. Here, the rank of the first diagonal block was 289'444 and of the full hamiltonian 1'157'776.

4.2.3 Kronecker product approximation preconditioner

Even though the preparational step with fill-in reducing permutations is done, the LU factors can easily overgrow the available computer memory. For this reason an alternative

preconditioner has been implemented. Here it is called *Kronecker product approximation* (KPA) and its idea lies in the observation that if the two-electron term containing R^λ is neglected in (4.14), then there are only Kronecker products in the diagonal block $\mathsf{A}^L_{\ell_1\ell_2\ell_1\ell_2}$ and those can be simultaneously diagonalized by suitable similarity transform, see also [55] and [56]

$$\mathsf{A}^L_{\ell_1\ell_2\ell_1\ell_2} \approx \left(\mathsf{S}^{1/2}\mathsf{C}_1^{-1} \otimes \mathsf{S}^{1/2}\mathsf{C}_2^{-1}\right) \left(E\mathsf{1}\otimes\mathsf{1} - \mathbf{\Lambda}_1\otimes\mathsf{1} - \mathsf{1}\otimes\mathbf{\Lambda}_2\right) \left(\mathsf{C}_1\mathsf{S}^{1/2} \otimes \mathsf{C}_2\mathsf{S}^{1/2}\right),$$

where

$$\mathsf{S}^{-1/2}\mathsf{H}_n\mathsf{S}^{-1/2} = \mathsf{C}_n^{-1}\mathbf{\Lambda}_n\mathsf{C}_n\,.$$

The diagonalization of $\mathsf{S}^{-1/2}\mathsf{H}_n\mathsf{S}^{-1/2}$ is done by the standard LAPACK routine `zgeev`, inversion of matrices by the tandem `zgetrf` & `zgetri`. The simplified and factored $\mathsf{A}^L_{\ell_1\ell_2\ell_1\ell_2}$ can be easily inverted, because the participating matrices are only of rank N, which is the number of B-splines in one dimension. The approximate solution of the system $\mathsf{A}^L_{\ell_1\ell_2\ell_1\ell_2}\mathsf{z} = \mathsf{r}$ is then

$$\mathsf{z} \approx \left(\mathsf{S}^{-1/2}\mathsf{C}_1^{-1} \otimes \mathsf{S}^{-1/2}\mathsf{C}_2^{-1}\right) \left(E\mathsf{1}\otimes\mathsf{1} - \mathbf{\Lambda}_1\otimes\mathsf{1} - \mathsf{1}\otimes\mathbf{\Lambda}_2\right)^{-1} \left(\mathsf{C}_1\mathsf{S}^{-1/2} \otimes \mathsf{C}_2\mathsf{S}^{-1/2}\right)\mathsf{r}\,. \quad (4.18)$$

The application of a Kronecker product on a vector, $(\mathsf{A}\otimes\mathsf{B})\cdot\mathsf{v}$, is a very efficient operation which requires only two matrix-matrix multiplications when the vector is reshaped to a matrix form by columns,

$$\mathsf{w} = (\mathsf{A}\otimes\mathsf{B})\cdot\mathsf{v} \quad \leftrightarrow \quad \mathsf{W} = \mathsf{A}\mathsf{V}\mathsf{B}^\top\,. \quad (4.19)$$

This relation reduces the number of floating point multiplications from N^4 to $2N^3$, which is a great speed-up. Translating (4.18) into the matrix notation using (4.19) and $\mathsf{Z} = \mathrm{mat}(\mathsf{z})$, $\mathsf{R} = \mathrm{mat}(\mathsf{r})$, $\mathsf{D} = \left(E\mathsf{1}\otimes\mathsf{1} - \mathbf{\Lambda}_1\otimes\mathsf{1} - \mathsf{1}\otimes\mathbf{\Lambda}_2\right)^{-1}$ we get

$$\begin{aligned}\mathsf{Z} &= \mathsf{S}^{-1/2}\mathsf{C}_1^{-1}\left[\mathsf{D}\left(\mathsf{C}_1\mathsf{S}^{-1/2}\,\mathsf{R}\,\mathsf{S}^{-1/2\top}\mathsf{C}_2^\top\right)\right]\mathsf{C}_2^{-\top}\mathsf{S}^{-1/2\top}\\ &= \mathsf{F}\,\mathsf{R}\,\mathsf{S}^{-1}\,, \qquad \mathsf{F} = \mathsf{S}^{-1/2}\mathsf{C}_1^{-1}\mathsf{D}\mathsf{C}_1\mathsf{S}^{-1/2}\,.\end{aligned}$$

4.2.4 Preconditioner performance

The effectivity of the preconditioners varies with the impact energy. The angular coupling, which is neglected by the main block-diagonal preconditioner, becomes very important around the ionization threshold. For energies close to the threshold the convergence will be very slow. The figure 4.8 shows performance of the COCG method when the inversion of diagonal blocks is used as the preconditioner. It would be possible to include the off-diagonal blocks, or some of them, in the preconditioner to increase its effectivity. This would, however, lead to solution of the huge full-rank matrix of the two-dimensional system. The figure 4.9 shows the number of iterations for various number of multipole moments considered in the off-diagonal blocks. The LU factorization (and its subsequent application) of the full-rank matrix is done by the library MUMPS [50], which, unlike both UMFPACK and SuperLU, offers also out-of-core mode, so that the LU factors do not need to fit in computer memory and are stored in temporary files on the disk.

The nested KPA preconditioner performs well if the electrons are not interacting too much. This is violated in vicinity of all thresholds, for which the electron-electron correlation is very important. The figure 4.10 shows number of nested PCOCG iterations needed to invert the $(0,0)$ block for a specific energy and basis.

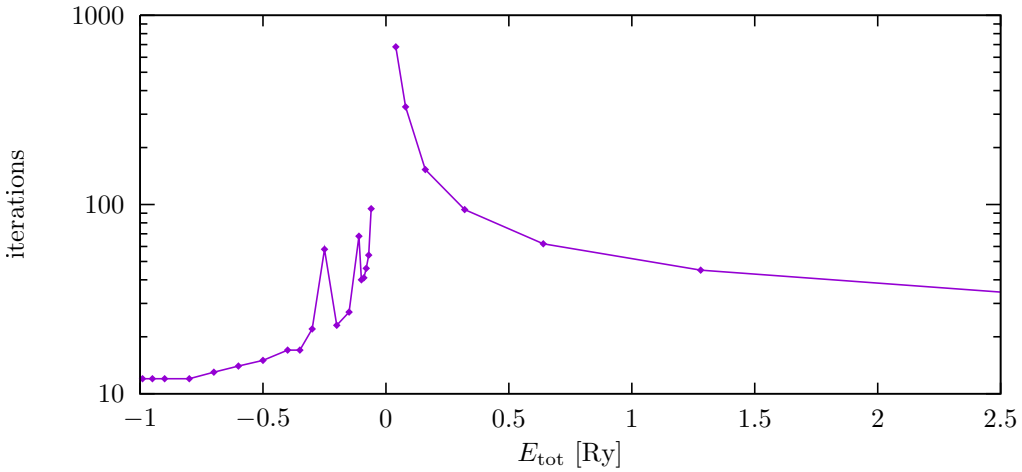

Figure 4.8: Preconditioner iterations: Iterations of COCG needed for convergence of the whole scattering wave solution of a sample setup at different energies. The number diverges around the ionization threshold. This curve does not depend very much on the specific initial state; the convergence character is rather a property of the matrix of the equations and its eigenspectrum.

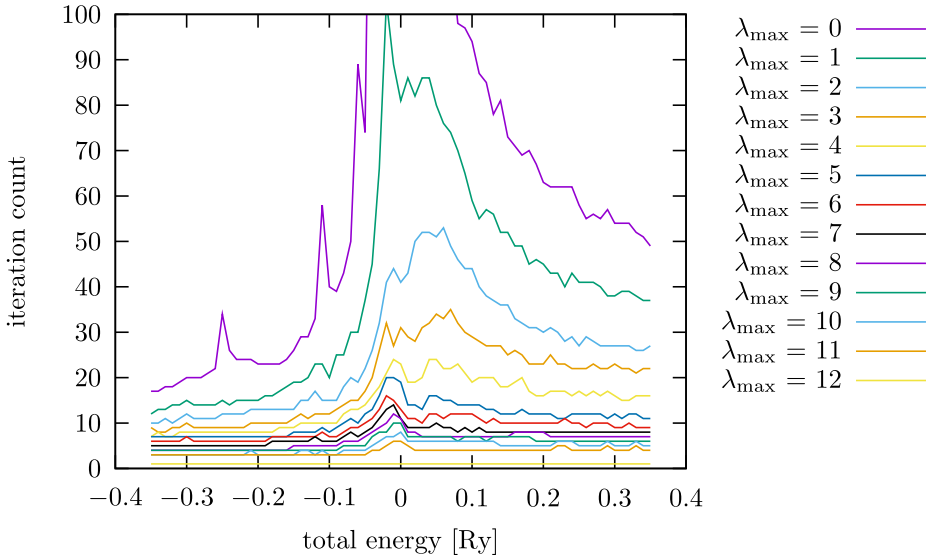

Figure 4.9: Number of COCG iterations needed to converge a solution when off-diagonal multipole blocks R^{λ} up to a given $\lambda_{\max}$ are included in the preconditioner. The importance of the multipoles decreases only slowly, cf. fig 4.2, and does not outweigh the construction cost of the coupled ILU preconditioner. Note however that the inclusion of $\lambda = 1$ (i.e. dipole coupling, which is responsible for polarization) significantly reduces the iteration count in the vicinity of the thresholds: The peaks at -0.25, $-0.111...$ and -0.0625 Ry disappear.

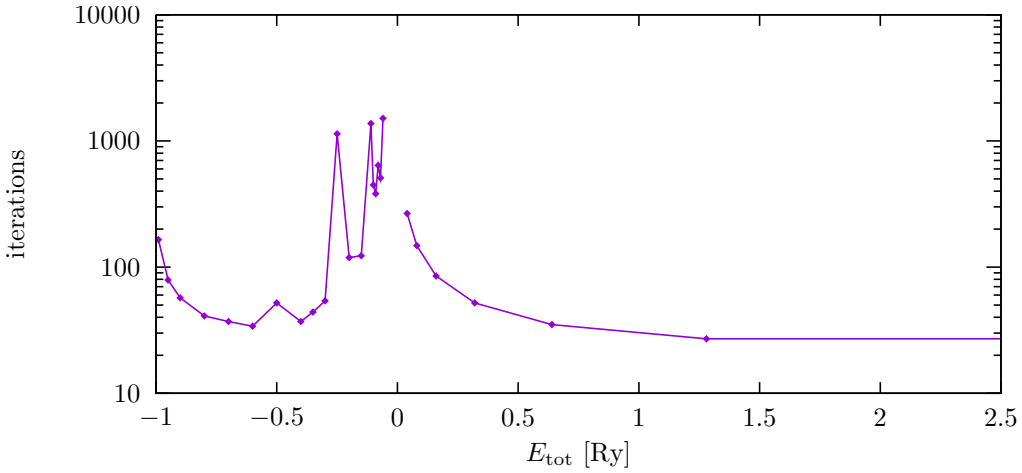

Figure 4.10: Nested (KPA) preconditioner iterations: Iterations of COCG needed for a convergence of the $(0, 0)$ segment of the scattering wave solution for a given initial state and other input parameters. The number diverges in the vicinity of excitation thresholds, which, unfortunately, means that is is relatively high in the whole resonance region.

The total solution time depends on the number of iterations of the main block-diagonal linear solver. Every iteration includes many KPA- (or a few ILU-) -preconditioned nested iterations. Apparently, when KPA is used, the total time will be proportional to the product of the two curves in figures 4.8 and 4.10. That number is low in the extremely low-energy region (below the first threshold) and in the intermediate-energy region (above the ionization threshold). In the resonance region (i.e. total energies from approximately -0.3 Ry to 0 Ry) the ILU preconditioner is more useful, despite its huge memory requirements.

The KPA preconditioner is effective when the electron-electron interaction is not dominant. This is the case for high energies and for high partial waves (angular momenta); the average electron separation is then large and the interaction is suppressed accordingly. Also, due to the fact that the electron-electron interaction is strongest along the line $r_1 = r_2$, the configurations with either $S = 1$ or $\Pi = 1$ are easier to solve than the rest. For these quantum numbers the wave function is antisymmetrical with respect to the exchange of the particles and hence equal to zero on the diagonal $r_1 = r_2$, reducing the magnitude of the interaction.

4.2.5 Parallelization

To make the solution faster it is necessary to distribute the computational work among several processing units. The program can run (a) in a single-thread mode, (b) in a shared memory mode on several cores (or processors) of a single node and (c) in a distributed mode on several communicating nodes.

The shared memory mode is implemented through the OpenMP standard. Optimally, hex-ecs uses the OpenBLAS [57] library, which contains parallelized BLAS and LAPACK routines and many of them are heavily optimized; the numerical kernels are written in assembly language, specifically tailored for each common processor model. The libraries UMFPACK and SuperLU can take advantage of multi-core machines as well; the first one only through OpenBLAS, the second even by itself. OpenMP parallelization allows access to more computing power; however, in large-scale calculations it is often necessary to access also more memory than a single node can offer.

The cross-node parallelization is done using the standard MPI model. The program is launched in several copies on several nodes and these instances communicate with each other and share work. The present model in hex-ecs is the following: There are n_g equal-sized groups containing n_p processes, altogether $n_g n_p$ processes. All processes within the group work on the same block-rows of the matrix $\mathsf{A}^L_{\ell_1\ell_2\ell_1'\ell_2'}$ and corresponding segments $\boldsymbol{\psi}_{sc,\ell_1\ell_2}$ and $\boldsymbol{\chi}_{\ell_1\ell_2}$ of the solution and the right-hand side, respectively; they store the same data. They evenly divide simple operations and synchronize the results among the group afterwards. The concept of a group is used due to the library SuperLU_$DIST$, which allows several processes (= the group) to work on the LU factorization of a single matrix. During the preconditioning step the groups are independently working on the solution of diagonal block systems associated to them. The only non-trivial cooperation among the groups comes in the multiplication by the whole block matrix.

The parallel efficiency on multicore processor is illustrated in the left panel of the figure 4.11. The program can also run on GPUs; comparison of GPU vs CPU timing is done in the right panel of the same figure.

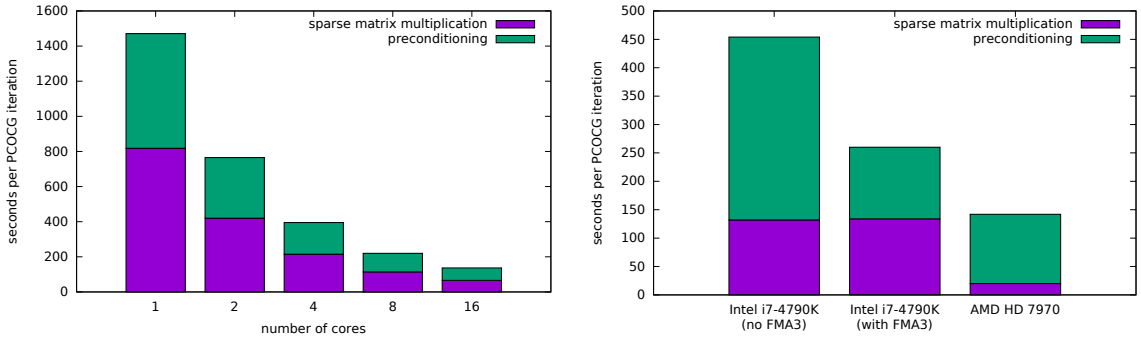

Figure 4.11: Performace of the program on various platforms: Left panel compares run times on increasing number of cores of an Ivy Bridge-class Xeon processor. Right panel compares run times on consumer Haswell-class i7 processor to a common GPU.

4.3 Radial convergence

Even though the atomic orbitals are asymptotically exponentially vanishing, the convergence of scattering amplitudes with the increasing R_0 is not as fast as one might hope. The reason is that the multipole effective potentials stemming from the multipole expansion of the electron-electron interaction, see (4.5) and (4.4), decrease with a power of the radial coordinate and much larger radii need to be considered so that one can obtain converged results.

Another way of seeing this situation comes from the notion of the Helmholtz problem (2.12). The right-hand side χ_i acts as a "source" of the complex "field" Ψ^+_{sc}. If χ_i cannot be neglected to a large distance, the "field" Ψ^+_{sc} will not stabilise until reaching large distances from the scattering centre. But this is not enough. For the quantum scattering it is also necessary to obtain converged angular expansion components $\psi_{\ell_1\ell_2}$ of Ψ^+_{sc} defined in (4.1). But these components again interact through multipole potentials. So the six-dimensional Helmholtz problem (2.12) can be rewritten as a set of two-dimensional Helmholtz problems for fields with a continuous source and where each field acts as a

source for other fields to large distances,

$$(\triangle + k^2_{\ell_1\ell_2}(r_1, r_2))\psi_{\ell_1\ell_2} = \chi_{\ell_1\ell_2} + \sum_{(\ell'_1,\ell'_2)\neq(\ell_1,\ell_2)} W_{\ell_1\ell_2\ell'_1\ell'_2}\psi_{\ell'_1\ell'_2}\,. \tag{4.20}$$

The radial convergence must encompass the effect of the right-hand side in (4.20).

4.3.1 S-model

In the case of an "S-model", i.e. a calculation where all angular momenta are set to zero, no long-range multipole potentials arise. Let us assume that we are looking for the solution of the ECS scattering equations for $L = \Pi = S = 0$, $n_L = 0$, initial state $1s$ and impact energy $E_i = 2$ Ry. Only the angular momentum pair $(0, 0)$ contributes to this calculation. The right-hand side has the form

$$\chi_{00}(r_1, r_2) = \left(\frac{1}{r_>} - \frac{1}{r_2}\right) P_{1s}(r_1) \sin k_i r_2 + (1 \leftrightarrow 2)\,,$$

If we take the limit $r_2 \to +\infty$, the function χ_{00} either becomes identically zero when $r_1 < r_2$ or exponentially decreases if we keep $r_1 > r_2$. In other words it mimics a short-range potential contribution. The extracted scattering quantities converge very fast with grid size in such a case, see the figure 4.12.

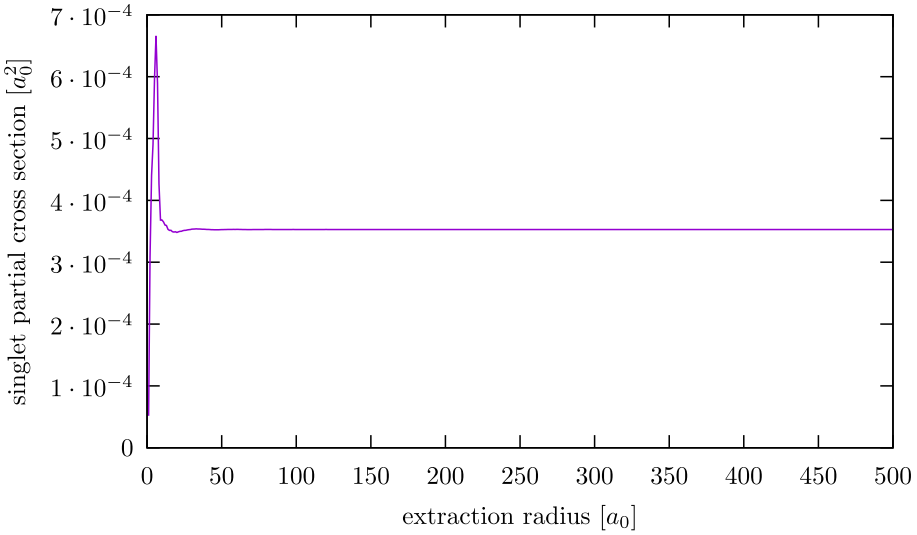

Figure 4.12: Radial convergence of extracted cross section for S-model scattering transition H($1s$) to H($10s$) at impact energy $E_i = 2$ Ry.

4.3.2 Higher angular momenta

Now assume that we raise n_L to 1, i.e. include the angular state $(1, 1)$. Then the right-hand side receives a new component

$$\chi_{11}(r_1, r_2) = -\frac{1}{\sqrt{3}}\frac{r_<}{r_>^2} P_{1s}(r_1) \sin k_i r_2 + (1 \leftrightarrow 2)\,.$$

This other component decreases as

$$\chi_{11}(r_1, r_2) \sim \frac{A}{r_2^2} \sin k_i r_2\,,$$

where $A = -\frac{1}{\sqrt{3}} r_1 P_{1s}(r_1)$ is a bounded function of r_1. The function χ_{11} corresponds to a long-range potential and the truncation of the right-hand side at R_0 leads to an error that diminishes with the power of the distance R_0. A similar effect as in the right-hand side takes place also in the the matrix of the set of equations, which contains the multipole potentials as well.

There are several ways how to compensate this loss of information, which are presented in the next three sections.

4.3.3 Potential splitting

One could take the asymptotic form of the potential, correct the initial and final states to account for this long-range interactions, and then solve the scattering between these modified, *distorted*, asymptotic states only on the remaining short-range (or at least more quickly decaying) potential. A similar operation has been done for ECS in [58] and [59], where the long-range direct Coulomb interaction for ionic targets has been separated.

Because the angular momentum pair coupling is what we would like to separate, one would need to solve practically the same two-dimensional system for the distorted initial and final states as for the scattered waves, as it has been done, illustratively, in [60]. The only difference would be a potential cut-off. Moreover, the distorted wave equations would need to involve even larger physical space than the scattering equations to result in correct asymptotic states. There is no benefit in such an approach.

4.3.4 Extrapolation

The slow radial convergence of the scattering amplitude can be resolved by extrapolation. When extrapolating, we assume that the dependence of the T-matrix (or the scattering amplitude) on the truncation radius is asymptotically

$$T_{fi,\ell}(R_0) \to T_{fi,\ell} + cR_0^{-1} + O(R_0^{-2})\,.$$

For asymptotic T-matrix it is then

$$T_{fi,\ell} \to \frac{R_0' T_{fi,\ell}(R_0') - R_0 T_{fi,\ell}(R_0)}{R_0' - R_0}\,,$$

which should converge considerably faster than $T_{fi,\ell}(R_0)$ alone. It has been noted in [40] that if sufficiently large grid is used to calculate the solution, then the extrapolation can be done by extracting T-matrices from this single solution at various radii, rather than calculating a whole set of solutions with varying grid size. This speeds up the methodology immensely.

The actual algorithm implemented in hex-ecs uses simple linear regression applied on the T-matrix as a function of the inverse extraction radius, see the figure 4.13. However, extrapolation of the extracted amplitude is only useful when evaluating excitations from low states to high states; otherwise the calculated wave function lacks important contributions from far distances.

4.3.5 Channel reduction

This is a very powerful method, which has been published in **[61]**. The grid still needs to be stretched very far; however, the method reduces the dimensionality of the problem

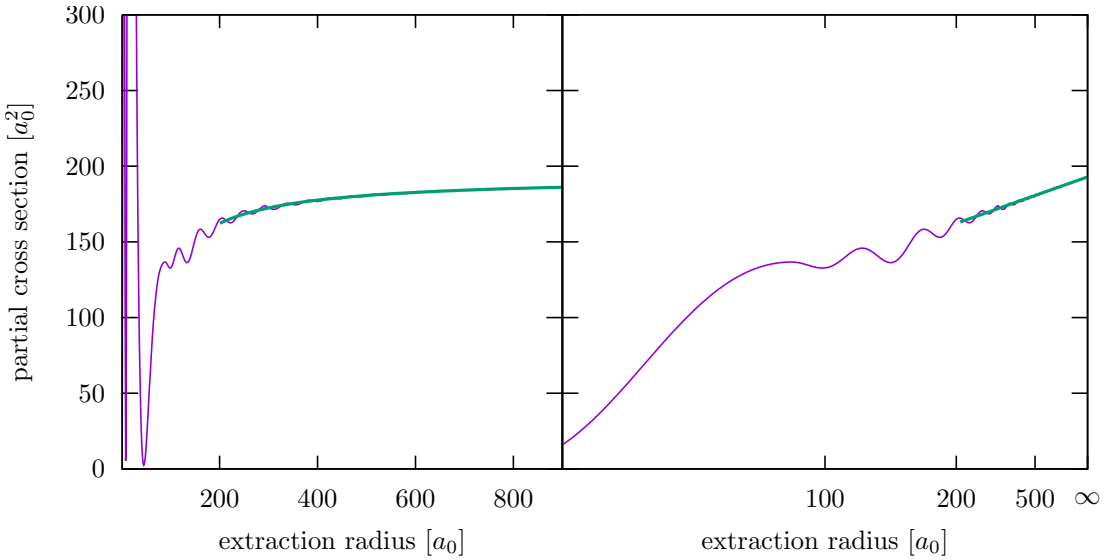

Figure 4.13: Radial extrapolation of cross sections for elastic scattering on H($2s$) at impact energy $E_i = 0.05$ Ry, for $L = S = \Pi = 0$, $n_L = 10$. The two plots show the same function of radial distance, only for different mapping of the horizontal axis: on the right panel it is changed so that the $1/r$ dependence transforms to a straight line.

and so the long grid does not pose any problem. Unfortunately, a channel reduction is possible only for total energies below (or around) the ionization threshold.

In asymptotic distances, where $r_2 \ll r_1 \to +\infty$ or $r_1 \ll r_2 \to +\infty$, the electrons become distinguishable and the atomic electron, which is bound to the nucleus, has to be in one of the energy-allowed atomic states. It is then

$$\psi^{LMS}_{\mathrm{sc},\ell_1\ell_2}(r_1,r_2) \to \begin{cases} \displaystyle\sum_{m=1}^{N_c^{(1)}} F^{(1)}_{m\ell_1}(r_1) P_{m\ell_2}(r_2) & [r_1 \to +\infty]\,, \\ \displaystyle\sum_{n=1}^{N_c^{(2)}} P_{n\ell_1}(r_1) F^{(2)}_{n\ell_2}(r_2) & [r_2 \to +\infty]\,, \\ 0 & [r_1, r_2 \to +\infty]\,, \end{cases} \tag{4.21}$$

where $P_{nl}(r) = rR_{nl}(r)$ is the hydrogen bound state radial function multiplied by the radius, $F^{(a)}_{nl}(r)$ is the corresponding (unknown) projectile channel function for asymptotic $r_a \to +\infty$ and $N_c^{(a)}$ is the number of open scattering channels. The summation over m and n includes only energetically allowed states, i.e. states with energy lower than the total energy E_{tot}. Note that the channel functions $F^{(a)}_{nl}$ should actually bear all the indices of $\psi^{LMS}_{\mathrm{sc},\ell_1\ell_2}$, because they are unique for each of these angular components. However, most of the discussion deals with a single block for given angular momenta, so we use a simplified notation without these indices.

The asymptotic forms (4.21) can be plugged into the scattering equation (4.3), resulting in (for $r_1 \to +\infty$)

$$\left[(E_{\mathrm{tot}} - E^{\mathrm{at}}_m) - T_{\ell_1}\right] F^{(1)}_{n\ell_1} = \xi^{(1)}_{n\ell_2} + \sum_{\substack{\ell_1'\ell_2' m \\ \lambda>0}} f^{\lambda}_{\ell_1\ell_2\ell_1'\ell_2';L} \frac{\rho^{\lambda}_{n\ell_2,m\ell_2'}}{r^{\lambda+1}} F^{(1)}_{m\ell_1'}\,, \tag{4.22}$$

where

$$\xi^{(1)}_{n\ell_2}(r_1) = \int P_{n\ell_2}(r_2)\, \chi^{LMS}_{\ell_1\ell_2}(r_1, r_2)\, \mathrm{d}r_2 \tag{4.23}$$

and

$$\rho^{\lambda}_{n\ell_2,m\ell'_2} = \int P_{n\ell_2}(r_2)\, r_2^{\lambda}\, P_{m\ell'_2}(r_2)\, \mathrm{d}r_2\,, \tag{4.24}$$

or similarly

$$\left[(E_{\mathrm{tot}} - E^{\mathrm{at}}_n) - T_{\ell_2}\right] F^{(2)}_{m\ell_2} = \xi^{(2)}_{m\ell_1} + \sum_{\substack{\ell'_1\ell'_2 n \\ \lambda>0}} f^{\lambda}_{\ell_1\ell_2\ell'_1\ell'_2;L} \frac{\rho^{\lambda}_{m\ell_1,n\ell'_1}}{r^{\lambda+1}} F^{(2)}_{n\ell'_2} \tag{4.25}$$

for the other asymptotics ($r_2 \to +\infty$).

The proposition (4.21) is satisfied very accurately already for moderate distances, because all energetically forbidden channels F_n exponentially decrease with the distance and only the asymptotically allowed states P_{nl} remain in the expansion. If there is a distance R_a where (4.21) is satisfactorily accurate, it is possible to solve the problem (4.3) only for radii smaller than R_a and the equations (4.22) and (4.25) only beyond the dividing radius R_a. The only remaining question is that of the boundary conditions, for which we will use ECS, and of the continuity, which is discussed further in the B-spline framework.

Let us consider the B-spline expansion of the radial functions:

$$\psi^{LMS}_{\mathrm{sc},\ell_1\ell_2}(r_1, r_2) = \sum_{k,l=1}^{N} B_k(r_1) B_l(r_2) \psi^{LMS}_{\mathrm{sc},\ell_1\ell_2,kl}\,, \tag{4.26}$$

$$F^{(1)}_{m\ell_1}(r_1) = \sum_{k=1}^{N} B_k(r_1) F^{(1)}_{m\ell_1,k}\,, \tag{4.27}$$

$$F^{(2)}_{n\ell_2}(r_2) = \sum_{l=1}^{N} B_l(r_2) F^{(2)}_{n\ell_2,l}\,. \tag{4.28}$$

Every B-spline in a basis overlaps with $2K$ other B-splines, where K is the B-spline order. The full problem knot sequence is chosen along an ECS contour, i.e. knots are real up to some sufficiently large $R_0 \gg R_a$, where the multipole coupling can be neglected, and complex with geometrically increasing distances until the point where all outgoing waves are effectively damped by ECS to the numerical zero. Now assume that approximately N_0 leading B-splines fit into the inner radius R_a. This will be the "inner basis". All further B-splines are considered the "outer" basis. There is $N_1 = N - N_0$ outer B-splines. The overlapping B-splines offer a simple means of enforcing the continuity between the inner and outer regions.

By projecting the equation (4.3) on the product $B_i(r_1)B_j(r_2)$ and the one-dimensional equations (4.22) and (4.25) on $B_i(r_1)$ and $B_j(r_2)$, respectively, we obtain a triplet of

matrix equations in the full B-spline basis,

$$\sum_{\ell_1'\ell_2'}\sum_{k,l=1}^{N} A^{L}_{\ell_1\ell_2\ell_1'\ell_2',ijkl}\,\psi^{LMS}_{\mathrm{sc},\ell_1'\ell_2',kl} = \chi_{\ell_1\ell_2,ij}\,, \tag{4.29}$$

$$\sum_{\ell_1'\ell_2'}\sum_{m=1}^{N_c^{(1)}}\sum_{k=1}^{N} B^{(1)}_{\ell_1\ell_2\ell_1'\ell_2',mn,kl}F^{(1;\ell_1',\ell_2')}_{m\ell_1',k} = \xi^{(1;\ell_1,\ell_2)}_{n\ell_2,l}\,, \tag{4.30}$$

$$\sum_{\ell_1'\ell_2'}\sum_{n=1}^{N_c^{(2)}}\sum_{l=1}^{N} B^{(2)}_{\ell_1\ell_2\ell_1'\ell_2',mn,kl}F^{(2;\ell_1',\ell_2')}_{n\ell_2',l} = \xi^{(2;\ell_1,\ell_2)}_{m\ell_1,k}\,. \tag{4.31}$$

Typically, the solution vector $\psi^{LMS}_{\mathrm{sc},\ell_1'\ell_2',kl}$ is found by a straightforward solution of the coupled set (4.29). However, the three sets (4.29)–(4.31) can be combined into a single system that is mostly much *smaller* than (4.29) alone when the assumption (4.21) is used. The B-spline equivalents of (4.21) are

$$\psi^{LMS}_{\mathrm{sc},\ell_1\ell_2,kl} = \sum_{m=1}^{N_c^{(1)}} F^{(1)}_{m\ell_1,k}P_{m\ell_2,l} \qquad [k \gtrsim N_0]\,, \tag{4.32}$$

$$= \sum_{n=1}^{N_c^{(2)}} P_{n\ell_1,k}F^{(2)}_{n\ell_2,l} \qquad [l \gtrsim N_0]\,, \tag{4.33}$$

$$= 0 \qquad [k,l \gtrsim N_0]\,.$$

These relations have a simple inversion originating in orthogonality $\sum_{i,j=1}^{N_0} P_{m\ell,i}S_{ij}P_{n\ell,j} = \delta_{mn}$ of the hydrogen orbitals:

$$F^{(1)}_{m\ell_1,k} = \sum_{i,j=1}^{N_0} P_{m\ell_2,i}S_{ij}\psi^{LMS}_{\mathrm{sc},\ell_1\ell_2,kj} \qquad [k \gtrsim N_0]\,, \tag{4.34}$$

$$F^{(2)}_{n\ell_2,l} = \sum_{i,j=1}^{N_0} P_{n\ell_1,j}S_{ij}\psi^{LMS}_{\mathrm{sc},\ell_1\ell_2,il} \qquad [l \gtrsim N_0]\,. \tag{4.35}$$

The summation can be truncated already at N_0 due to exponential decay of the orbitals. The matrix S_{ij} is the overlap matrix of the B-spline basis, $S_{ij} = \int B_i(r)B_j(r)\mathrm{d}r$.

Having these relations between the full and asymptotic solutions we can now choose the following subset from the equations (4.29)–(4.31), where we suppressed the angular summations and indices:

$$\begin{aligned}\forall i,j = 1,\ldots,N_0:\quad \chi_{ij} &= \sum_{k,l=1}^{N_0} A_{ijkl}\psi_{kl} \\ &+ \sum_{k=N_0+1}^{N_0+K}\sum_{l=1}^{N_0}\sum_{m=1}^{N_c^{(1)}} A_{ijkl}F^{(1)}_{mk}P_{ml} \\ &+ \sum_{k=1}^{N_0}\sum_{l=N_0+1}^{N_0+K}\sum_{n=1}^{N_c^{(2)}} A_{ijkl}P_{nl}F^{(2)}_{nl}\,,\end{aligned} \tag{4.36}$$

$$\forall l = N_0+1,\ldots,N \quad \forall n = 1,\ldots,N_c^{(1)}:$$
$$\xi_{nl}^{(1)} = \sum_{m=1}^{N_c^{(1)}} \sum_{k=N_0+1}^{N} B_{mnkl}^{(1)} F_{mk}^{(1)} + \sum_{m=1}^{N_c^{(1)}} \sum_{k=N_0+1-K}^{N_0} B_{mnkl}^{(1)} \sum_{i,j=1}^{N_0} P_{ni} S_{ij} \psi_{kj}\,, \tag{4.37}$$

$$\forall k = N_0+1,\ldots,N \quad \forall m = 1,\ldots,N_c^{(2)}:$$
$$\xi_{mk}^{(2)} = \sum_{n=1}^{N_c^{(2)}} \sum_{l=N_0+1}^{N} B_{mnkl}^{(2)} F_{nl}^{(2)} + \sum_{n=1}^{N_c^{(2)}} \sum_{l=N_0+1-K}^{N_0} B_{mnkl}^{(2)} \sum_{i,j=1}^{N_0} P_{mj} S_{ij} \psi_{il}\,. \tag{4.38}$$

These three sub-systems relate the combined solution vector $(\psi_{kl}, F_{mk}^{(1)}, F_{nl}^{(2)})$, see figure 4.14, to the combined right-hand side $(\chi_{ij}, \xi_{nl}^{(1)}, \xi_{mk}^{(2)})$.

If no outer problem is to be solved ($N_0 = N$, $N_1 = 0$), the equations (4.36)–(4.38) reduce to (4.29) and the symmetrical matrix of the linear equations has the structure illustrated in the figure 4.15. The rank of the matrix grows as $O(N^2)$.

When the problem is split into the inner and outer part, the combined matrix has a slightly more complicated structure shown in the figure 4.16, but the rank of the combined matrix for the fixed inner basis (fixed N_0) scales with $O(N_1) \sim O(N)$ as $N_1 \to +\infty$, which is already a great improvement over the original $O(N^2)$. Even more, for a general M-electron problem, the number of inner solution elements grows as $O(N_0^M)$, but with the new approach still just a few *one-dimensional* (hence $O(N^1)$) channels will dominate as $N \to +\infty$.

As noted, the resulting combined matrix does not possess the regular nested structure of the original inner-only problem, so that it is not easily possible to use the effective Kronecker product approximation preconditioner. However, the matrix is relatively small and it is computationally feasible to use the sparse incomplete LU factorization.

The method of channel reduction can be, to some degree, used also for energies above the ionization threshold. This is possible, because a numerical grid (including the B-spline representation) can support only a finite number of bound and continuous eigenstates of the one-electron hamiltonian. Number of these states is equal to the number of basis elements. For energies close above the ionization threshold there is mostly less than a hundred open channels, which can be used in expansion (4.21).

Finally, it is possible to include also some forbidden channels in the expansion (4.21). The benefit of this inclusion is that the inner radius R_a does not need to reach so far. This is very advantageous close below a threshold, where the channel that opens above the threshold already manifests itself very clearly and only slowly decays. Inclusion of such a channel in the asymptotic expansion will speed up the convergence in R_a.

To illustrate the benefits of the suggested approach we did several simple calculation of the electron-hydrogen scattering at energies right above chosen excitation thresholds. All calculations are for transitions between the s-states and for total quantum numbers $L = S = \Pi = 0$. The B-spline knot spacing is 1 a_0 in the real part and gradually increasing in the complex part, which is 500 a_0 long. The scattering equations have been

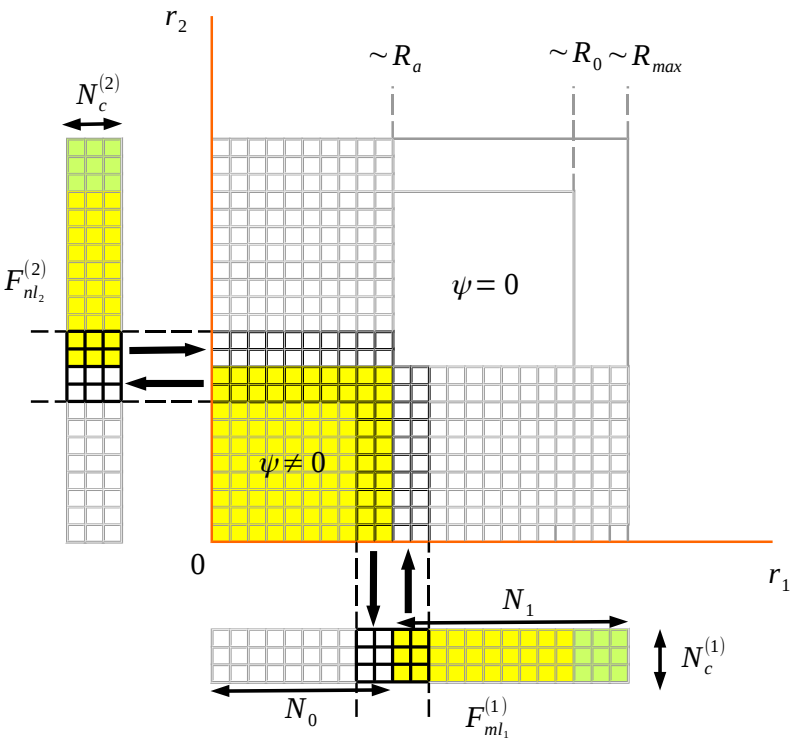

Figure 4.14: Relation of the solution parts ψ, $F^{(1)}$ and $F^{(2)}$. Every square corresponds to a B-spline projection of the functions. Only the coloured parts are solved for; yellow elements correspond to real radial B-splines, green to complex B-splines. Elements outside of the inner (outer) B-spline basis are combined from the outer (inner) solutions along the arrows.

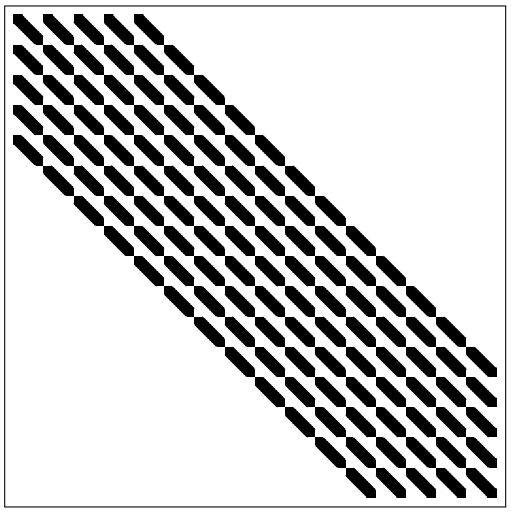

Figure 4.15: Structure of the original B-spline matrix A of the equation (4.3) or (4.29) (one angular block). The matrix corresponds to the two-dimensional nature of the problem—it has a regular structure of a tensor product of one-dimensional banded matrices.

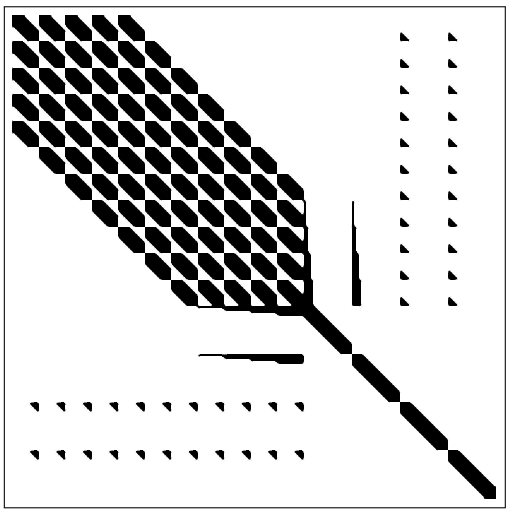

Figure 4.16: Structure of the combined set of equations (4.36), (4.37) and (4.38). The inner problem (top left) keeps the two-dimensional tensor-product nature, whereas the outer problems for the various channels (right bottom) are one-dimensional. The inner and outer problems are coupled (left bottom and right top). Generally the one-dimensional diagonal blocks can be also coupled to each other, but always only within a set corresponding to $F_{n\ell}(r_1)$ or $F_{n\ell}(r_2)$, whenever dipole or higher coupling is possible, see (4.22) and (4.25). This figure, however, corresponds to the matrix A^0_{0000} dealing with $L = \ell_1 = \ell_2 = 0$ solution blocks; these solutions asymptotically converge to a sum of s-states which are not coupled by any multipole.

solved both by the original method presented in [**36**] (top rows of the tables) and by the new method with dividing radius R_a (rest of the tables' rows). The results and the required computation times (for a 4-core Intel i7-4790K processor) are summarized in the tables 4.2 and 4.3. The dramatical reduction of calculation times is striking. With the original approach (i.e. without the channel reduction), it would be virtually unthinkable to reach radial convergence in these cases, particularly in the second one.

4.3.6 Domain decomposition

For energies high above the ionization threshold it is not possible to substantially reduce the number of asymptotic channels, as suggested in the previous section. The solution must be sought in its full form throughout the computational domain. Due to the radially decreasing influence of the inter-particle potentials the coupling between the angular components $\psi_{\mathrm{sc},\ell_1\ell_2}$ of the scattering wave function is stronger in the vicinity of the origin $r_1 = r_2 = 0$ and weaker far from the origin. The coupling is accounted for by the outer iterations of the COCG linear solver. For energies right above an excitation or ionization threshold the number of iterations needed for convergence of COCG is large, because the coupling is relatively strong at such energies. However, if the two-dimensional solution on a square $(0, R_0) \times (0, R_0)$ could be separately solved on sub-squares, only the square at the origin would need the full number of COCG iterations. The rest of the solutions would converge faster, because of weaker coupling. Also, with a symmetrical sub-division of the original domain, it is possible to take advantage of the anticipated symmetry or anti-symmetry of the wave function and solve only half of the off-diagonal sub-domains.

These are the motivations for the *domain decomposition*. Apart from reducing the average number of outer COCG iterations, the domain decomposition transforms the original large linear system to a set of smaller systems, which can better fit into the computer memory and so can be solved without resorting to out-of-core calculations or

R_a [a_0]	R_0 [a_0]	σ_0 [a_0^2]	time [min]
-	100	0.1125	0.7
-	200	0.1135	1.0
-	400	0.1151	3.5
-	800	0.1147	39.5
-	1600	0.1145	337
100	200	0.1135	0.1
100	400	0.1151	0.1
100	800	0.1147	0.1
100	1600	0.1146	0.1

Table 4.2: The partial singlet cross section for H($1s$) $\rightarrow$ H($2s$) transition at projectile impact energy $E_i = 0.755$ Ry. The angular states up to $0 \leq \ell_{1,2} \leq 3$ have been included. The total energy is $E_{\text{tot}} = -0.245\,\text{Ry}$, which is 0.005 Ry above the $n = 2$ threshold, with 2 allowed asymptotic channels: $1s$ and $2s$. Using $R_a = 100\ a_0$ as the inner region's radius is enough to match the original results within 0.1 %.

R_a [a_0]	R_0 [a_0]	σ_0 [a_0^2]	time [min]
-	200	0.105	4.5
-	400	0.106	101
-	800	0.160	533
-	1600	0.208	1094
200	800	0.160	2.7
200	1600	0.208	2.7
200	6400	0.241	2.7
200	64000	0.251	3.9
200	640000	0.252	72.6

Table 4.3: The partial singlet cross section for H($2s$) $\rightarrow$ H($3s$) transition at projectile impact energy $E_i = 0.14$ Ry. The angular states up to $0 \leq \ell_{1,2} \leq 7$ have been included. The total energy is $E_{\text{tot}} = -0.11\,\text{Ry}$, which is approximately 0.001 Ry above the $n = 3$ threshold, with 3 allowed asymptotic channels: $1s$, $2s$ and $3s$. Using $R_a = 200\ a_0$ as the inner region's radius is enough to match the original results within 1 %.

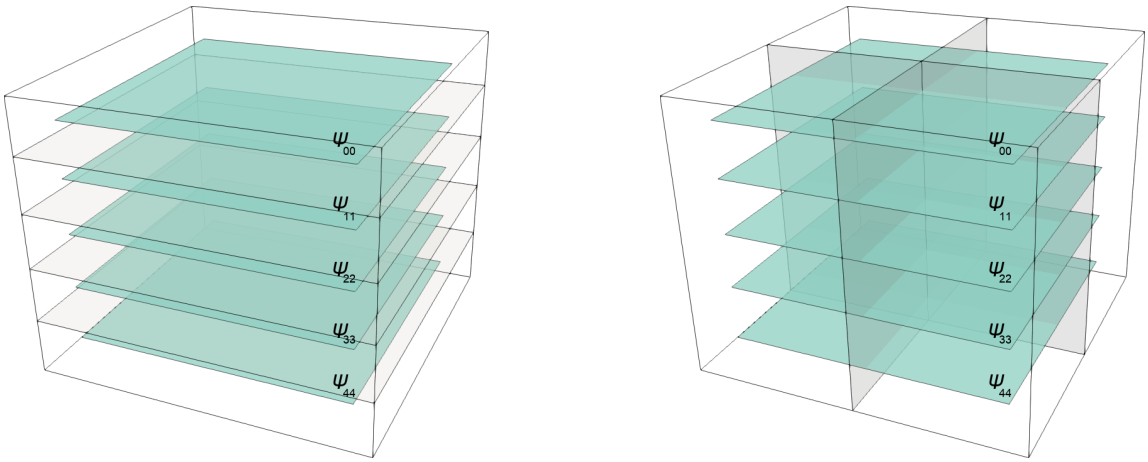

Figure 4.17: Different approaches to solution of coupled angular components of the wave function. The first figure shows the traditional approach—segregated solution—where the components are solved independently and coupling is added through the linear solver iterations. The second figure illustrates the idea of the domain decomposition—the global problem is solved separately on sub-domains. Of course, individual vertical clips (sub-domains) shown in the second figure are, again, solved by segregation.

perpetual recomputing of various intermediate results. Furthermore, the calculation of the individual sub-domain solutions can be done in parallel without involving any MPI communication apart from occasional synchronization of the solution at the interfaces. All of this has a potential of a great speed-up.

The equation (4.3) can be written as a two-dimensional Helmholtz equation in a non-homogeneous medium with a continuous source and feedback (due to the coupling to other angular components):

$$\left(\triangle + k^2(r_1, r_2)\right) \psi_{\ell_1\ell_2}(r_1, r_2) = s_{\ell_1\ell_2}(r_1, r_2)\,, \tag{4.39}$$

$$\begin{aligned}
\triangle &= \frac{\partial^2}{\partial r_1^2} + \frac{\partial^2}{\partial r_2^2}\,, \\
k^2(r_1, r_2) &= 2E_{\text{tot}} - \frac{\ell_1(\ell_1+1)}{r_1^2} - \frac{\ell_2(\ell_2+1)}{r_2^2} + \frac{2}{r_1} + \frac{2}{r_2} - \sum_\lambda 2f^L_{\ell_1\ell_2\ell_1\ell_2;L} \frac{r_<^\lambda}{r_>^{\lambda+1}}\,, \\
s_{\ell_1\ell_2}(r_1, r_2) &= 2\chi_{\ell_1\ell_2}(r_1, r_2) + \sum_{\ell_1'\ell_2' \neq \ell_1\ell_2;\lambda} 2f^\lambda_{\ell_1\ell_2\ell_1'\ell_2';L} \frac{r_<^\lambda}{r_>^{\lambda+1}} \psi_{\ell_1'\ell_2'}(r_1, r_2)\,.
\end{aligned}$$

This equation is a classical stationary wave equation well known from the electromagnetism. As in the classical elecromagnetism, each of the (uncountable) elementary source points of the source $s(r_1, r_2)$ generates waves that propagate to all directions from that point through a "medium" with varying "optical properties" given by the position-dependent wave number $k(r_1, r_2)$. When summed up, the individual field contributions give rise to the total solution of the equation (4.39). This image naturally leads to a domain decomposition approach suggested in [62], where the individual sub-problems are solved only using the sources from the sub-square, and where the sources from other panels are accounted for by inclusion of a surrogate source on the boundaries of the sub-square; the surrogate source is chosen such that it generates exactly the same incoming waves as if the other sub-squares were connected to the just considered sub-square. All other waves are out-going, so it is possible to wrap the whole sub-domain into an ECS layer of a sufficient

thickness, apart from edges where Dirichlet boundary condition is already present ($r_1 = 0$ and $r_2 = 0$).

The presentation [62] took advantage of the finite difference approach and introduced the surrogate source in the form of a term proportional to the local field value and a δ-function located at the boundary between the sub-domains. In the B-spline formulation this is difficult to realize due to the inherent smoothness of the B-spline description, which benefits elsewhere. Thus, instead of the *geometrical domain decomposition* from [62], the program hex-ecs uses an *algebraical domain decomposition*, where the basic objects are not points of the position space, but elements of the B-spline expansion in the algebraical linear space of the solution.

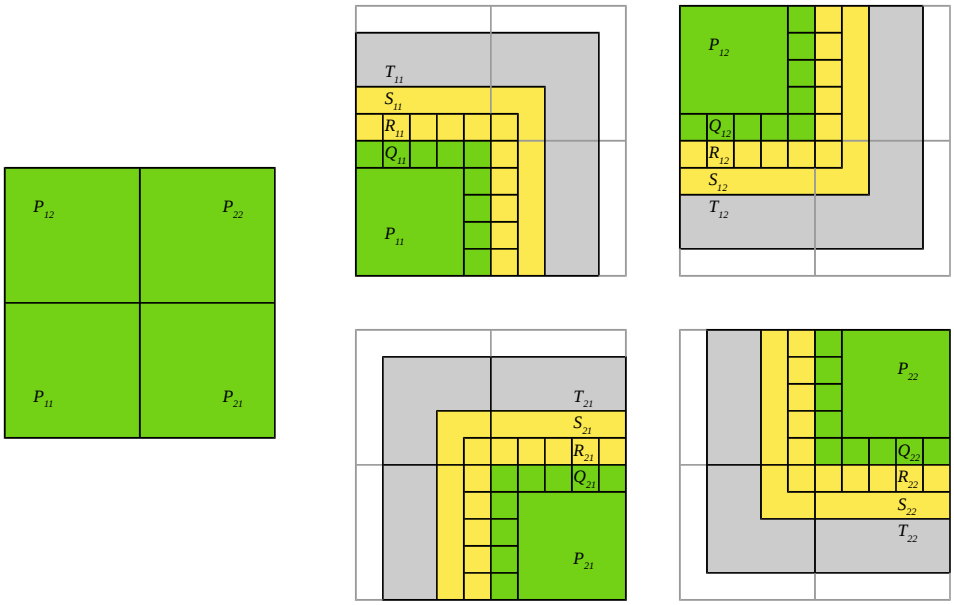

Figure 4.18: Sub-domain composition in index (algebraical) space. Left-most figure shows the full solution domain, the four remaining figures highlight the four sub-domains with all additional grid parts that are appended before the solution. The B-splines of P_n and Q_n, $Q_n \subset P_n$, are common to the full and decomposed grid, the B-splines of R_n and S_n are additional fully real B-splines with the same knots as the counterpart B-splines in the neighbour sub-domains, and T_n denotes the remaining, complex, B-splines of the ECS absorption layer.

The figure 4.18 illustrates the individual parts of the sub-domains. Every sub-domain is composed of:

- its unique B-spline elements (green regions P_n and Q_n), which are used to reconstruct the global solution,
- a few additional interface layers of B-splines that are geometrically identical to those in the neighbour panel, needed to couple the domains together (yellow regions R_n and S_n)
- and the elements corresponding to the complex B-splines in the ECS region T_n (gray), needed to damp outgoing solutions, so that we can use Dirichlet boundary condition as usual.

The solution of the scattering problem on a sub-domain is a sum of the solution generated by sources local to the sub-domain, and of the solution generated by sources from other sub-domains. The equations will be now assembled for the situation, where green parts

P_n and Q_n contain the sum of the solutions (including the in-coming solutions from neighbour panels) and yellow and gray parts R_n, S_n and T_n contain only the local (outgoing) solution. It is also assumed that the buffer layers Q_n and R_n are exactly K B-splines thick, K being the B-spline order used, and that S_n is at least K B-splines thick.

After a projection on the full-domain double B-spline basis the equation (2.11) can be written as

$$\sum_{J\in\mathcal{U}(I)} A_{IJ}x_J = b_I\,, \tag{4.40}$$

where the angular indices have been omitted for clarity. In this equation $I \equiv (i,j)$ and $J = (k,l)$ are two-component multi-indices and $J \in \mathcal{U}(I)$ denotes all index pairs (k,l) of two-dimensional B-splines $B_k(r_1)B_l(r_2)$ that have a non-empty overlap with the two-dimensional B-spline $B_i(r_1)B_j(r_2)$. The equation (4.40) reduces to several special cases when restricted to a sub-domain n:

$$\forall I \in P_n : \sum_{J\in\mathcal{U}(I)} A^{(n)}_{IJ}x^{(n)}_J = b^{(n)}_I\,, \tag{4.41}$$

$$\forall I \in Q_n : \sum_{J\in\mathcal{U}(I)\cap P_n} A^{(n)}_{IJ}x^{(n)}_J + \sum_{J\in\mathcal{U}(I)\cap R_n} A^{(n)}_{IJ}\left(x^{(n)}_J + \overline{y}^{(n)}_J\right) = b^{(n)}_I\,, \tag{4.42}$$

$$\forall I \in R_n : \sum_{J\in\mathcal{U}(I)\cap Q_n} A^{(n)}_{IJ}\left(x^{(n)}_J - \overline{y}^{(n)}_J\right) + \sum_{J\in\mathcal{U}(I)\cap(R_n\cup S_n)} A^{(n)}_{IJ}x^{(n)}_J = 0\,, \tag{4.43}$$

$$\forall I \in S_n \cup T_n : \sum_{J\in\mathcal{U}(I)} A^{(n)}_{IJ}x^{(n)}_J = 0\,. \tag{4.44}$$

For a sub-domain n, the source $b^{(n)}_I$ is only non-zero in P_n; it is assigned to the sub-domain during the decomposition of the global source. In other parts it is zero. The matrix $A^{(n)}_{IJ}$ has identical elements for both the global and local problem only for I, J in P_n and R_n; otherwise the elements are different, hence the distinction between A_{IJ} (global) and $A^{(n)}_{IJ}$ (local, differs from A_{IJ} close to complex region and inside of it).

The remaining newly introduced symbols in the above set of equations are the neighbour panel solutions $\overline{y}_J$ generated by sources in other panels than the currently solved panel n. In case of equation (4.42) it is $\overline{y}^{(n)}_J = \overline{x}^{(m)}_J - \overline{x}^{(n)}_J$, where m is the only neighbour panel for which $J \in Q_m$. The line above the symbols means that the values from the previous sweep are used. With progressing convergence the expression $x^{(n)}_J - \overline{y}^{(n)}_J$ tends to $\overline{x}^{(m)}_J$, because $x^{(n)}_J - \overline{x}^{(n)}_J$ tends to zero, resulting in desirable continuity (coupling) between panels. In case of equation (4.43) it is $\overline{y}^{(n)}_J = \sum_{m\neq n}\overline{x}^{(m)}_J$, where the sum goes over all neighbour panels of the panel n. This sums all field coming from neighbour panels, so that they can be used to isolate the field originating from the sub-domain n.

The above equations can then be rewritten as

$$\forall I \in P_n : \sum_{J\in\mathcal{U}(I)} A^{(n)}_{IJ}x_J = b_I\,, \tag{4.45}$$

$$\forall I \in Q_n : \sum_{J\in\mathcal{U}(I)} A^{(n)}_{IJ}x_J = b_I - \sum_{J\in\mathcal{U}(I)\cap R_n} A^{(n)}_{IJ}\left(\overline{x}^{(m)}_J - \overline{x}^{(n)}_J\right)\,, \tag{4.46}$$

$$\forall I \in R_n : \sum_{J\in\mathcal{U}(I)} A^{(n)}_{IJ}x_J = \sum_{J\in\mathcal{U}(I)\cap Q_n} A^{(n)}_{IJ}\sum_{m\neq n}\overline{x}^{(m)}_J\,, \tag{4.47}$$

$$\forall I \in S_n \cup T_n : \sum_{J\in\mathcal{U}(I)} A^{(n)}_{IJ}x_J = 0\,, \tag{4.48}$$

which is exactly the original proposal: we are solving standard local field problem (where mostly $A^{(n)}_{IJ} = A_{IJ}$) with a modified source b_I. All modifications to the source arise only in regions Q_n and R_n.

The penalty for the benefits of the domain decomposition approach is an addition of another level of iterations to propagate information from each sub-domain into all other sub-domains. Nevertheless, during these additional iterations convergence is always reached in a finite number of sweeps over all sub-domains. Due to the linearity of the equation (4.40) the resulting "field" in every sub-domain is a simple sum of fields generated by sources in all sub-domains. In other words, the source in every sub-domain contributes to the field in every sub-domain. So it is necessary to do so many sweeps that the influence of every sub-domain propagates into every other subdomain. The zero Dirichlet boundary condition in the origin $r_1 = 0$ or $r_2 = 0$ acts as a fixed-end reflecting boundary, so the fields bounce off the two edges and propagate back into the space, until they are damped in the complex grid area. If n is the number of sub-domains along an axis, then the information needs to (approximately) traverse less than or equal to $2n$ sub-domains. This is true for all sub-domains, so one has to solve all sub-domains approximately $2n$-times, totalling in $2n^3$ separate sub-domain solutions, to obtain the final global solution, assuming equal sub-division in both axes.

The symmetrical and uniform n-by-n decomposition shown in the figure 4.17 is not the only possibility, though it is the most efficient one when the magnitude of the wave function far from the axes is small and so most of the field propagates more or less symmetrically along the axes. In this case some of the central sub-domains can be ignored to save computational time. A different possibility is to use a 1-by-n, i.e. linear, decomposition, which performs well in situations where the ionization contribution is important; see figure 4.19. Also, it is advantageous to split the solution domain into even parts in terms of the number of B-splines. These are more densely clustered close to the axes, which is the reason for the uneven appearence of the sub-domains in the figure 4.19.

The domain decomposition can be combined with the channel reduction discussed earlier without any restriction. The channel-reduced grid part is then either (and preferably) a separate sub-domain of its own, or part of another, standard, sub-domain. This is yet to be implemented in the solver program hex-ecs.

To conclude this section, it is worthwhile to point out that in the above presentation the linearity of wave-functions and of probability fluxes with respect to their sources has been used interchangeably, even though on the first sight the relation for the flux $\mathbf{j}$

$$\mathbf{j} = \frac{1}{2\mathrm{i}}(\psi^* \nabla\psi - \psi \nabla\psi^*) \tag{4.49}$$

is of the second order in ψ. While it is obvious that a linear combination of sources on the right-hand side of the equation (4.39) leads to the same linear combination of solutions, it is not so obvious for the combination of fluxes. However, it holds as well due to cancellation of cross-terms in the formula for a combined probabilty flux:

$$\begin{aligned}\mathbf{j} &= \frac{1}{2\mathrm{i}}\left((\psi_1+\psi_2)^*\nabla(\psi_1+\psi_2) - (\psi_1+\psi_2)\nabla(\psi_1+\psi_2)^*\right) = \\ &= \frac{1}{2\mathrm{i}}\left(\psi_1^*\nabla\psi_1 + \psi_2^*\nabla\psi_2 - \psi_1\nabla\psi_1^* - \psi_2\nabla\psi_2^*\right) = \mathbf{j}_1 + \mathbf{j}_2\,.\end{aligned}$$

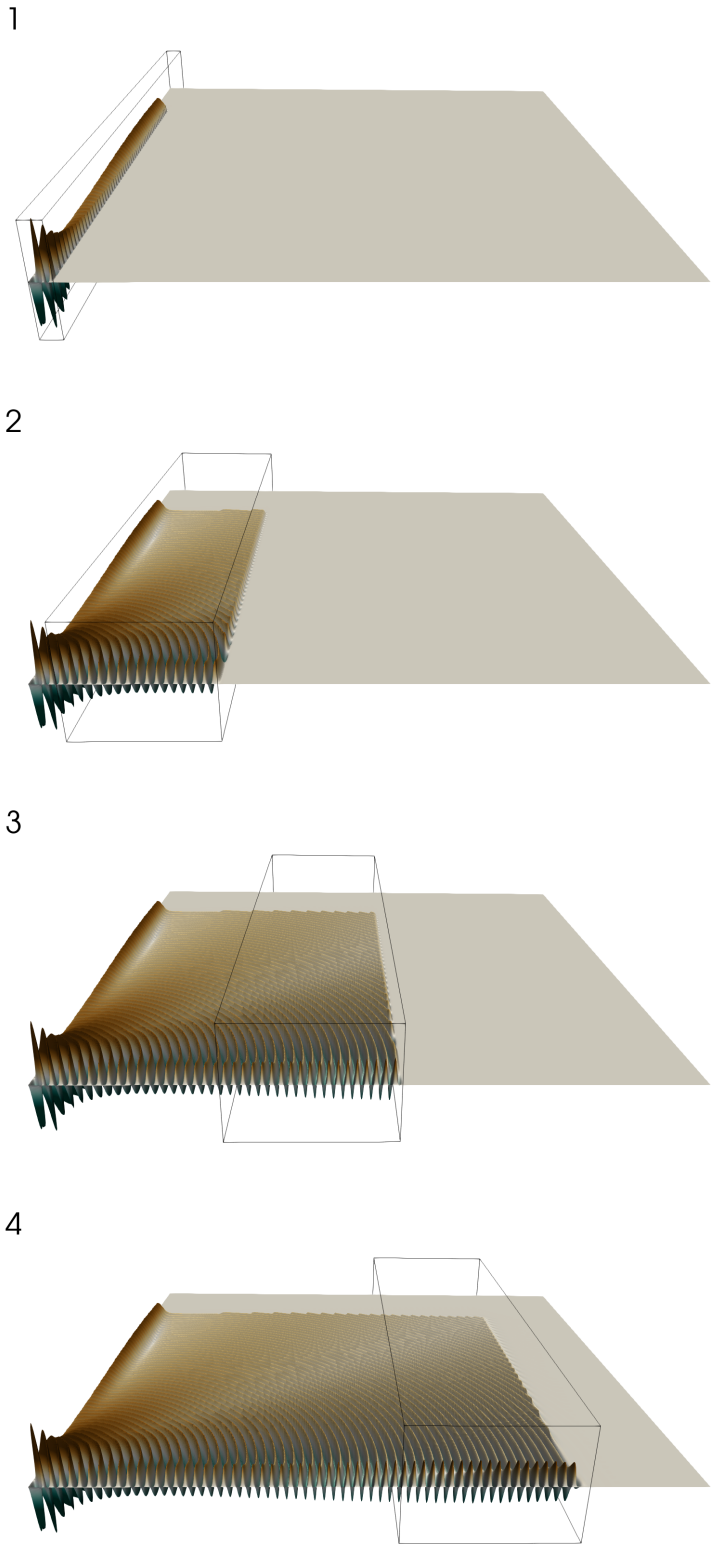

Figure 4.19: Collected solutions from sub-domains for 1-by-4 domain decomposition in the first sweep. The remaning sweeps only slightly correct the wave function without a deep visual impact.

Chapter 5

Hex-db: Database interface

The result of the computational codes are either the T-matrices, or the cross sections for various outcomes of the electron-hydrogen collisions. These can be used on their own, or assembled in a common database file, which can be then post-processed for derived scattering quantities. The interface program hex-db does a similar service for the Hex package as the program MJK [63] for the R-matrix package RMATRX1 [64]. Description of the program hex-db was published in [**65**].

5.1 Scattering T-matrices

The most basic scattering quantity used in Hex is the T-matrix. It is produced, stored and re-used in the form of the partial wave expansion,

$$T = \sum_{\ell=0}^{\infty} T_\ell Y_\ell^{m_i - m_f} \,. \tag{5.1}$$

This expansion can take very large amount of terms to converge. Interestingly, for some cases like scattering on charged target or for transitions between degenerate levels the sum does not converge at all, even though the terms are perfectly finite. When the sum exists, it is necessary to truncate it at some $\ell_{\max}$. The rest of the sum is either negligible, or can be extrapolated.

For elastic scattering the only important asymptotic contribution is from the polarization potential $V_{\rm pol} = -\alpha/2r^4$. In the first Born approximation the T-matrix is proportional to

$$T_\ell^{\rm el} \sim \int \hat{j}_\ell(kr) V_{\rm pol}(r) \hat{j}_\ell(kr) {\rm d}r \,.$$

This can be integrated using the formula ([66], §6.576)

$$\int_0^\infty x^{-\lambda} J_\nu(ax) J_\nu(bx) {\rm d}x = \frac{a^\nu b^\nu \Gamma\left(\nu + \frac{1-\lambda}{2}\right)}{2^\lambda (a+b)^{2\nu-\lambda+1} \Gamma(\nu+1) \Gamma\left(\frac{1+\lambda}{2}\right)} \, {}_2F_1\left(\begin{matrix} \nu + \frac{1-\lambda}{2}, \nu + \frac{1}{2} \\ 2\nu + 1 \end{matrix} \middle| \, \frac{4ab}{(a+b)^2} \right)$$

and the Gauss identity ([27], §15.4)

$${}_2F_1\left(\begin{matrix} a, b \\ c \end{matrix} \middle| \, 1 \right) = \frac{\Gamma(c)\Gamma(c-a-b)}{\Gamma(c-a)\Gamma(c-b)}$$

to yield, see also [67], §45.2.4,

$$T_\ell^{\rm el} \sim \frac{\alpha k^2}{(2\ell-1)(2\ell+1)(2\ell+3)} \,, \tag{5.2}$$

or simply $T_\ell \sim \ell^{-3}$.

For inelastic transitions the ultimate asymptotic behaviour is exponential due to exponentially decreasing overlap between the initial and final orbital;

$$T_\ell^{\text{inel}} \sim cq^\ell \,. \tag{5.3}$$

The formulas (5.2) and (5.3) are used to add as many terms to (5.1) as needed to make it converge within sufficient tolerance.

5.2 Derived scattering quantities

The definitions of all scattering quantities provided by hex-db interface are summarized in this section, together with the keywords that should be used when querying for these particular quantities. These are given in typewriter font.

The scattering amplitude, `scatamp`, for discrete transitions

$$f_{fi}^S(\hat{\mathbf{k}}_f) = -\frac{1}{2\pi}\sum_\ell T_\ell^{LSm_i} Y_\ell^{m_i-m_f}(\hat{\mathbf{k}}_f)\,. \tag{5.4}$$

and for ionization amplitude $F^S(\mathbf{k}_1,\mathbf{k}_2)$, `ionamp`, see (4.16). Alternatively, there is also `scatamp-dir` which provides the scattering amplitude calculated for arbitrary impact direction, see (2.26). In the computer code the d-matrix needed for directional scattering amplitude is evaluated using the appropriate routine from GSL [68]. The differential cross section, `dcs`,

$$\frac{\mathrm{d}\sigma_{fi}^S}{\mathrm{d}\Omega}(\hat{\mathbf{k}}_f) = \frac{k_f}{k_i}\frac{2S+1}{4}\left|f_{fi}^S(\hat{\mathbf{k}}_f)\right|^2 \,.$$

The spin asymetry, `asy`, is a combination of the discrete differential cross sections,

$$\alpha_{fi} = \frac{\mathrm{d}\sigma_{fi}^0 + \frac{1}{3}\mathrm{d}\sigma_{fi}^1}{\mathrm{d}\sigma_{fi}^0 + \mathrm{d}\sigma_{fi}^1}\,.$$

The triple differential cross section, `tdcs`, is a five-dimensional distribution of scattering probability in the case of ionization,

$$\frac{\mathrm{d}\sigma_{fi}}{\mathrm{d}\hat{\mathbf{k}}_1\mathrm{d}\hat{\mathbf{k}}_2\mathrm{d}E_2}(\mathbf{k}_1,\mathbf{k}_2) = \sum_S \frac{2S+1}{4}\frac{k_1k_2}{k_i}|F^S(\mathbf{k}_1,\mathbf{k}_2)|^2\,.$$

The (partial) integral cross section, `ics`, for discrete transitions

$$\sigma_{fi,\ell}^S = \frac{k_f}{k_i}\frac{2S+1}{16\pi^2}\sum_{LL'} T_\ell^{LSm_i} T_\ell^{L'Sm_i*}\,,$$

and for ionization

$$\sigma_{fi,L}^S = \sum_{\ell_1,\ell_2}\int_0^{E/2}\frac{k_1k_2}{k_i}|f_{\ell_1\ell_2}^{LS}(k_1,k_2)|^2\mathrm{d}E_2\,.$$

The integrand in this integral is very oscillatory and is integrated by means of the Clenshaw-Curtis quadrature, see Appendix A, which uses harmonic functions to approximate the integrand and is well suited for oscillatory functions.

The collision strength, `colls`, is a dimensionless quantity proportional to the cross section ([67], §47.1.1). The cross section is multiplied by the impact energy. The advantage

of the collision strength is its symmetry ($\Omega_{fi} = \Omega_{if}$) stemming from the theorem of the detailed balance, and also that it filters out the overall energy dependence, so that for example the threshold value does not rise sharply. The formula is

$$\Omega^S_{fi} = (2l_i + 1)k_i^2 \sigma^S_{fi} \,.$$

The (total) cross section, `ccs`,

$$\sigma^S_{fi} = \sum_\ell \sigma^S_{fi,\ell} \,.$$

The spin flip cross section, `spflip`, comes from (2.23),

$$\sigma^{\mathrm{spin-flip}}_{fi} = \frac{k_f}{k_i} \frac{1}{16\pi^2} \sum_{\ell LL'} \left(T^{L0m_i}_\ell T^{L'0m_i *}_\ell + T^{L1m_i}_\ell T^{L'1m_i *}_\ell - 2\mathrm{Re}\, T^{L0m_i}_\ell T^{L'1m_1 *}_\ell \right) .$$

The (grand) total cross section, `tcs`, uses for its evaluation the optical theorem,

$$\sigma^S_i = \sum_f \sigma^S_{fi} = \frac{2S+1}{4} \frac{4\pi}{k_i} \mathrm{Im}\, f_{ii}(\hat{\mathbf{k}}_i) \,. \tag{5.5}$$

The above equation follows from the unitarity of the S-matrix and its consequence that $\sum_{f\ell'} T_{if,\ell\ell'} T^*_{fi,\ell'\ell} \sim \mathrm{Im}\, T_{ii,\ell\ell}$ in the meaning refined in the beginning of the next chapter.

In electron-photon coincidence experiments several special variables are used. For dipole-allowed transitions ($|l_i - l_f| = 1$, e.g. $\mathrm{H}(1s) \to \mathrm{H}(2p)$) they are defined using the three basic statistical quantities ([67], §46)

$$\lambda = \langle |f_0^2| \rangle \left(\frac{\mathrm{d}\sigma}{\mathrm{d}\Omega} \right)^{-1} , \quad R = \mathrm{Re}\, \langle f_1 f_0^* \rangle \left(\frac{\mathrm{d}\sigma}{\mathrm{d}\Omega} \right)^{-1} , \quad I = \mathrm{Im}\, \langle f_1 f_0^* \rangle \left(\frac{\mathrm{d}\sigma}{\mathrm{d}\Omega} \right)^{-1} . \tag{5.6}$$

The angle brackets symbolize averaging over the spin states (i.e. 1/4 of the singlet value and 3/4 of the triplet value). The indices 1 or 0 indicate whether the transition changed the atomic magnetic quantum number or not. The *reduced Stokes parameters* are then the components of the vector

$$\mathbf{P} = (2\lambda - 1; 2\sqrt{2}R; -2\sqrt{2}I) \,,$$

the *linear polarization* is the size of the xy-projection of $\mathbf{P}$,

$$P_l = \sqrt{P_x^2 + P_y^2} \,,$$

the *charge cloud alignment* is the angle parameter

$$\gamma = \frac{1}{2} \arg(P_x + \mathrm{i}P_y) \,,$$

and the *excitation coherence* is the magnitude of the vector $\mathbf{P}$,

$$P^+ = |\mathbf{P}| \,.$$

All these numbers will be written out if the switch `--stokes` is used.

5.3 Interpolation

A very important part of the post-processing is the interpolation of the results. The reasons for a need of a good interpolation technique are at least two:

- The database may not contain the numerical data for a particular impact energy, but it does contain data for some close energies, which can be used to estimate of the missing points.
- To avoid unnecessary consumption of the computational time, some partial waves may be calculated with fewer energy samples than other partial waves for the same transition. For example low partial waves need to be more finely sampled to capture the shape of the resonances, whereas the higher partial waves are typically very smooth and monotonous. But to construct the final cross section energy dependence, these partial wave contributions need to be added together, which is not well defined if the sampling is not identical.

The method of choice in hex-db has been the interpolation using the *Akima splines* [69]. These polynomial functions are essentially plain cubic splines with relaxed condition on the continuity of the second derivative. As such they are more flexible and support smooth interpolation of data with out-of-trend points. This is very useful in scattering data, where the energy dependencies have a simple overall behaviour with sudden resonant structures. The construction of the Akima spline iterpolation is done using the routines from the GSL [68].

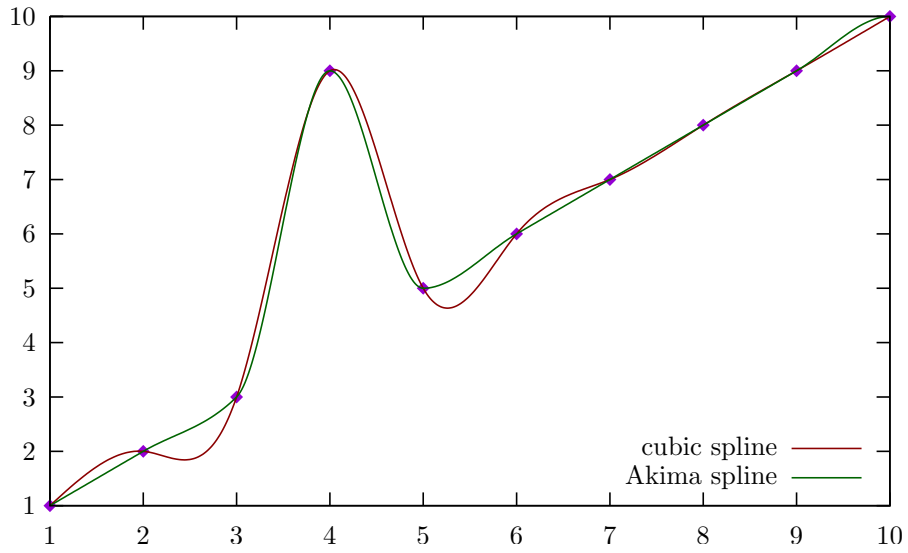

Figure 5.1: Comparison of interpolation using the Akima splines and the common cubic splines. Whereas the cubic spline interpolation oscillates in the vicinity of an out-of-trend point, the Akima spline adapts very well to the expected behaviour of the curve.

But it is not enough to know how to interpolate, also the decision of what to interpolate is important. Even the powerful Akima splines are just polynomial functions, which by themselves would prove very useless to follow the cross section curves, which typically decrease as an inverse of the impact energy. For this reason it is not the cross sections that are interpolated, but the collision strengths $\Omega_{ij} = E_i\sigma_{ji}$. Similarly, the T-matrices need to be interpolated only through the product $\tau_{ji} = k_i T_{ji}$.

Chapter 6

Results

This chapter presents the calculated data and also results from several basic tests, which include comparison with other data and verification of the theoretical requirements on unitarity and conservation. The figures in this part contain mostly the collision strengths. The calculated T-matrices and other derived quantities are available via the web portal to the database mentioned in the chapter 3. The calculated datasets were published in [**78**].

One of the theoretical tests is the conservation of flux, also called the *unitarity* of the S-matrix. If we use the canonical definition of the T-matrix, we have ([67], §47.1.1)

$$f_{fi}(\hat{\mathbf{k}}_f) = \mathrm{i}\sqrt{\frac{\pi}{k_i k_f}} \sum_{LS\ell'\ell} \mathrm{i}^{\ell-\ell'} \sqrt{2\ell+1} C^{Lm_i}_{l_i m_i \ell 0} C^{Lm_i}_{l_f m_f \ell m_i - m_f} T^{LS}_{fi,\ell'\ell} Y_{\ell'}^{m_i - m_f}(\hat{\mathbf{k}}_f)\,.$$

By substituting this expression to (5.4) we obtain the relation between the canonical multi-channel T-matrix $T^{LS}_{fi,\ell'\ell}$ and the T-matrix $T^{LS}_{fi,\ell}$ used in Hex:

$$T^{LS}_{fi,\ell'\ell} = \sum_{m_i m_f} \mathrm{i}^{\ell'-\ell} C^{Lm_i}_{l_i m_i \ell 0} C^{Lm_i}_{l_f m_f \ell' m_i - m_f} \frac{\mathrm{i}}{2\pi} \sqrt{\frac{k_i k_f}{\pi}} \frac{1}{\sqrt{2\ell+1}} T^{LS}_{fi,\ell}\,. \tag{6.1}$$

After summing over L this number should satisfy the relation (2.18) in a matrix sense, when the channel labels (i,ℓ) and (f,ℓ') are used as matrix indices.

The figures in this chapter show among other things the partial wave convergence. This is represented by several curves with increasing saturation. The lightest curve represents the lowest partial wave, the next is sum of the first two partial waves, etc., and the darkest curve represents the converged sum of all partial waves.

6.1 Scattering lengths

The datasets are not bounded from above due to arbitrary possible impact energy, but for every process there exists a specific energy when the channel opens. In the textbook scattering on finite-range potentials, the inelastic cross sections at the excitation threshold are equal to zero. However, due to the degeneracy of the hydrogen levels, the atom is strongly polarized by the projectile and the cross sections (or T-matrices) at the thresholds are generally non-zero [70]. A similar situation occurs in elastic scattering on excited states, where the cross section diverges. Only for elastic scattering on the ground state, in the only single-channel situation, there is a finite non-zero limit ([67], §45.2.4)

$$\lim_{k\to 0+} \sigma^S_{ii}(k) = (2S+1)\pi a_s^2 + O(k^2)\,, \tag{6.2}$$

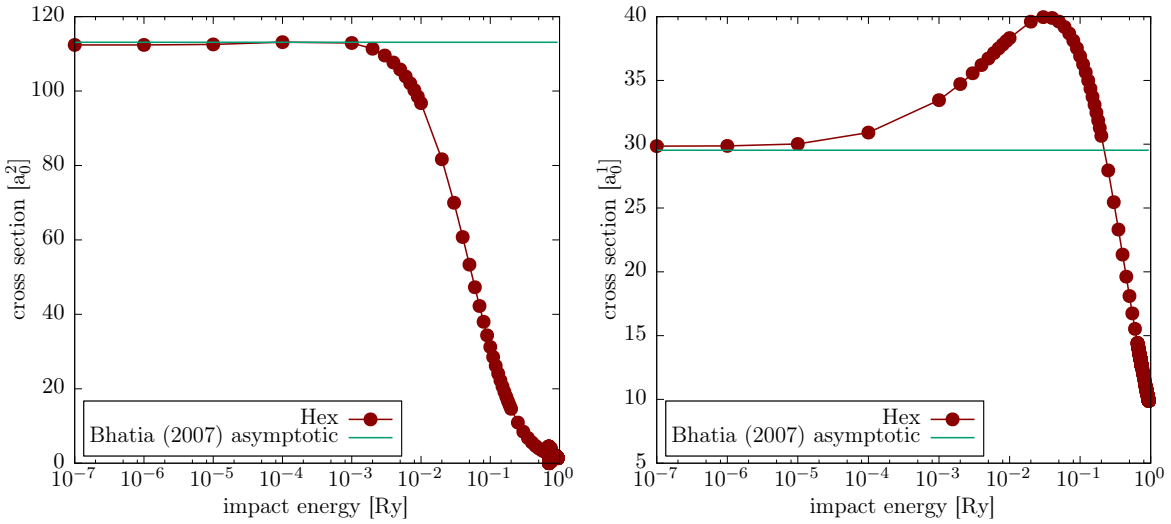

Figure 6.1: Asymptotic values of the scattering cross sections for extremely low-energy scattering on the ground state at symmetry $L = \Pi = 0$; they converge to (6.2). The left panel contains results for the singlet state ($S = 0$), the right panel for the triplet state ($S = 1$).

which defines an effective size parameter a_s called the *scattering length* of the target state. This value determined the elastic cross section for transition $1s - 1s$ at zero energy. The article [71] contains the values 6.00 a_0 and 1.77 a_0 for singlet and triplet ground state scattering, respectively, which agrees with the present results 6.00 a_0 and 1.78 a_0 within one percent.

To obtain the values the scattering has been calculated for several energies exponentially approaching the threshold from above and the evaluated scattering lengths have been extrapolated using a linear fit. Results of the calculations are shown in the figure 6.1.

6.2 S-wave model

The S-wave model ($L = \ell_1 = \ell_2 = 0$, also known as the Temkin-Poet model) is very easy to simulate, because the system contains just one block and thus no long-range angular coupling. It has been used to verify the present ECS implementation. The figure 6.2 compares the cross sections obtained by hex-ecs and other programs.

The Temkin-Poet model is a useful tool for exploration of some basic properties of the electron-hydrogen scattering problem. As a sub-topic of this thesis the asymptotic behaviour of the cross section for highly excited states was analyzed. While the inelastic cross sections exponentially decrease in the limit $n_f \to +\infty$ due to the diminishing overlap of the initial and final orbital, the elastic cross sections behave differently. The elastic cross sections for the first approximately 100 atomic states have been investigated within the Temkin-Poet model, see the figure 6.3. Results from elastic scattering calculations came as a surprise; they so far seem to have an oscillatory character, even though a monotonous behaviour might be expected. It is not clear whether the oscillations would continue for even higher states. Also, this is a feature of the Temkin-Poet model. Its significance for the physical, partial-wave-converged results is not obvious.

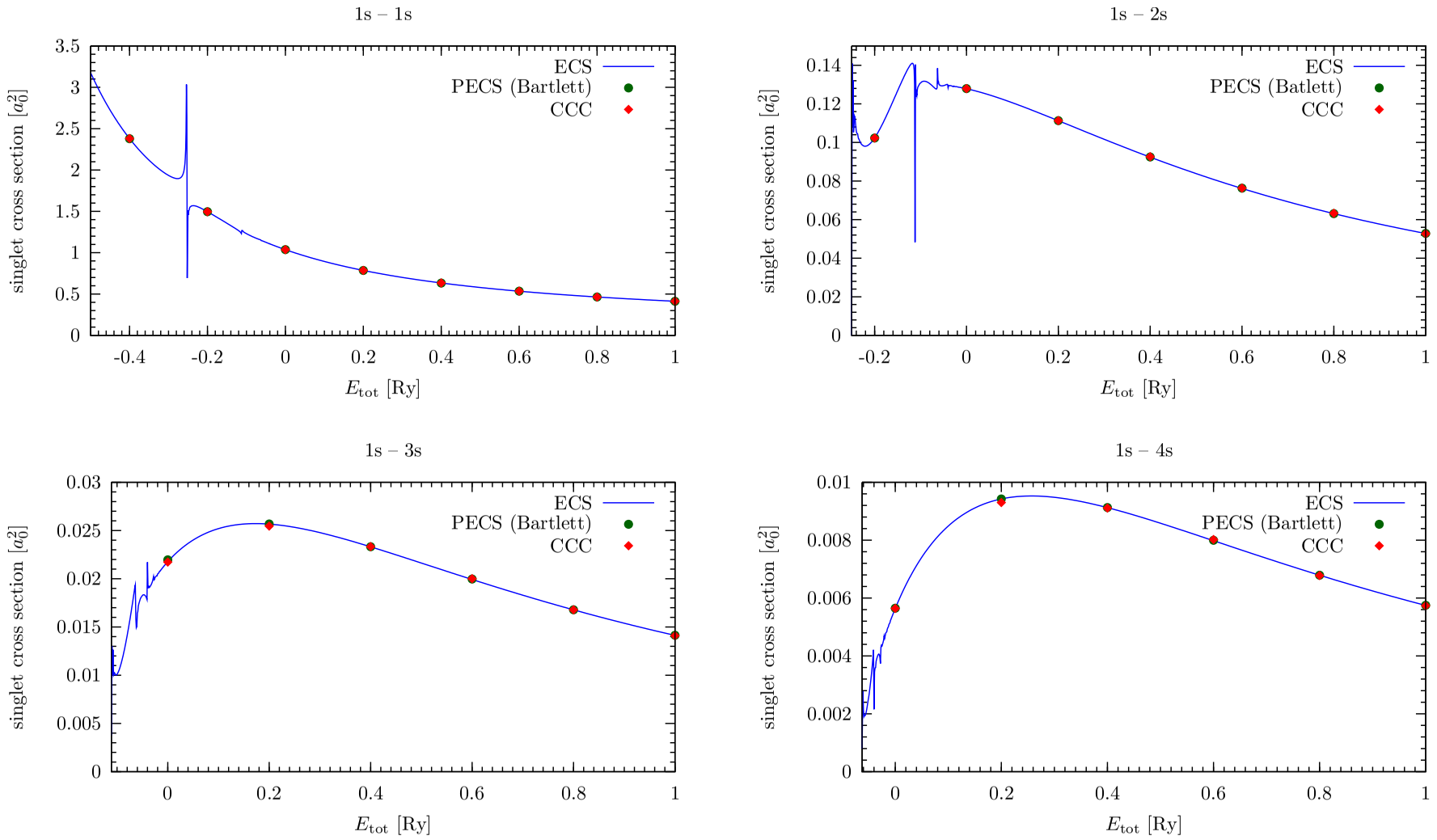

Figure 6.2: The singlet cross sections for excitations from the 1s to higher states within the Temkin-Poet model. The data are from PECS calculation by Bartlett [40] (green dots) and from a CCC code by Bray [72] (red diamonds).

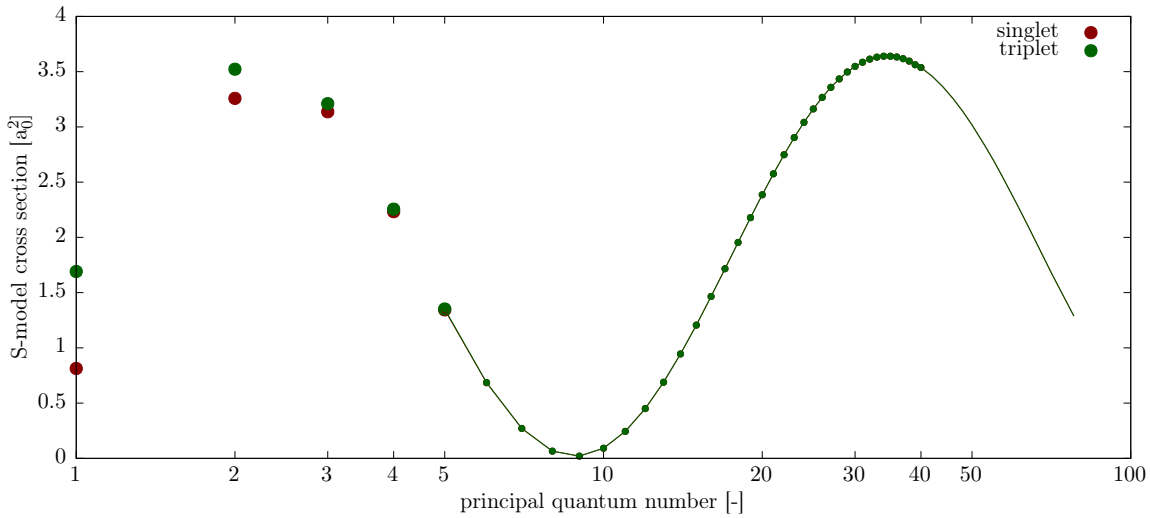

Figure 6.3: Elastic cross sections on the hydrogen s-states at total energy $E_{\mathrm{tot}} = 3$ Ry within the Temkin-Poet model, without spin weights. The difference between the results for singlet and triplet configurations are noticeable only for $n \leq 5$, for higher states the scattering becomes spin-independent.

6.3 Resonances

The lowest possible total energy of the (e^-, e^-, p^+) system is the only bound state of H^- with energy -14.35 eV. All other would-be bound states of H^- are autoionizing double excitations lying above the threshold of the $H(1s) + e^-$ scattering channel, which manifest as Feshbach resonances and are clearly observable.

The resonances are mostly labeled by approximate two-electron configuration, e.g. $H^-(2s2p)$. This scheme approximates the structure as a combination of an excited hydrogen atom $H(nl)$, $n \geq 2$, called the *parent* state [73], and a weakly attached electron in an excited state $e^-(n'l')$, $n' \geq n$, $l' \geq l$. In the approximation of independent electrons it is exactly the binding energy of the attached electron that defines the position of the resonance with respect to the excitation threshold of the hydrogenic level n. This notation is used in the figures, together with the total symmetry of the resonant state, i.e. identification of the partial wave where the resonance appears. For example $^1S^e$ is the singlet even-parity s-wave.

Resonances are marked only in the ground state elastic scattering datasets, figures 6.4, 6.6 and 6.13, but they are present in all transitions. Their positions were taken from [74], [75], [76] and [77].

6.4 Results below the threshold $n = 2$

The easiest calculation is for total energies ranging from the lowest limit, $E_{\mathrm{tot}} = -1$ Ry, to the first excitation threshold, $E_{\mathrm{tot}} = -0.25$ Ry. No other state than the gound state can exist in this domain, so the calculation is single-channel, very fast and only one problem must be solved for every energy. The collected elastic data are presented in the figure 6.4.

In the single-channel elastic scattering the relation (6.1) between the Hex's T-matrix and the canonical T-matrix reduces to

$$T^{\ell S}_{ii,\ell\ell} = \frac{\mathrm{i}}{2\pi} \frac{k_i T^{\ell S}_{ii,\ell}}{\sqrt{\pi(2\ell+1)}} \,.$$

A plot of the expression $|T^{\ell S}_{ii,\ell\ell} + 1|^2 - 1$, which ideally tends to zero due to unitarity of the S-matrix, is given in the figure 6.5 for partial waves $0 \leq \ell \leq 2$. The unitarity error is always less than one part in a thousand, well within the desired accuracy of a few percent.

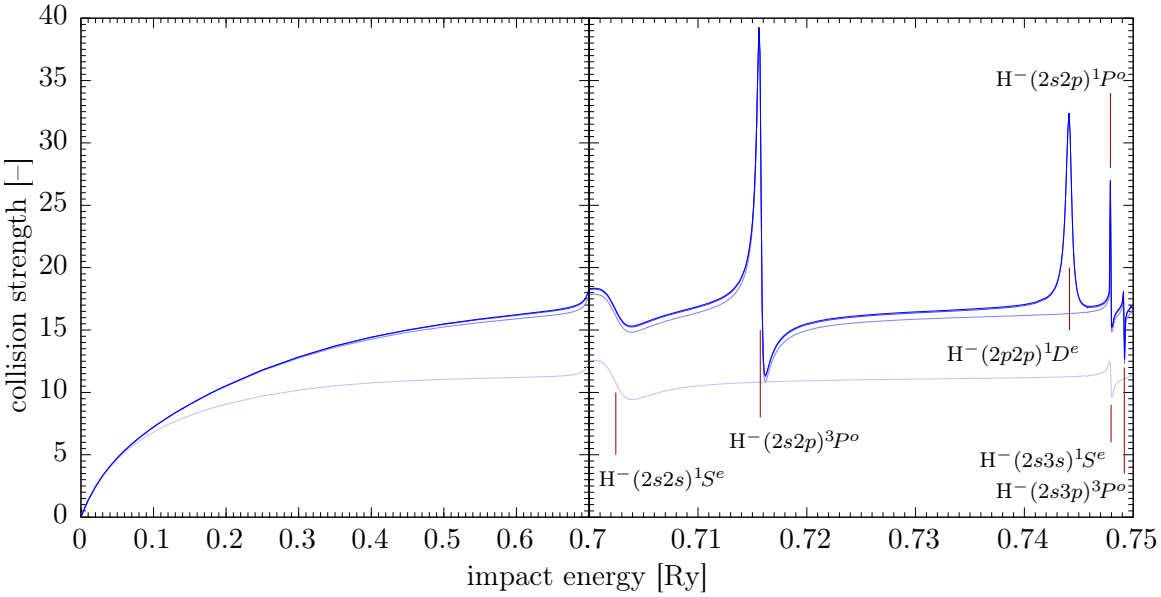

Figure 6.4: The collision strengths for the lowest possible total energies below the first excitation threshold. Only one channel H($1s$) + e^- is open. The area around the first resonance is stretched to make the resonances apparent. Only the partial waves with $\ell = L = 0$, 1, 2 are visually distinguishable. Figure displays 4 partial waves in total.

6.5 Results between $n = 2$ and $n = 3$ thresholds

In the energy region between $E_{\mathrm{tot}} = -0.250$ Ry and $E_{\mathrm{tot}} = -0.\overline{111}$ Ry the hydrogen atom can exist in the ground state or in one of the excited states $2s$ or $2pm$, allowing for collision-induced transitions H($1s$) $\rightarrow$ H($1s$), H($1s$) $\rightarrow$ H($2s$), H($1s$) $\rightarrow$ H($2pm$), H($2s$) $\rightarrow$ H($2s$), H($2pm$) $\rightarrow$ H($2pm'$) and their reverses. Due to the non-relativistic degeneracy of the states with $n = 2$ the summed cross section for transition H($2s$) $\rightarrow$ H($2pm$) diverges; the same holds for the reverse transition. All other transitions are finite and their partial wave convergence is shown in the figures 6.6–6.8. It is noteworthy to point out the extreme number of partial waves needed for convergence of elastic scattering on the excited states, see figures 6.9 and 6.10. This is a problem of all excited states. The figures 6.33, 6.34 compare the calculated cross sections to other available results.

In this energy region it is also possible for the first time to check the reversibility, the theorem of detailed balance. The theorem states exactly that $\Omega_{fi} = \Omega_{if}$. For elastic transitions this is a trivial equivalence. For inelastic scattering there is some new information. The collision strengths are compared in the figure 6.11, demonstrating very accurate consistency of the two datasets.

Finally, it is possible to check that the cross sections sum to the total cross section that is expected from the optical theorem (5.5). The comparison of the total cross section for scattering on the ground state is in the figure 6.12.

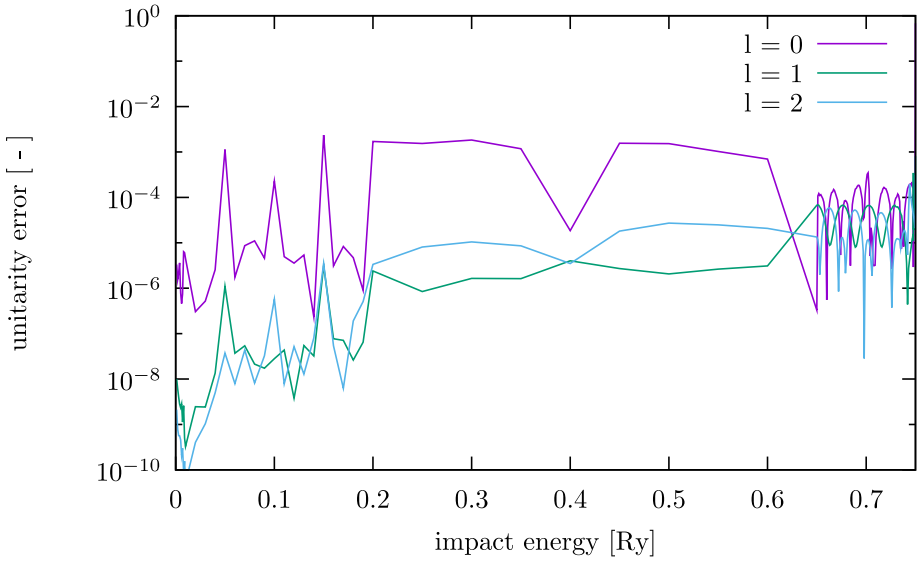

Figure 6.5: Unitarity error for three lowest partial waves for impact energies below the first excitation threshold. The error is always less than or equal to approximately one part in a thousand.

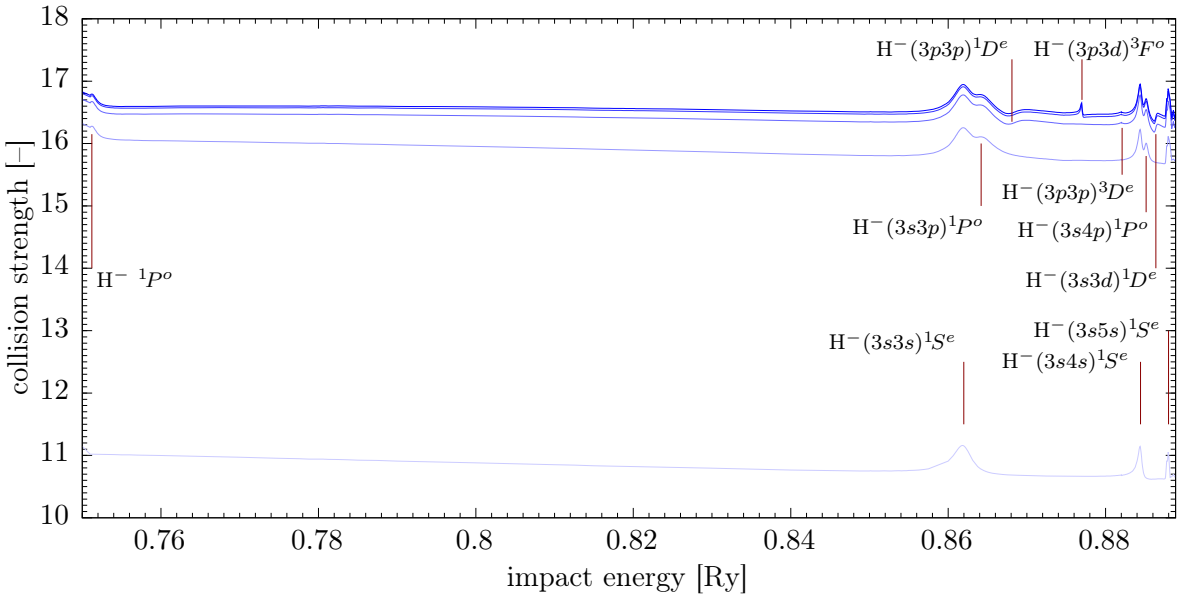

Figure 6.6: Partial wave convergence of the collision strengths for elastic scattering on the ground state H($1s$) at energies between the $n = 2$ and $n = 3$ thresholds. Figure displays 5 partial waves.

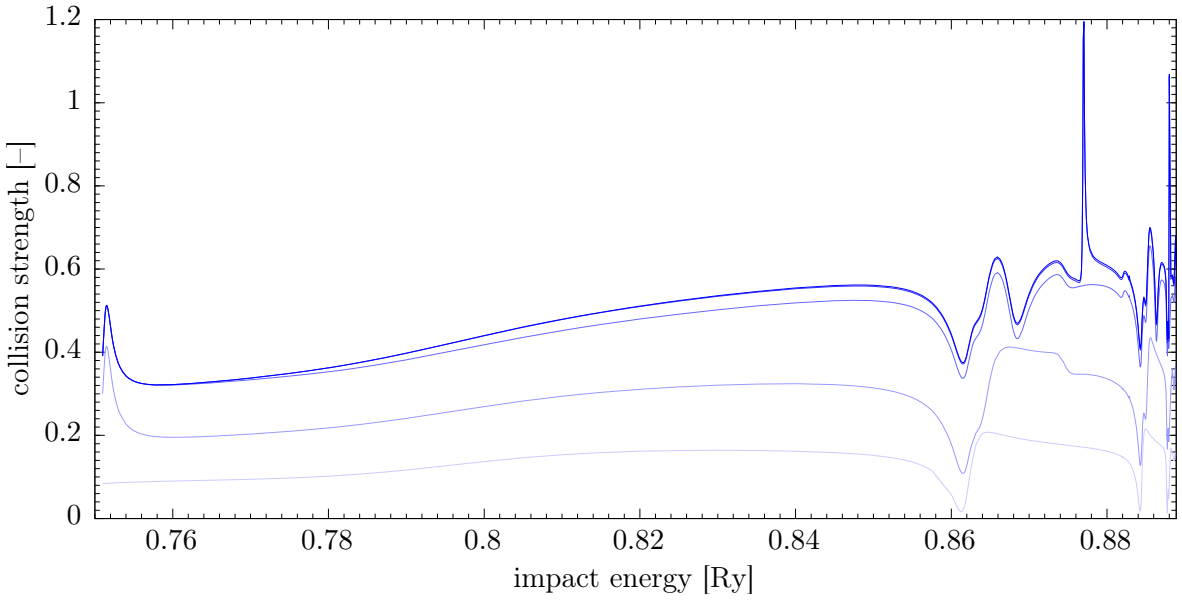

Figure 6.7: Partial wave convergence of the collision strengths for excitation from the ground state H($1s$) to H($2s$) between the $n = 2$ and $n = 3$ thresholds. Figure displays 5 partial waves.

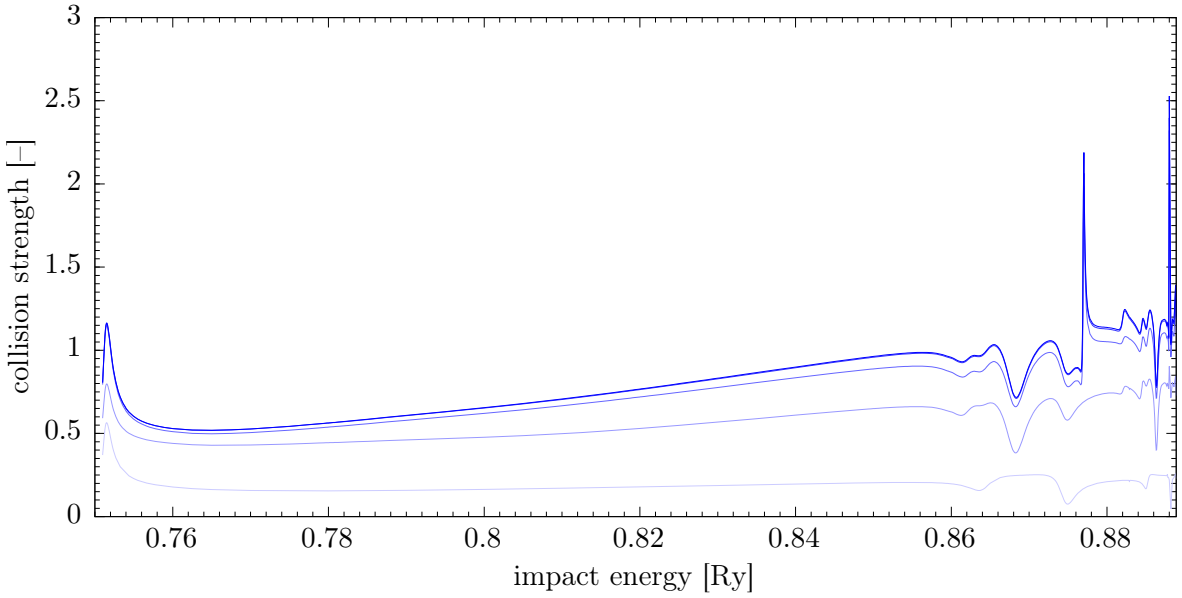

Figure 6.8: Partial wave convergence of the summed collision strengths for excitation from H($1s$) to the three magnetic sublevels of H($2p$) between the $n = 2$ and $n = 3$ thresholds. Figure displays 5 partial waves.

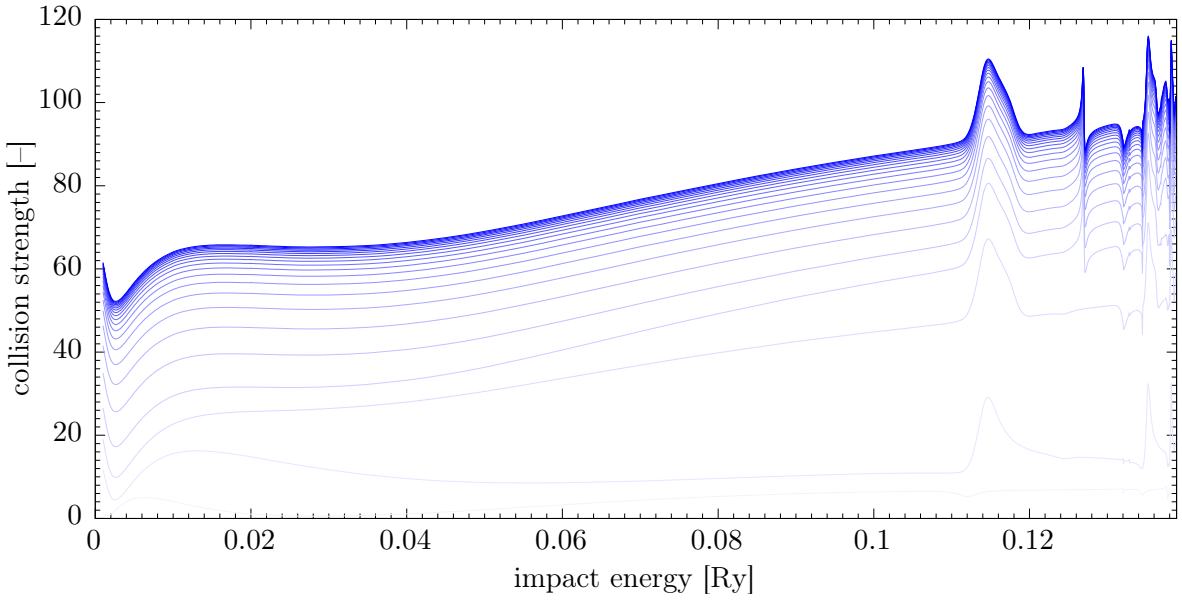

Figure 6.9: Partial wave convergence of the collision strengths for elastic scattering on the excited state H($2s$) between the $n = 2$ and $n = 3$ thresholds. A considerably larger amount of partial waves (20 displayed) is needed for converged values compared e.g. to the inelastic transition in the figure 6.7. This is a direct consequence of the slow decay of the elastic partial T-matrices, eq. (5.2).

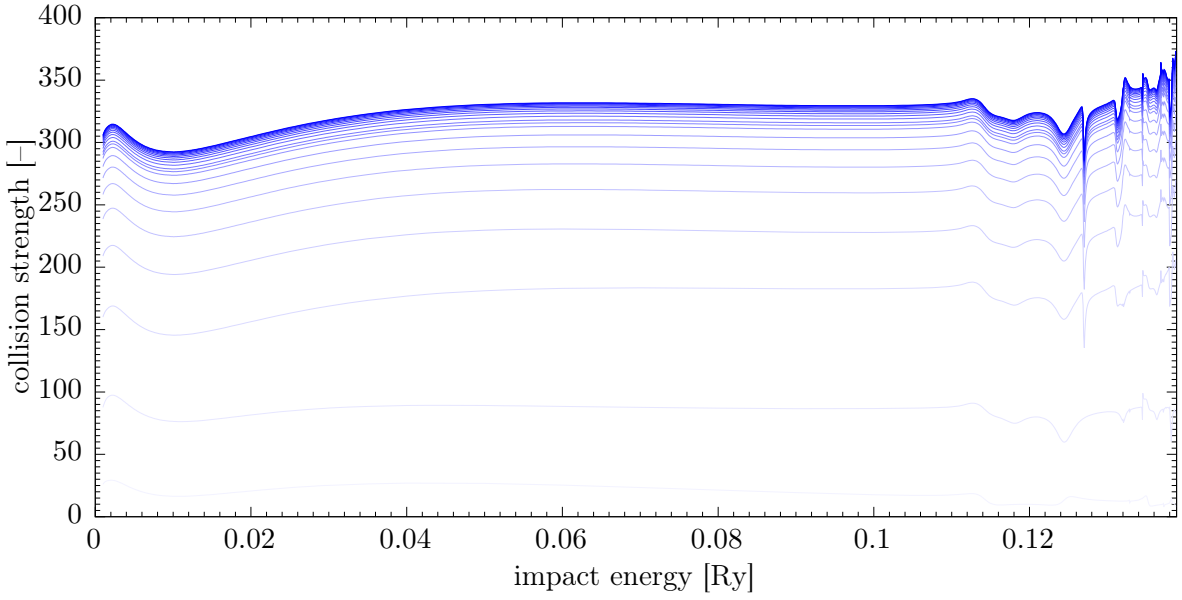

Figure 6.10: Partial wave convergence of the collision strengths for elastic scattering at the excited state H($2p$) between the $n = 2$ and $n = 3$ thresholds, summed over all initial and final magnetic sublevels. Figure displays 20 partial waves.

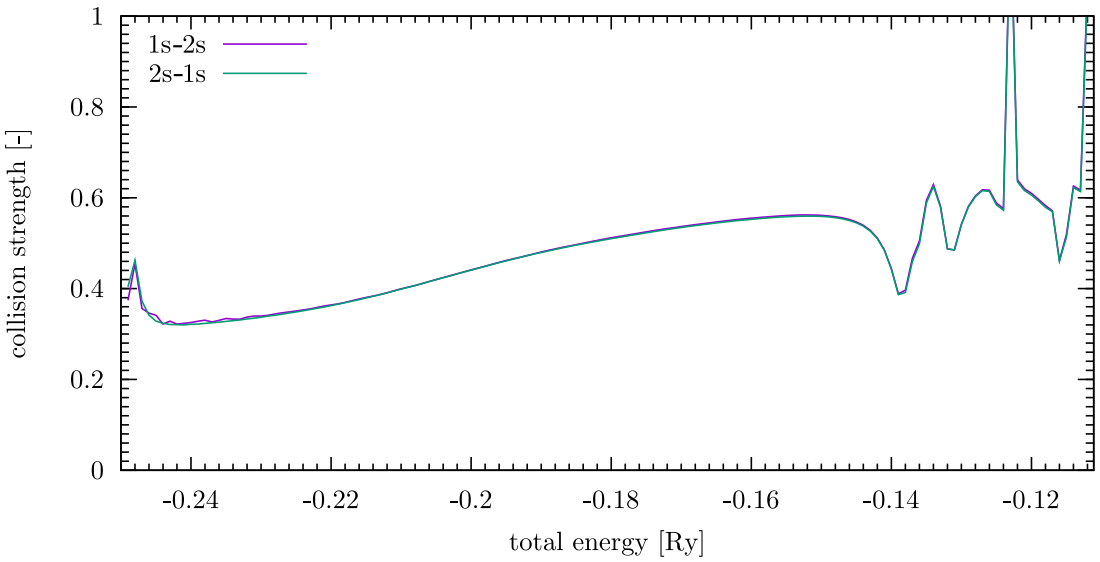

Figure 6.11: Comparison of the $1s - 2s$ and $2s - 1s$ transition data in terms of the detailed balance theorem. The datasets are very close to each other.

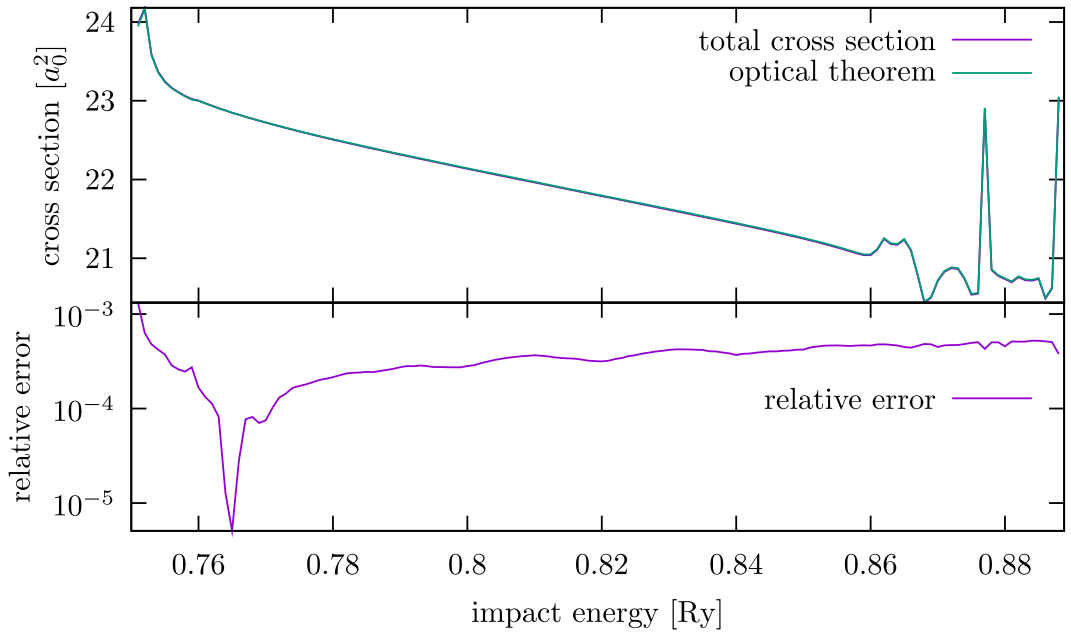

Figure 6.12: Comparison of the (grand) total cross section of scattering on the ground state calculated by summing cross sections for individual excitations and by employing the optical potential (5.5). The two curves are visually indistinguishable; the relative difference (plotted in the bottom half) is always smaller than 1 %.

6.6 Between $n = 3$ and $n = 4$ thresholds

The number of possible states rapidly increases with rising energy of the system. It is well-known that above the threshold of the n-th level there are n^2 unique states $|nl\rangle$, and $n(n+1)(2n+1)/6$ unique states $|nlm\rangle$. While in the region between $n = 2$ and $n = 3$ thresholds this evaluates to just 5 possible atomic states (including magnetic sub-levels), above the $n = 3$ threshold the set of targets expands to 14 states.

The partial wave convergence of the results in this energy domain is shown in the figures 6.13–6.30. Again, datasets for the elastic scattering needed a large amount of partial waves to converge, figures 6.19, 6.23, 6.27, 6.29 and 6.30.

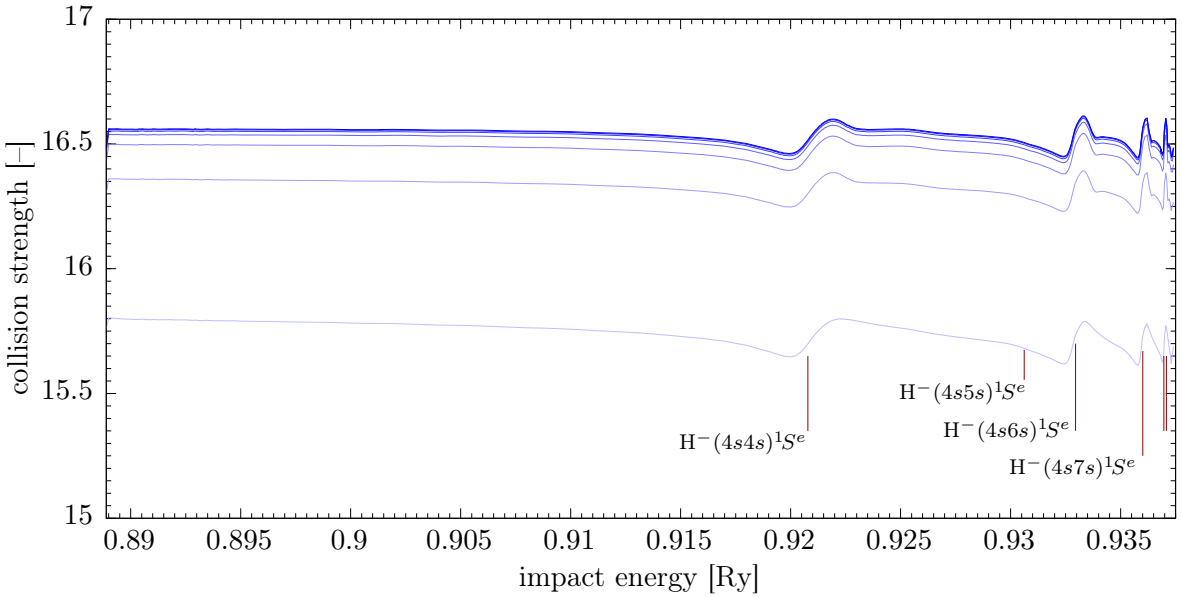

Figure 6.13: Partial wave convergence of the collision strengths for elastic scattering on the ground state H($1s$) at energies between the $n = 3$ and $n = 4$ thresholds. To make the resonances more apparent, the vertical scale has been adjusted; the lowest $L = 0$ partial wave is thus not visible in the figure. Figure displays 7 partial waves.

6.7 Higher energies

Many calculations of the scattering at higher energies have been done to verify that the codes work perfectly in the vicinity of the ionization threshold and above. However, systematic treatment of further datasets did not finish before the end of this doctoral project and thus are not present in this text. Still, the calculations are underway to achive the intented goal and assemble the complete database (possibly limited to $n \sim 10$) that would be usable for plasma physics.

6.8 Differential cross section

Of the many differential scattering quantities that hex-db is able to calculate from the T-matrices the differential cross section has been chosen for illustration. The figures 6.31 and 6.32 present the differential collision strengths for excitations from $1s$ to $2s$ and $2p$, respectively, for all scattering angles and all impact energies currently available in the

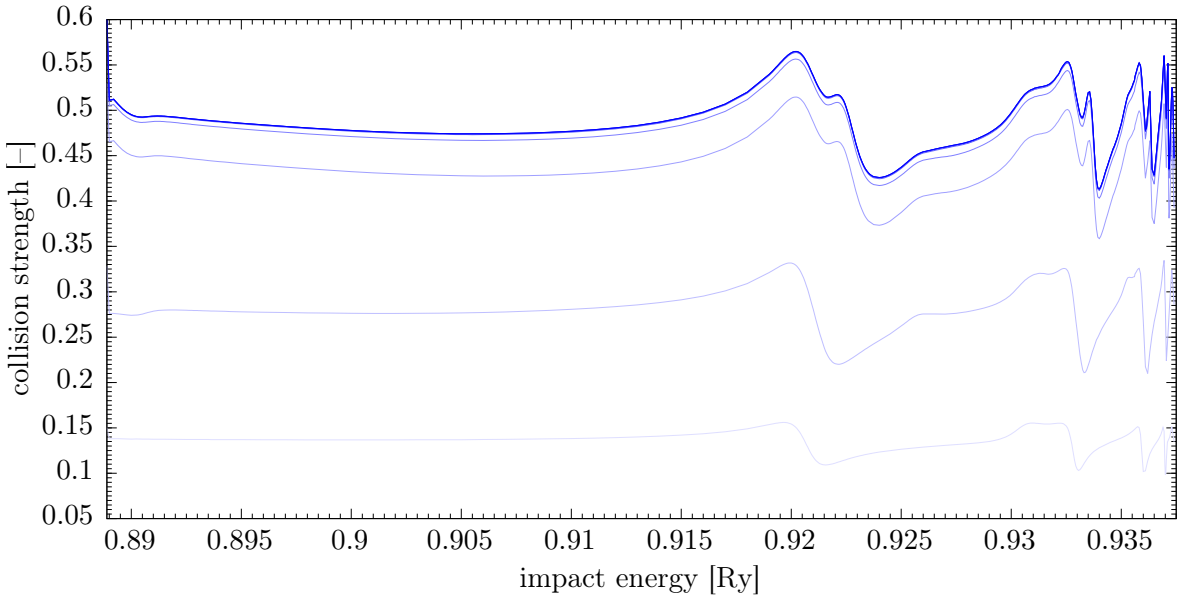

Figure 6.14: Partial wave convergence of the collision strengths for excitation from the ground state H($1s$) to H($2s$) between the $n = 3$ and $n = 4$ thresholds. Figure displays 8 partial waves.

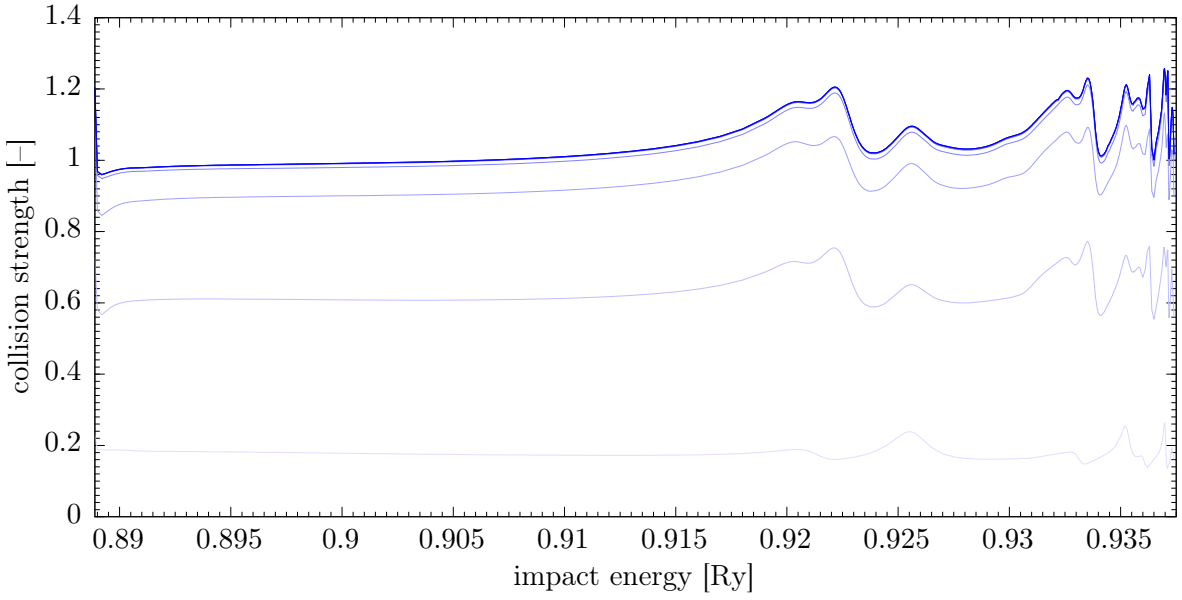

Figure 6.15: Partial wave convergence of the collision strengths for excitation from the ground state H($1s$) to H($2p$) between the $n = 3$ and $n = 4$ thresholds. Figure displays 8 partial waves.

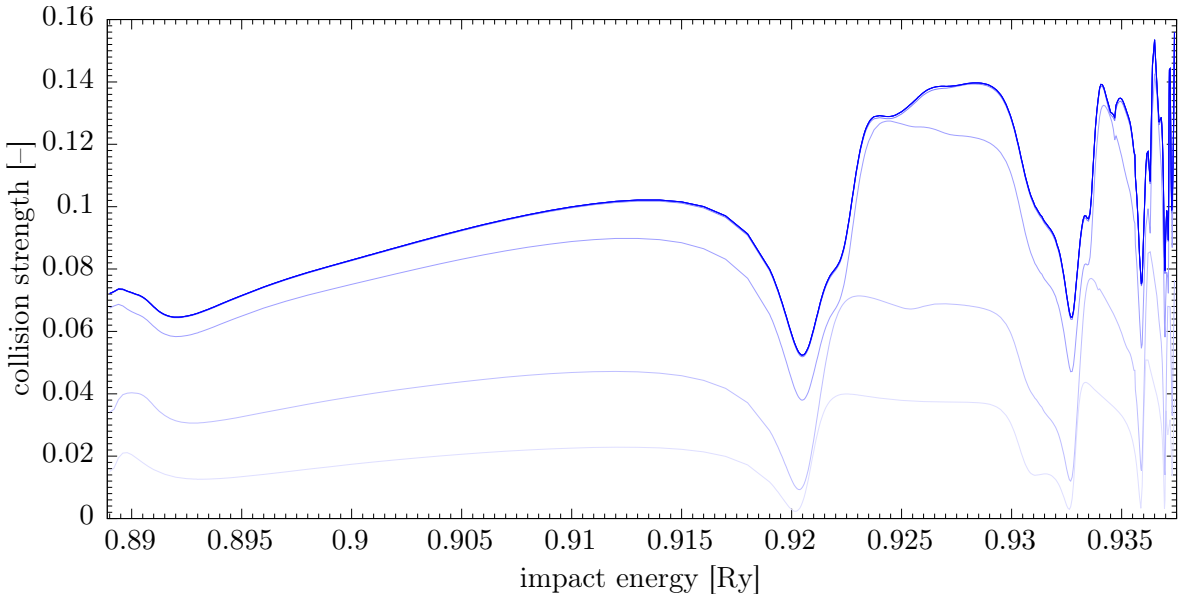

Figure 6.16: Partial wave convergence of the collision strengths for excitation from the ground state H($1s$) to H($3s$) between the $n = 3$ and $n = 4$ thresholds. Figure displays 8 partial waves.

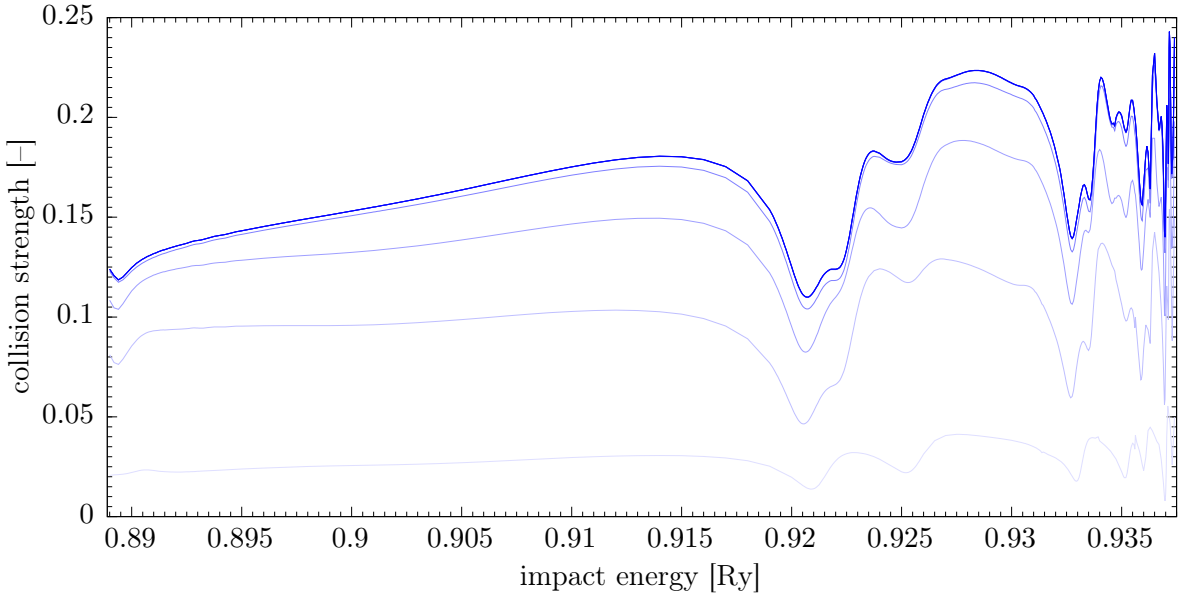

Figure 6.17: Partial wave convergence of the collision strengths for excitation from the ground state H($1s$) to H($3p$) between the $n = 3$ and $n = 4$ thresholds, summed over final magnetic sub-levels. Figure displays 8 partial waves.

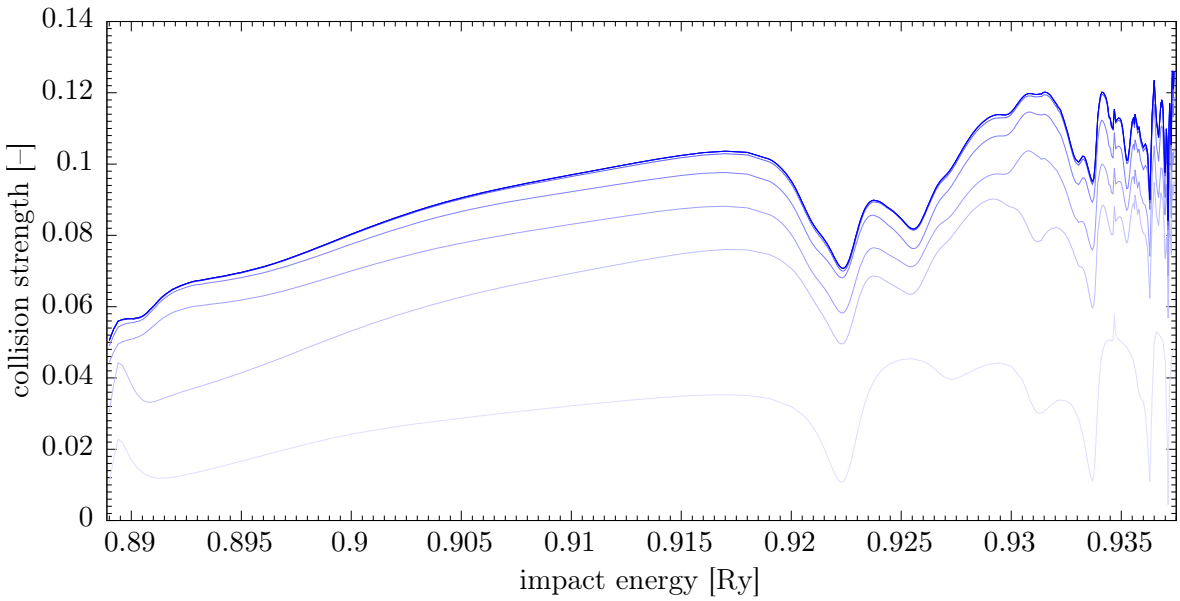

Figure 6.18: Partial wave convergence of the collision strengths for excitation from the ground state H($1s$) to H($3d$) between the $n = 3$ and $n = 4$ thresholds, summed over final magnetic sub-levels. Figure displays 8 partial waves.

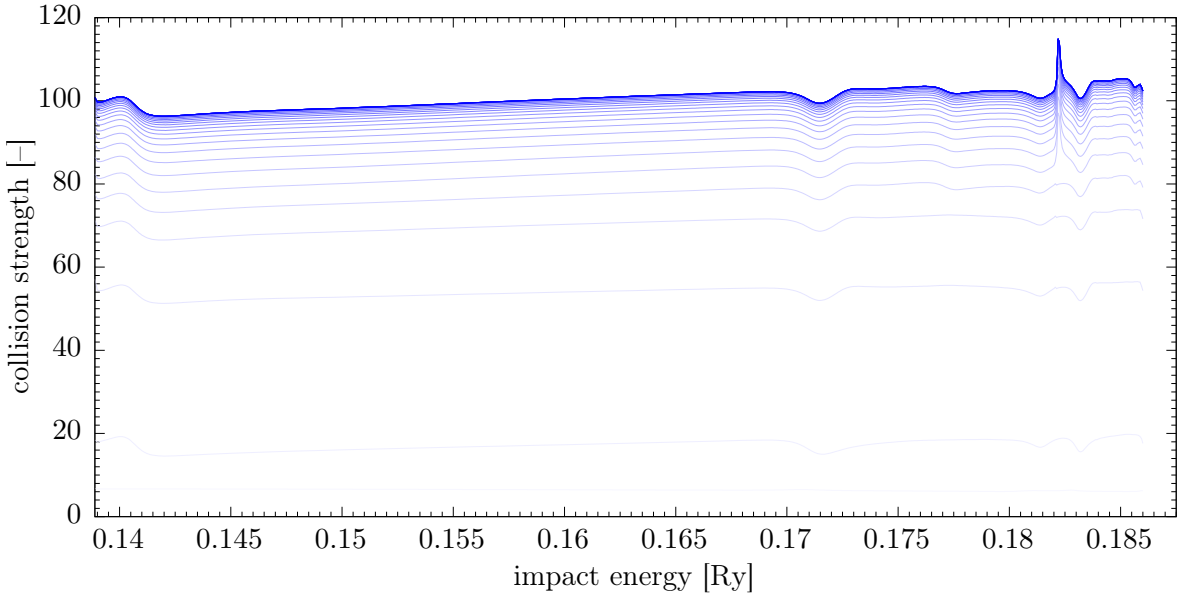

Figure 6.19: Partial wave convergence of the collision strengths for elastic scattering on the excited state H($2s$) at energies between the $n = 3$ and $n = 4$ thresholds. Figure displays 30 partial waves.

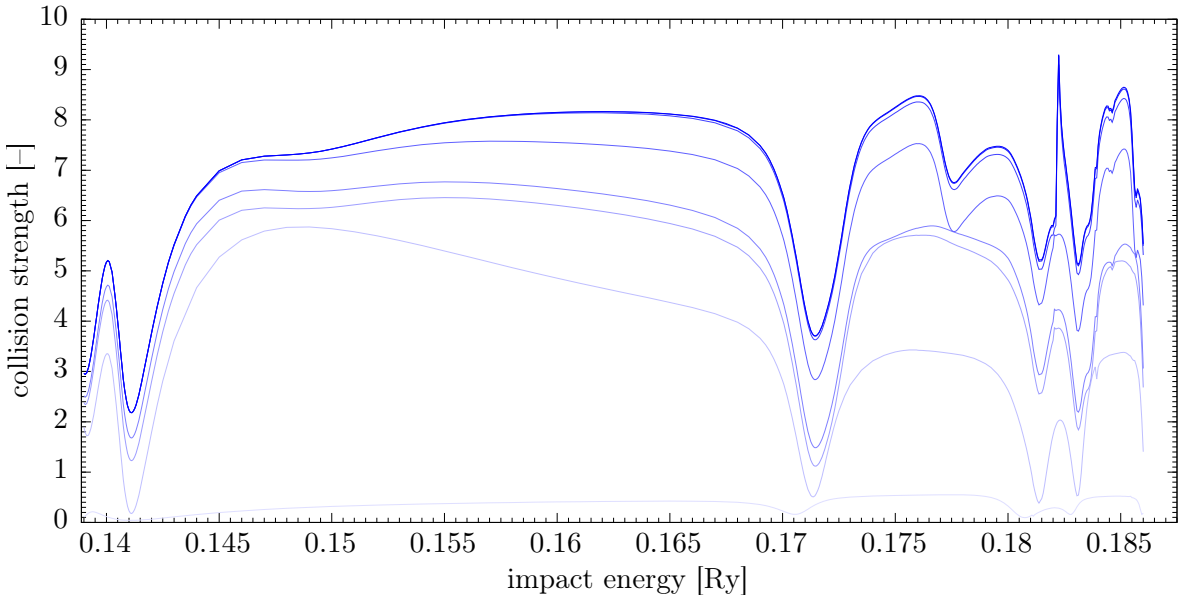

Figure 6.20: Partial wave convergence of the collision strengths for excitation from the excited state H($2s$) to H($3s$) between the $n = 3$ and $n = 4$ thresholds. Figure displays 8 partial waves.

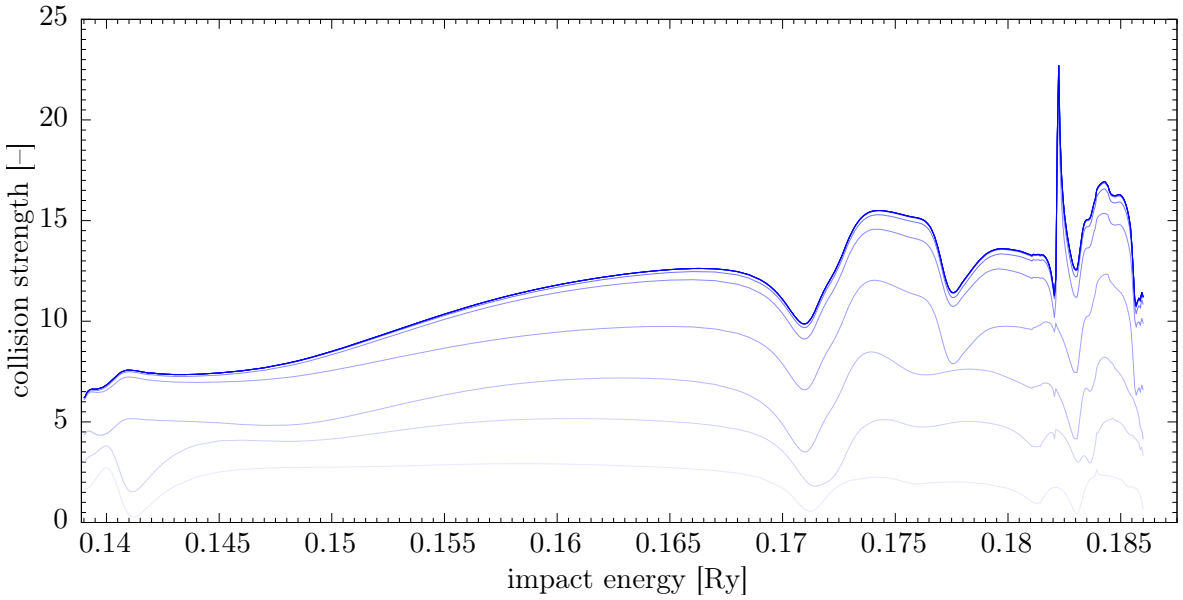

Figure 6.21: Partial wave convergence of the collision strengths for excitation from the excited state H($2s$) to H($3p$) between the $n = 3$ and $n = 4$ thresholds, summed over final magnetic sublevels. Figure displays 11 partial waves.

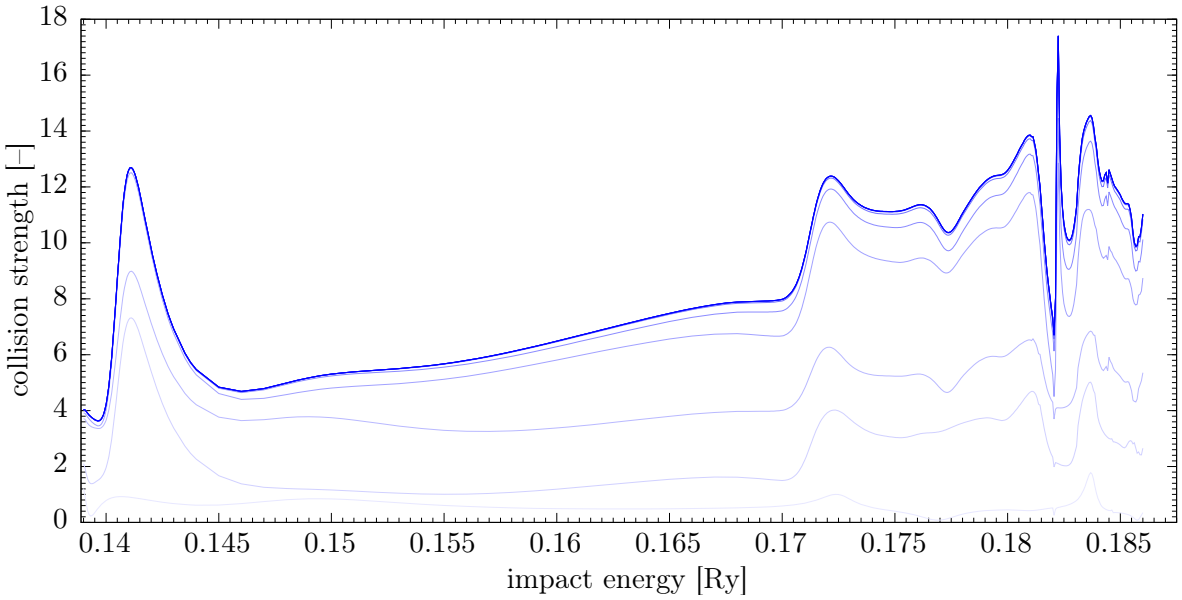

Figure 6.22: Partial wave convergence of the collision strengths for excitation from the excited state H($2s$) to H($3d$) between the $n = 3$ and $n = 4$ thresholds, summed over final magnetic sublevels. Figure displays 11 partial waves.

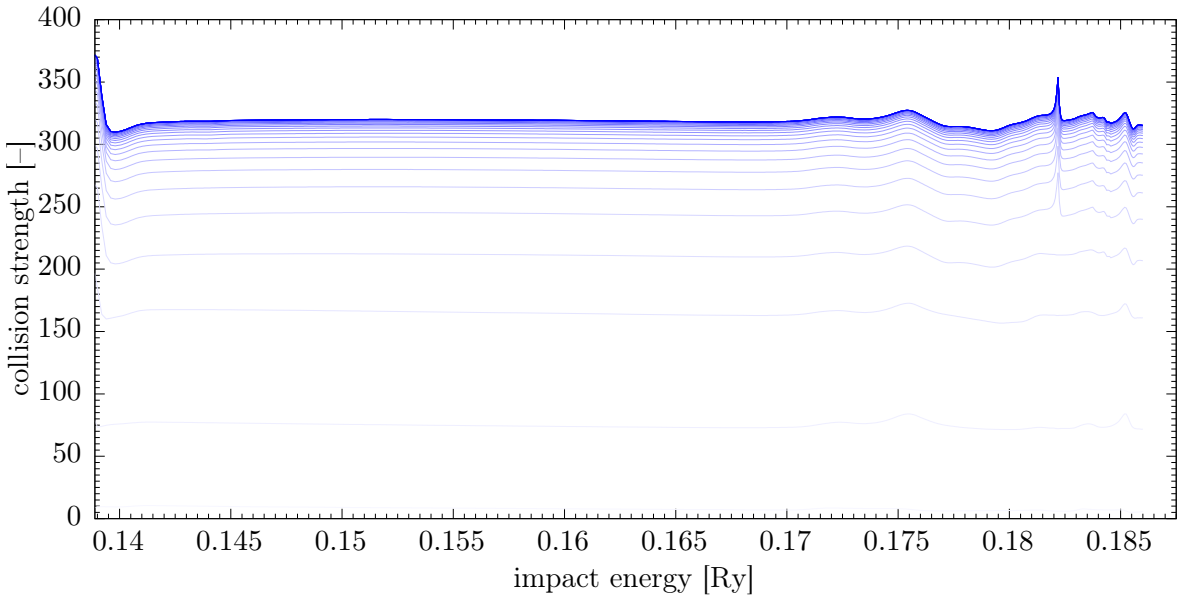

Figure 6.23: Partial wave convergence of the collision strengths for elastic scattering on the excited state H($2p$) at energies between the $n = 3$ and $n = 4$ thresholds, summed over initial and final magnetic sublevels. Figure displays 30 partial waves.

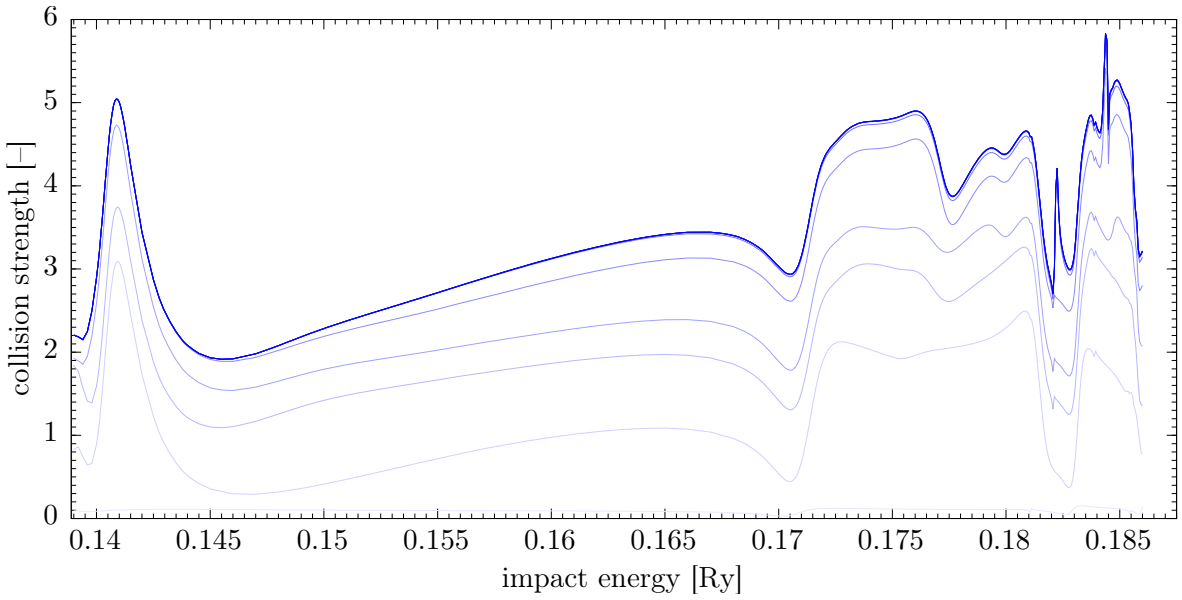

Figure 6.24: Partial wave convergence of the collision strengths for excitation from the excited state H($2p$) to H($3s$) between the $n = 3$ and $n = 4$ thresholds, summed over initial magnetic sublevels. Figure displays 11 partial waves.

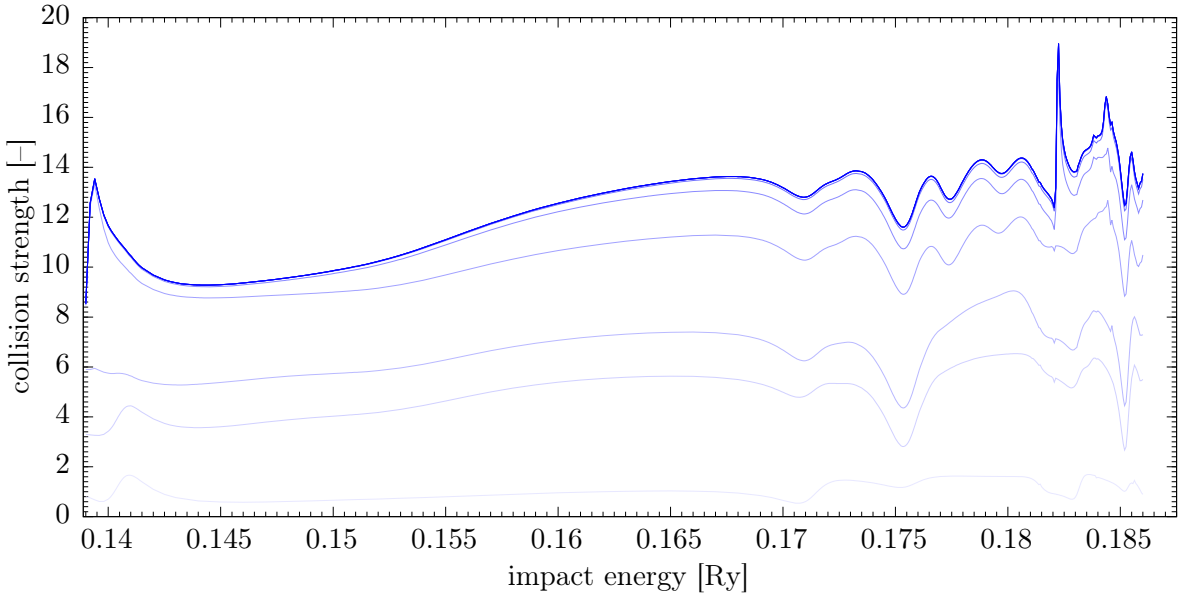

Figure 6.25: Partial wave convergence of the collision strengths for excitation from the excited state H($2p$) to H($3p$) between the $n = 3$ and $n = 4$ thresholds, summed over initial and final magnetic sublevels. Figure displays 11 partial waves.

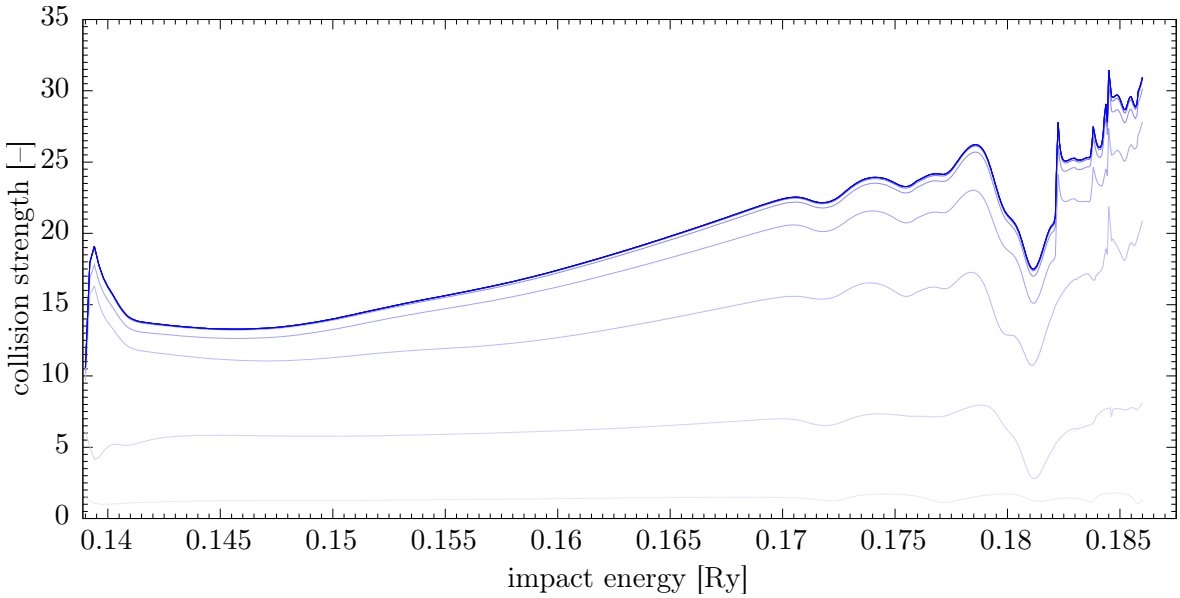

Figure 6.26: Partial wave convergence of the collision strengths for excitation from the excited state H($2p$) to H($3d$) between the $n = 3$ and $n = 4$ thresholds, summed over initial and final magnetic sublevels. Figure displays 11 partial waves.

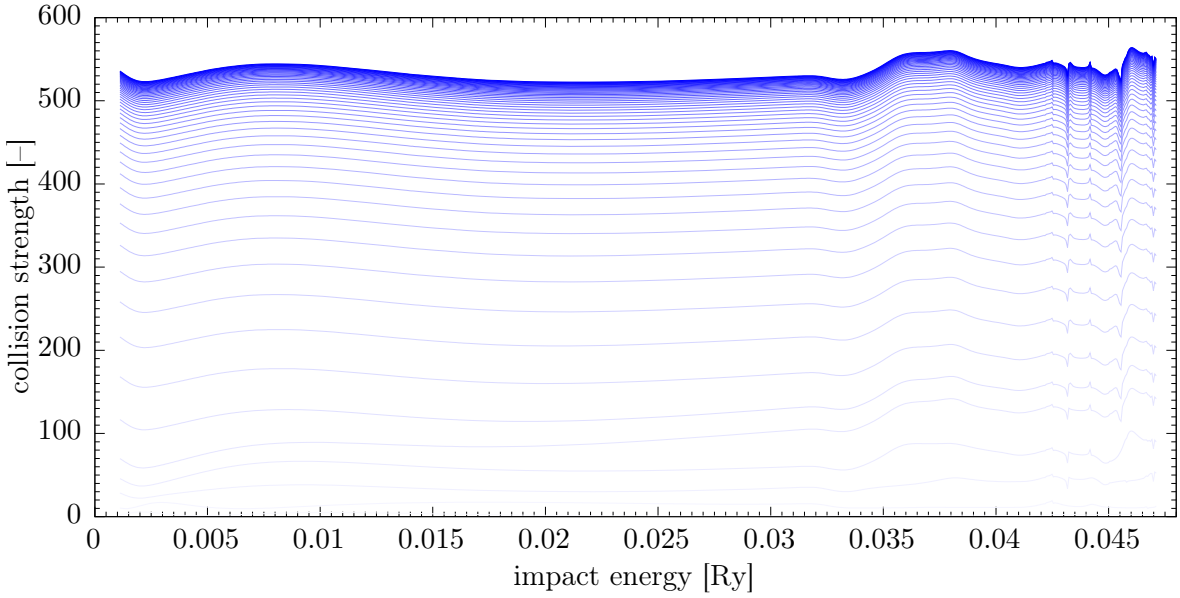

Figure 6.27: Partial wave convergence of the collision strengths for elastic scattering on the excited state H($3s$) at energies between the $n = 3$ and $n = 4$ thresholds. Figure displays 50 partial waves.

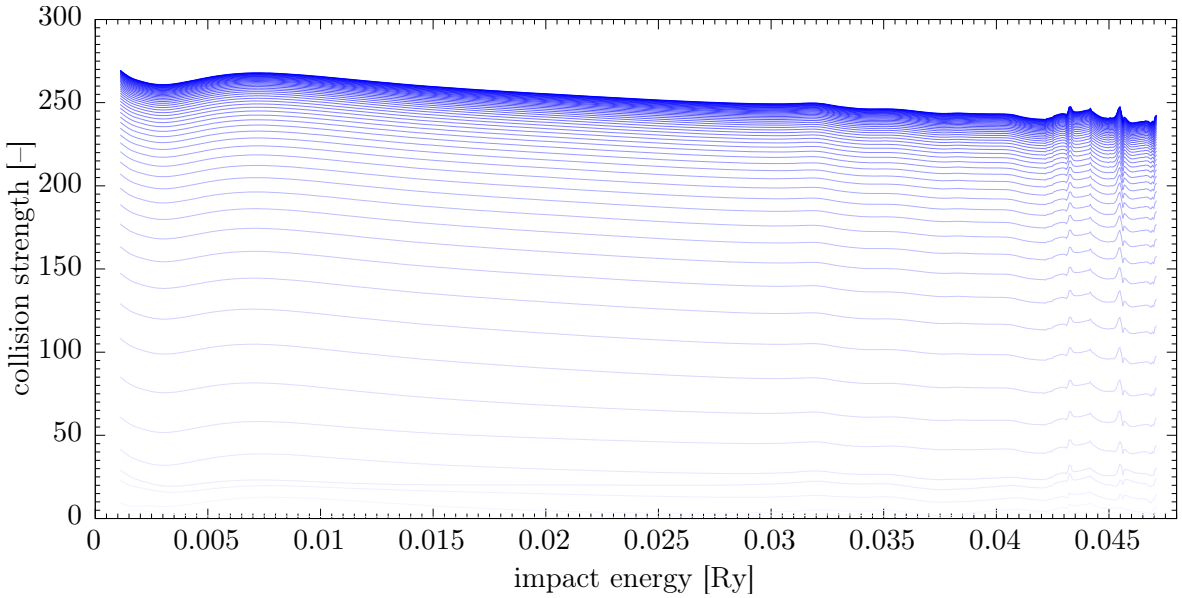

Figure 6.28: Partial wave convergence of the collision strengths for degenerate (but non-dipole, hence finite) transition from the excited state H($3s$) to H($3d$) between the $n = 3$ and $n = 4$ thresholds, summed over final magnetic sublevels. Figure displays 50 partial waves.

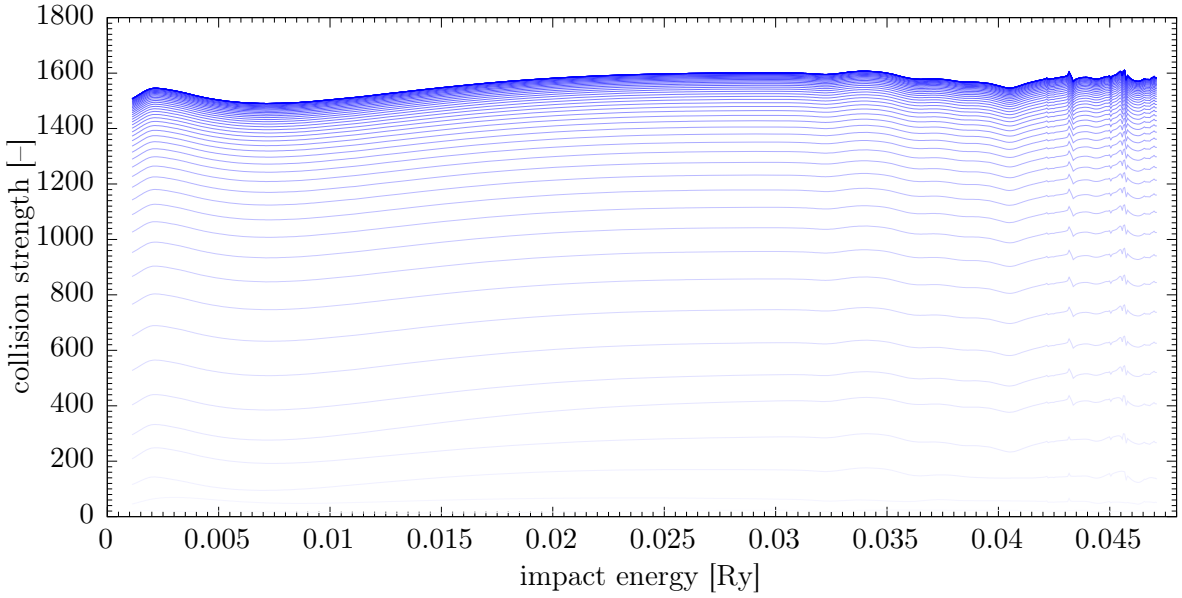

Figure 6.29: Partial wave convergence of the collision strengths for elastic scattering on the excited state H($3p$) at energies between the $n = 3$ and $n = 4$ thresholds, summed over initial and final magnetic sublevels. Figure displays 50 partial waves.

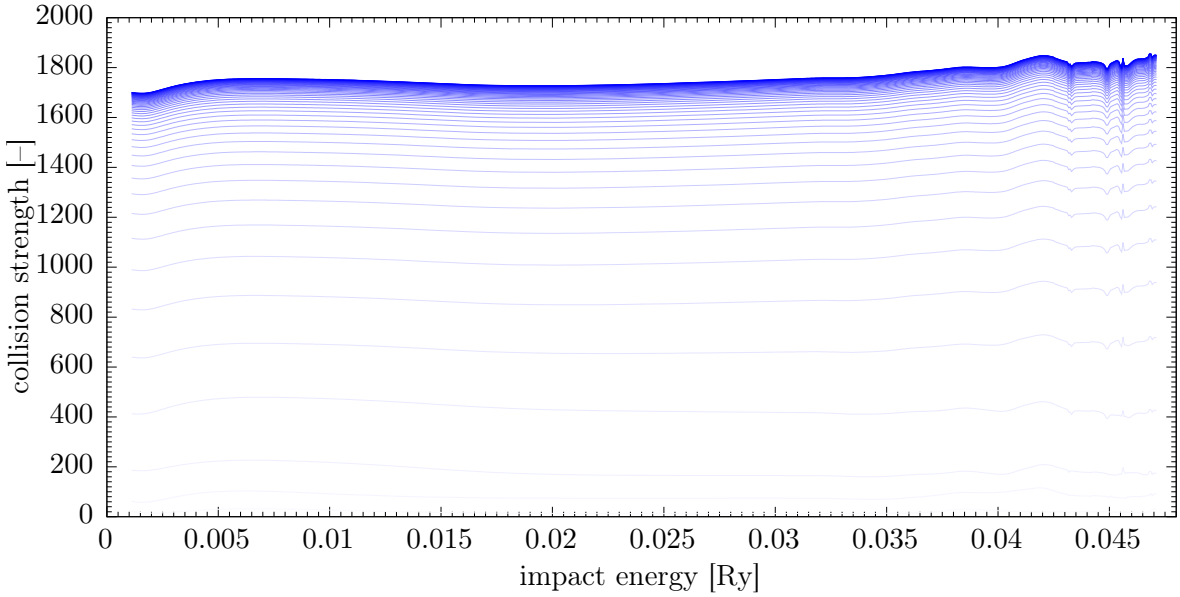

Figure 6.30: Partial wave convergence of the collision strengths for elastic scattering on the excited state H($3d$) at energies between the $n = 3$ and $n = 4$ thresholds, summed over initial and final magnetic sublevels. Figure displays 50 partial waves.

database. The differential scattering strength is proportional to the differential cross section,

$$\frac{\mathrm{d}\Omega_{ji}}{\mathrm{d}\Omega} = k_i^2 \frac{\mathrm{d}\sigma_{ji}}{\mathrm{d}\Omega}\,, \tag{6.3}$$

where the symbols Ω_{ij} (collision strength) and Ω (solid angle) need to be distinguished. Change of the angular distribution of the scattered electron at resonance energies can be well observed.

6.9 Validation of new results against existing data

As mentioned in introduction, there had been a considerable effort to assemble electron-hydrogen scattering data already in the last quarter of the 20$^{\mathrm{th}}$ century. A legacy of that time is a large amount of incoherent datasets, which have been reviewed in [**78**]. The figures 6.33–6.43 in this section demonstrate agreement between the newly calculated data and already existing data, where available.

The main source of reference data has been the atomic database Aladdin managed by IAEA, containing most complete datasets. This database, though mostly aimed at high-energy plasma physics, is also often used by astronomers. Results of the present work should supplement and refine the data in Aladdin. Other reference data include general close-coupling, R-matrix and PECS calculations listed in the introduction.

Elastic scattering on the ground state (figure 6.33) and excitations from the ground state to states with $n_f = 2$ (figure 6.34) are compared with many datasets of high accuracy and there is hardly any discrepancy between the present calculation and available calculations. The same agreement is observed in case of de-excitation from the states with $n_i = 2$ (figure 6.36).

The agreement is less apparent for excitation from the ground state to states with $n_f = 3$ (figure 6.35). While the PECS results almost perfectly coincide with current calculation, the R-matrix calculation done by Aggarwal resulted in systematically higher

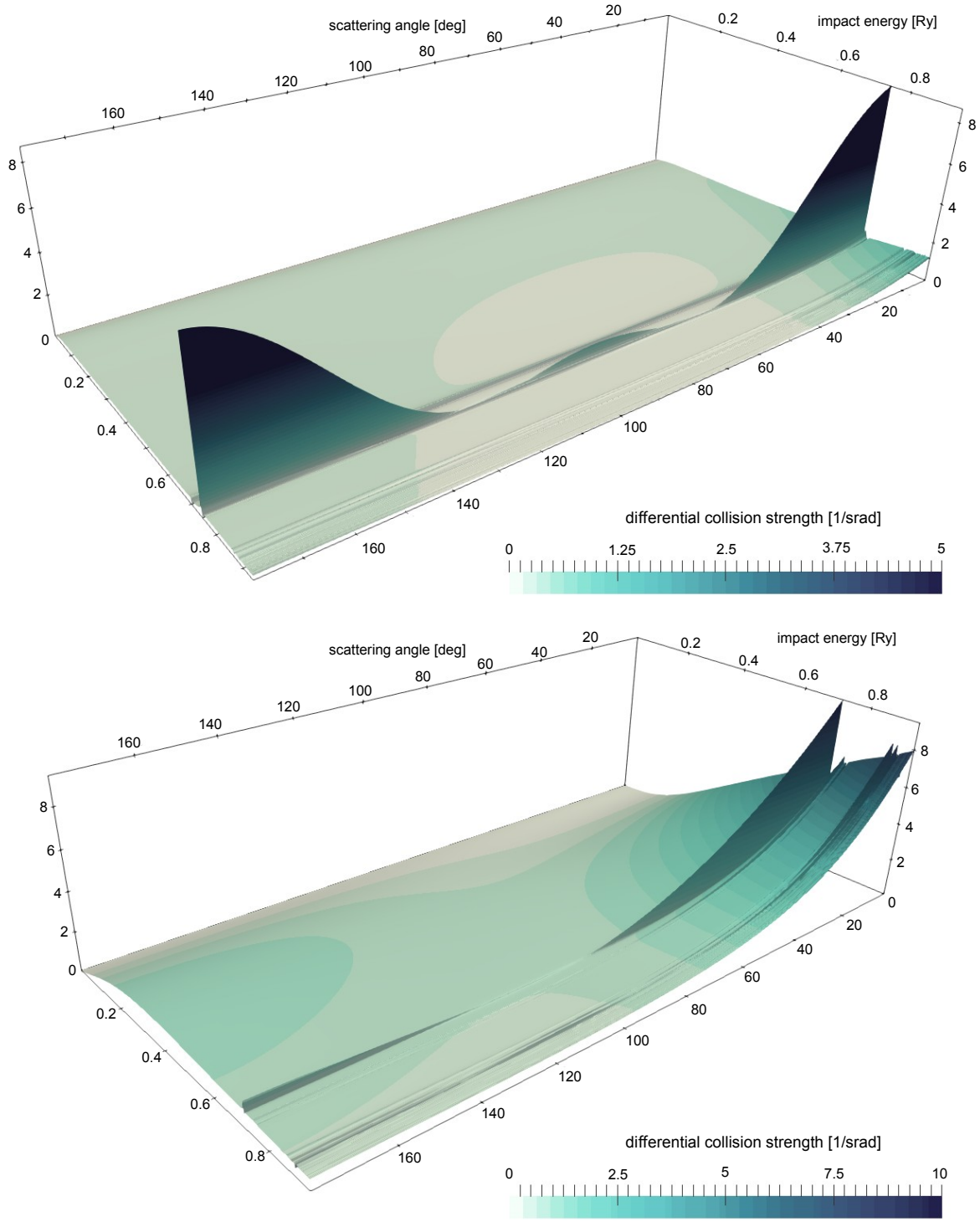

Figure 6.31: Energy dependency of the differential collision strength for the elastic process $\mathrm{H}(1s) \rightarrow \mathrm{H}(1s)$; top figure is for total $S = 0$, bottom for $S = 1$.

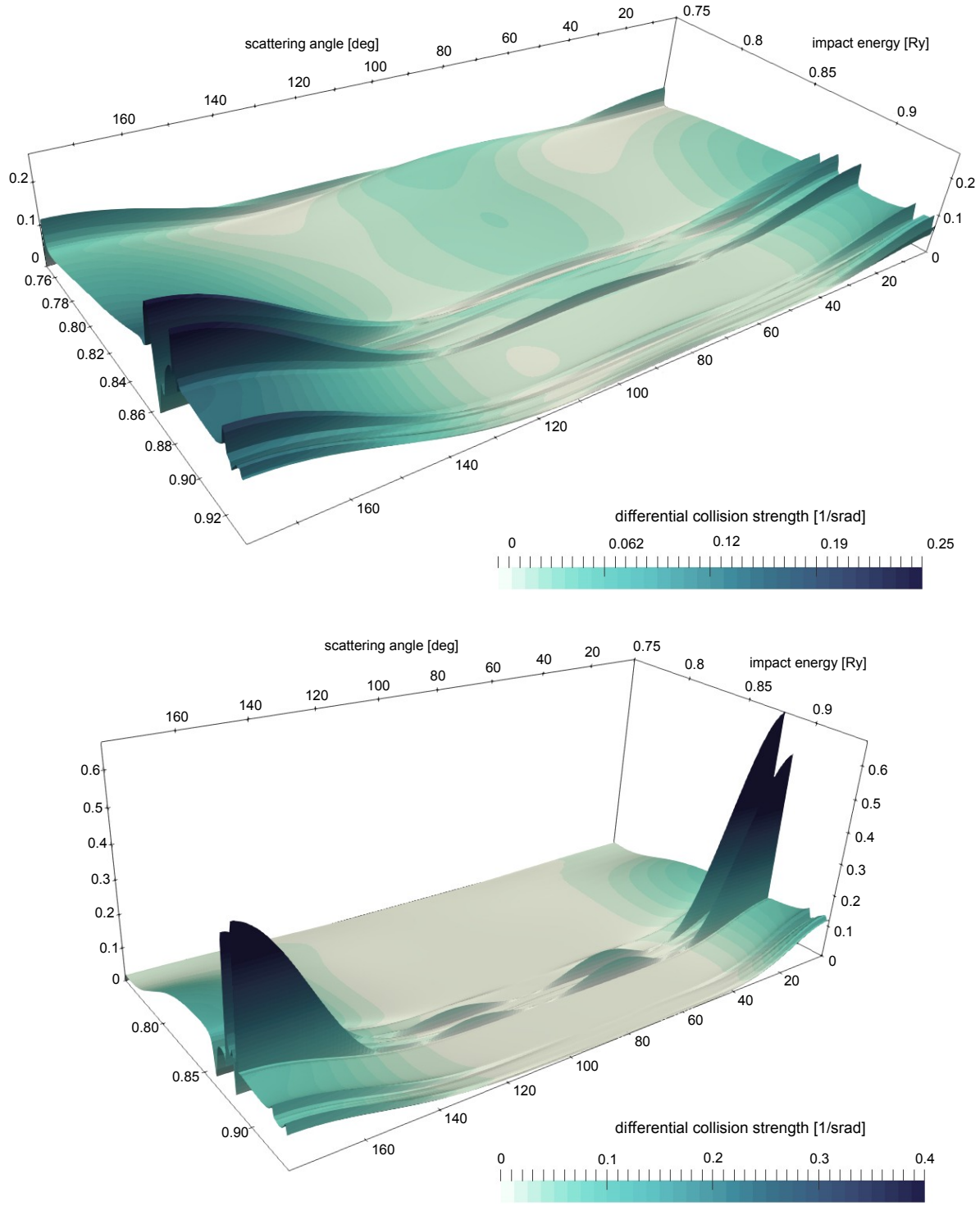

Figure 6.32: Energy dependency of the differential collision strength for the excitation H($1s$) $\rightarrow$ H($2s$); top figure is for total $S = 0$, bottom for $S = 1$.

collision strengths and the data from Aladdin are rather irregularly scattered along the ECS results. Given the coincidence with PECS, it can be assumed that the present data are equally accurate. Actually, thanks to the channel reduction method allowing a closer approach to the threshold of the $n = 3$ channel, present results deliver wider energy range than PECS.

The results of Aggarwal seem to match the present results much better for excitations from $n = 2$ to $n = 3$ states, as shown in the figures 6.39 and 6.40, though the energy range offered by hex-ecs proves superior.

For all other transitions only comparison with Aladdin datasets is possible. The agreement is mostly acceptable for inelastic transitions. However, collision strengths for elastic scattering on excited states provided by Aladdin differ strongly from those calculated in this work, typically by more than 10 %. Elastic scattering at low energies is dominated by polarization, as discussed above. Polarization is a long-range interaction, so its accurate treatment needs inclusion of large space surrounding the atom. Because the similarity between Aladdin and Hex data worsens when getting closer to the opening of the scattering channel, it is likely that this long-range interaction had not been accounted for very well in Aladdin. Furthermore, the partial wave convergence illustrations from previous sections demonstrated that for elastic scattering the convergence is very slow. The Aladdin data, located always below the Hex data, probably suffer from insufficient convergence in terms of partial waves.

Considering the comparisons, it is possible to conclude that the results offered by this thesis (and published in [78]) agree well with independent calculations and most probably provide as accurate results even for energies where comparison was not possible.

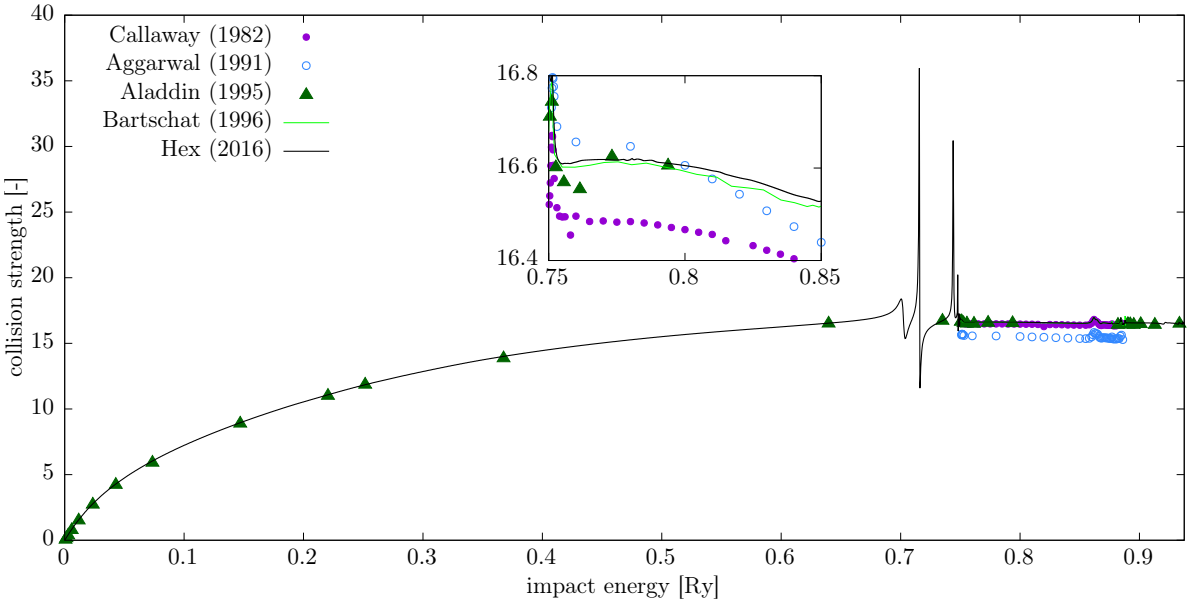

Figure 6.33: Elastic collision strengths on the ground state compared with calculations of Callaway [8], Aggarwal [10], Bartschat [12] and with the data from Aladdin [16].

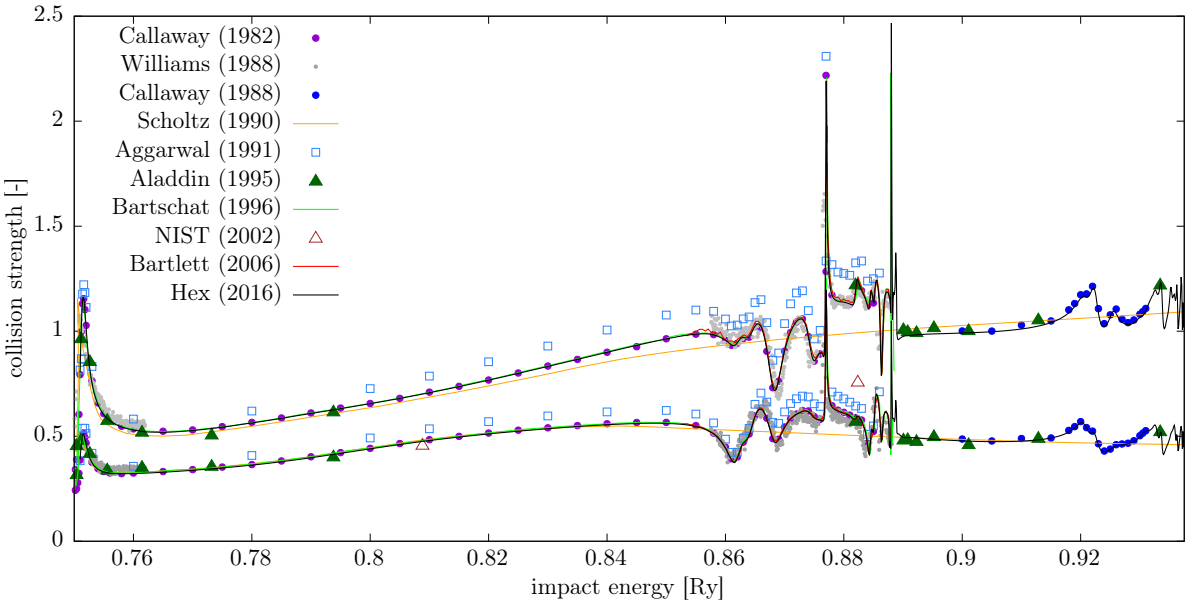

Figure 6.34: Collision strengths for excitations of the hydrogen ground state to H($2s$) and H($2p$), lower and upper curve, respectively, compared with the calculations of Callaway [8], [9], Scholtz [79], Aggarwal [10], Bartschat [12], Bartlett [15], with the measurement of Williams [80] and the data from the databases Aladdin [16] and NIST [19].

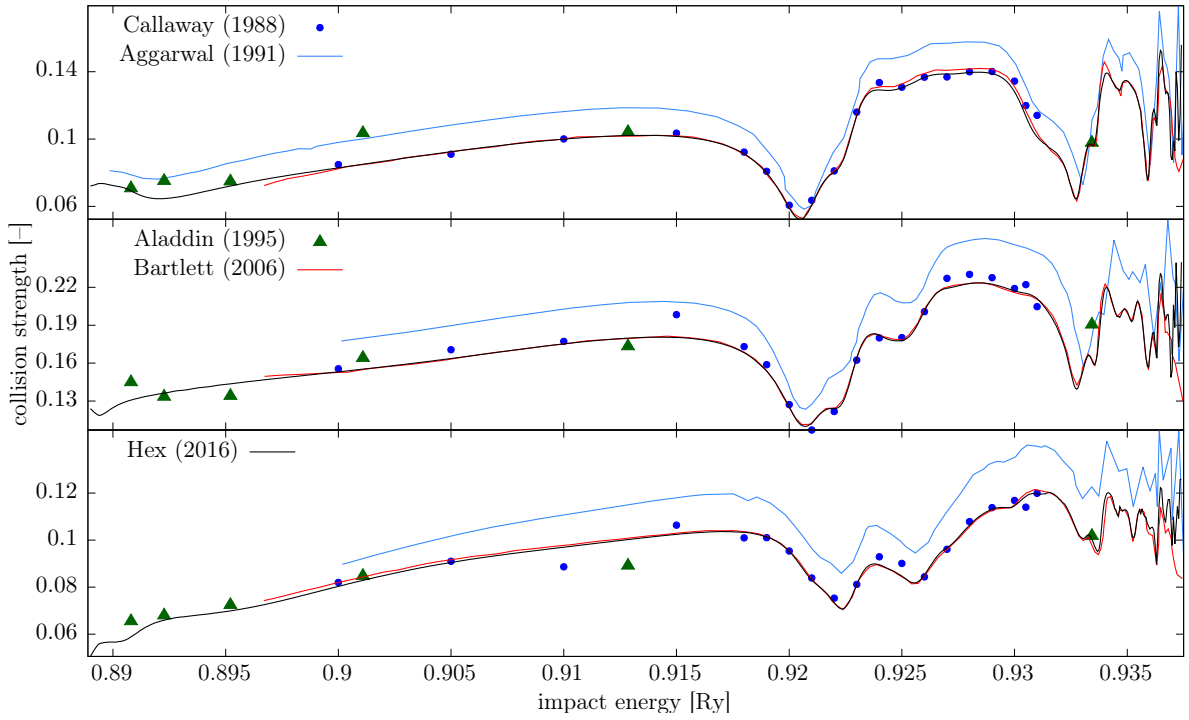

Figure 6.35: Collision strengths for excitations of the hydrogen ground state to H($3s$), H($3p$) and H($3d$), from top to bottom, compared with the calculations of Callaway [9], Aggarwal [10], Bartlett [15] and with the data from the database Aladdin [16].

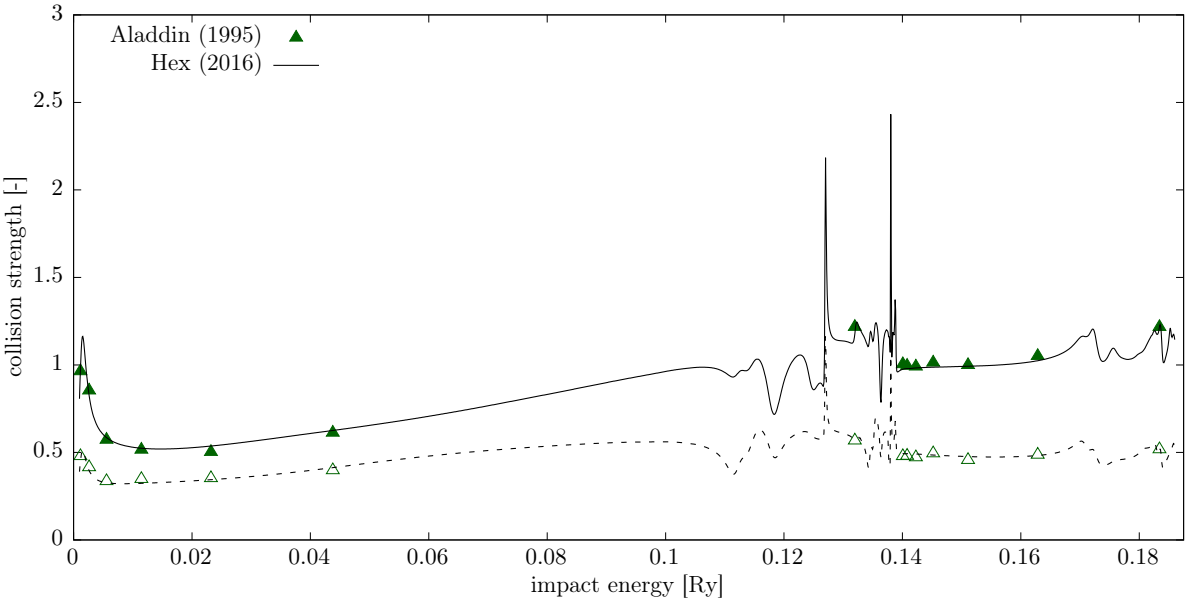

Figure 6.36: Collision strengths for de-excitation of H($2s$) and H($2p$) to H($1s$), bottom and top curves, respectively, compared to the data from the database Aladdin [16].

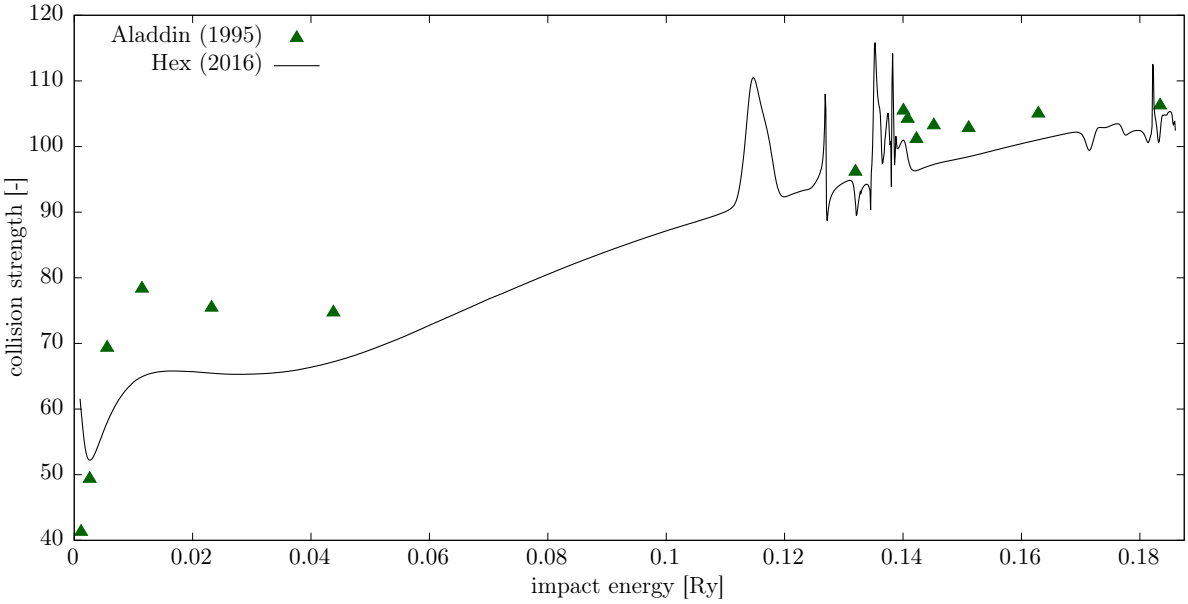

Figure 6.37: Collision strengths for elastic scattering on H($2s$) compared to the data from the database Aladdin [16].

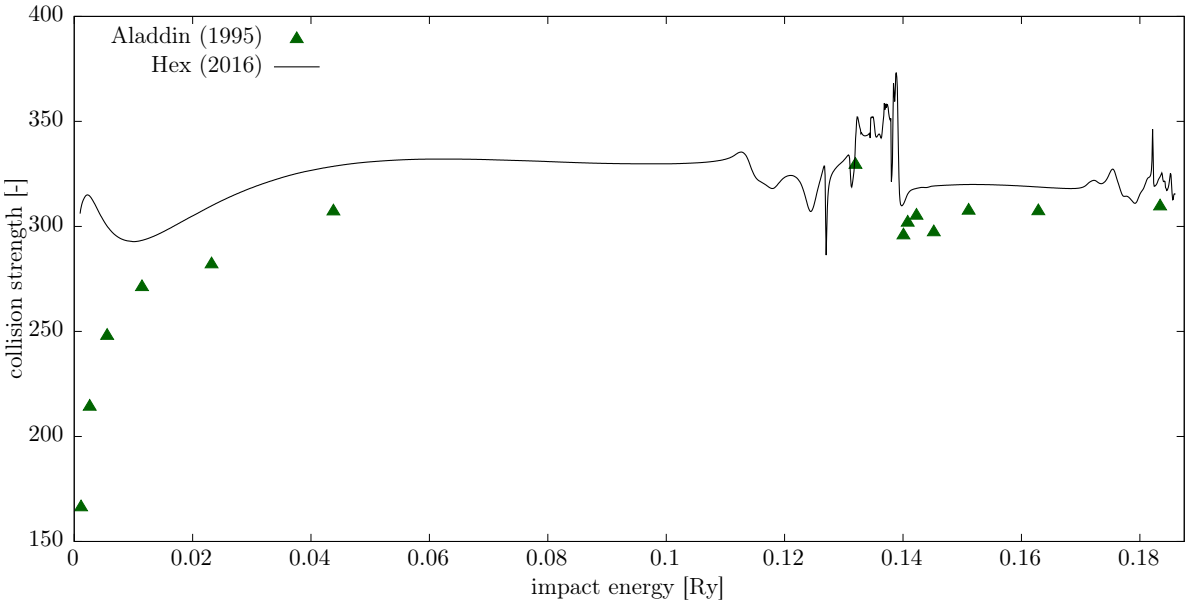

Figure 6.38: Collision strengths for elastic scattering on H($2p$) compared to the data from the database Aladdin [16].

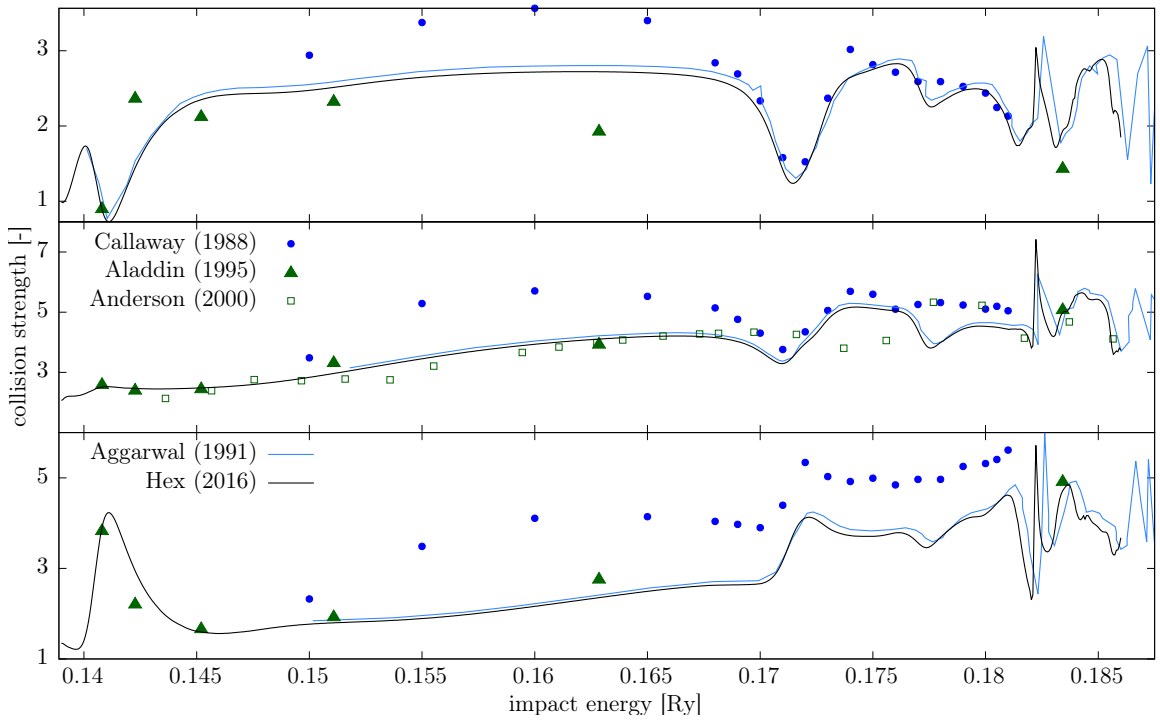

Figure 6.39: Collision strengths for excitation of H($2s$) to H($3s$), H($3p$) and H($3d$) compared to the calculation of Callaway [9], Aggarwal [10] and Anderson [14] and to the data from the database Aladdin [16].

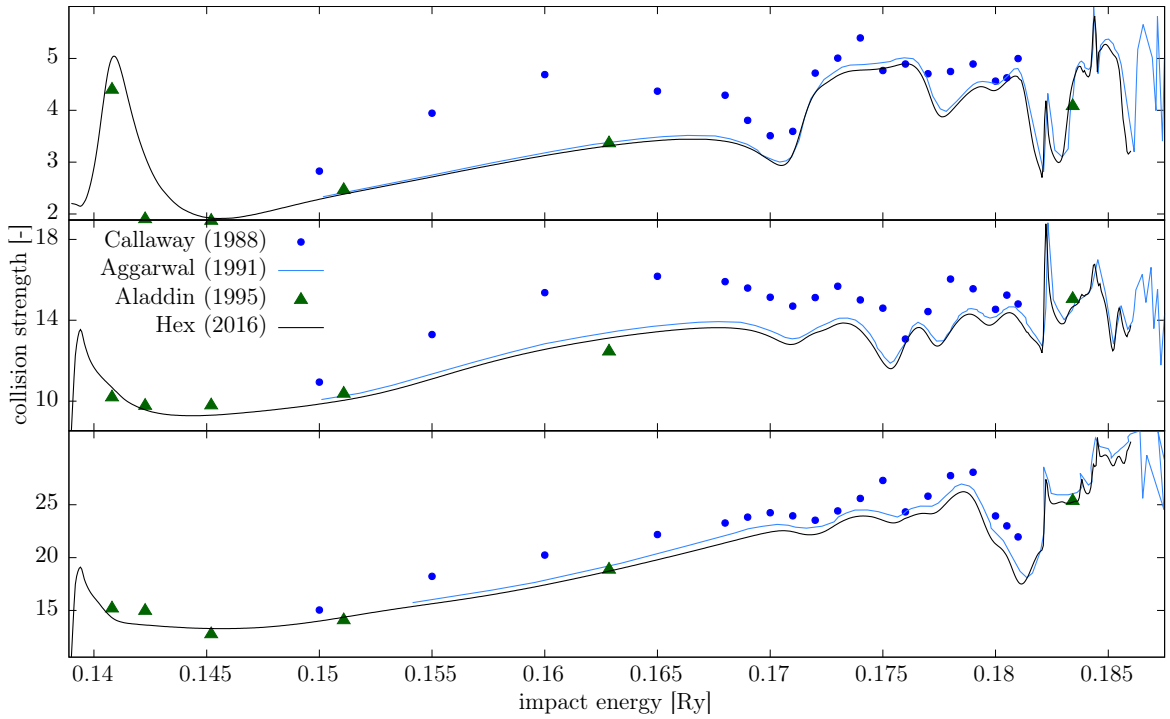

Figure 6.40: Collision strengths for excitation of H($2p$) to H($3s$), H($3p$) and H($3d$) compared to the calculation of Callaway [9] and Aggarwal [10] and to the data from the database Aladdin [16].

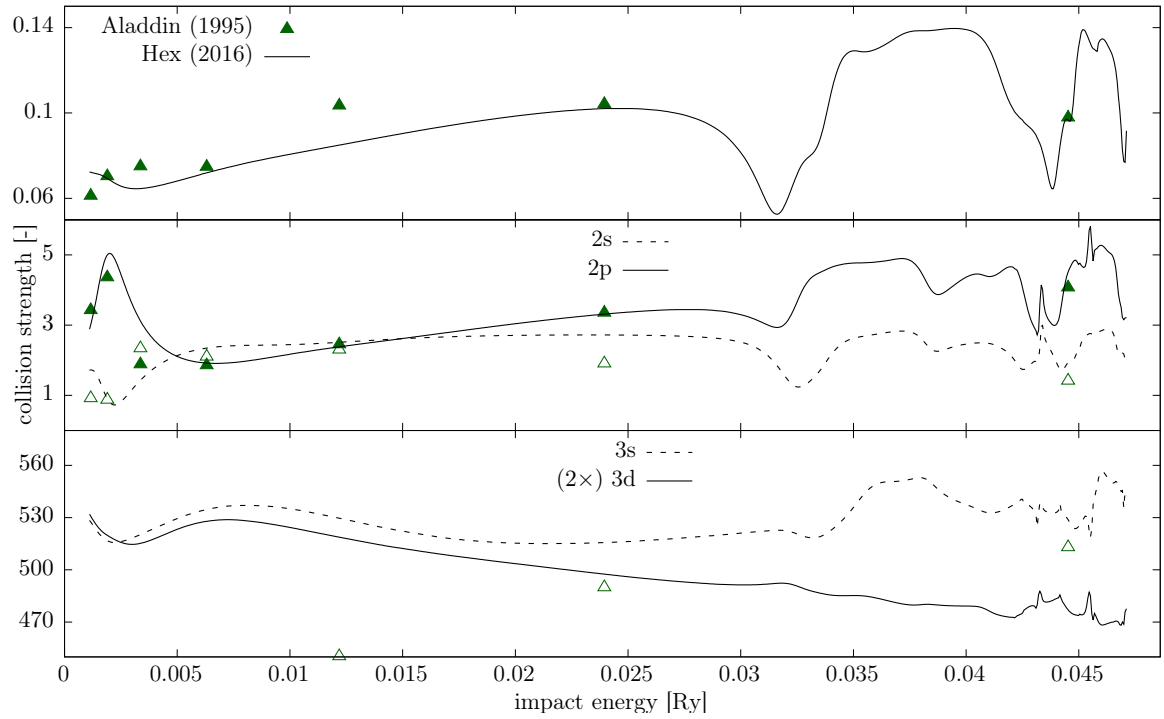

Figure 6.41: Collision strengths for processes from H($3s$) to H($1s$), H($2s$), H($2p$), H($3s$) and H($3d$) compared to the data from the database Aladdin [16]. Some datasets (and Aladdin values) were multiplied by a convenient factor to make the data better fit into the figure.

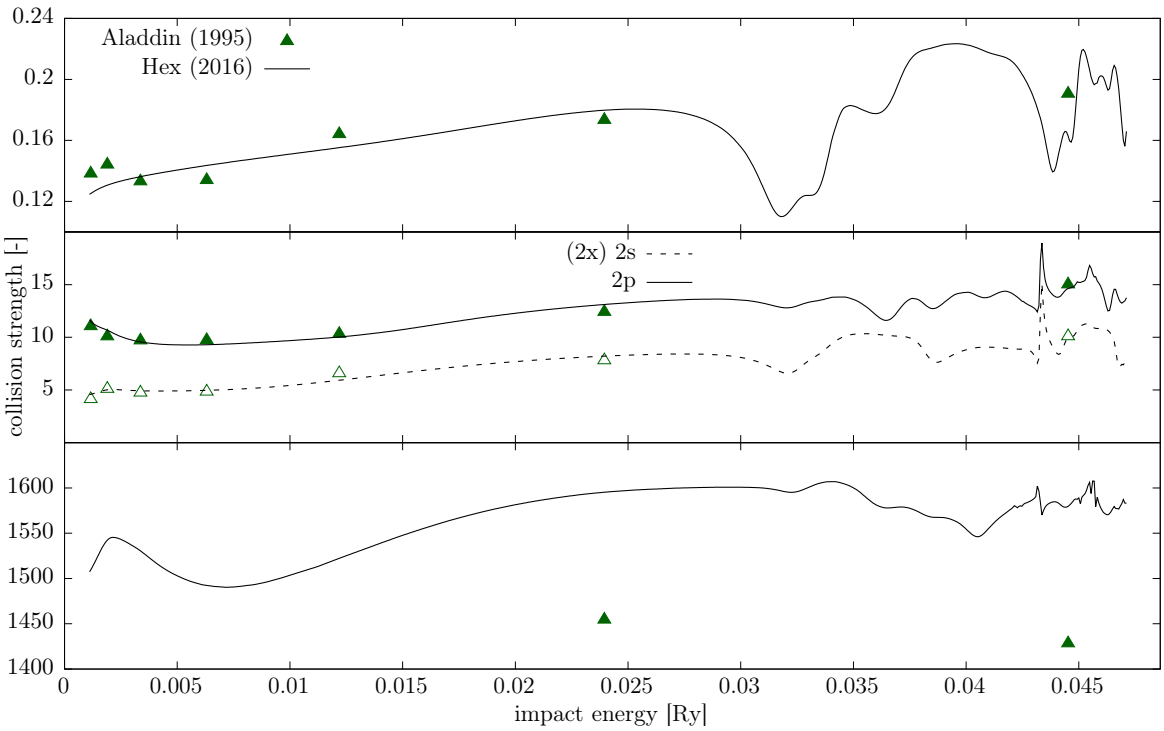

Figure 6.42: Collision strengths for processes from H($3p$) to H($1s$), H($2s$), H($2p$) and H($3p$) compared to the data from the database Aladdin [16]. Some datasets (and Aladdin values) were multiplied by a convenient factor to make the data better fit into the figure.

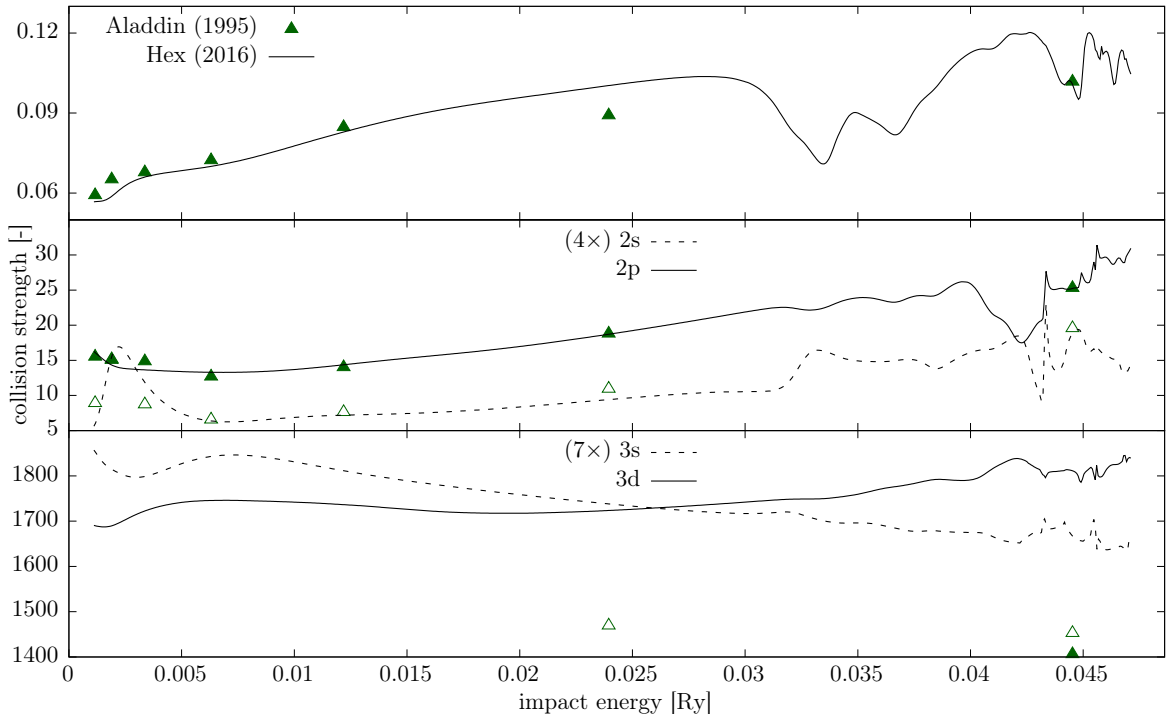

Figure 6.43: Collision strengths for processes from H($3d$) to H($1s$), H($2s$), H($2p$), H($3s$) and H($3d$) compared to the data from the database Aladdin [16]. Some datasets (and Aladdin values) were multiplied by a convenient factor to make the data better fit into the figure.

Chapter 7

Conclusion

This thesis summarizes a several-year-long endeavour to produce reliable and complete electron-hydrogen scattering data. Multiple methods have been tested, starting from the simple first Born approximation, then using the published codes of various kind—the R-matrix packages, semiclassical codes etc.—to the most accurate, but also most resource intesive *ab initio* methods like the exterior complex scaling or converged close coupling. Several million core hours have been spent to produce in total over fourty thousand data points. Fourteen initial and final states have been included and over 150 allowed transitions between these states for energy range from -1 Ry almost up to the ionization threshold.

The results have been checked by several ways: Where available, they have been compared to published data, both from earlier calculations by other researchers and from experiments. Also, theoretical constraints arising from the conservation of flux and from the detailed balance theorem were checked, to assure that the data are accurate within a few per cent. From the comparisons it can be concluded that the desired accuracy has likely been reached, sometimes leading to a significant improvement in contrast to the previously available data.

The so far obtained datasets are not complete; however, further calculations are underway and due to be published in the following years for the benefit of the plasma physics community. The author would also like to join the appropriate IAEA CRP to produce more data in cooperation with other plasma physics researchers.

Besides the results themselves the ECS code has been polished to a well usable form, so that any of the data can be independently recalculated, or even some new data can be added, e.g. for higher transitions, as soon as the computational technology sufficiently advances. The code is written in a very dynamic manner, there are just a few hard-coded constants and, as it is, it should allow for the solution of even much larger systems than used in this work, which is something that the other freely available codes often lack. This is a feature of the very robust ECS approach.

Further extensions of the method presented in this text is also envisioned. Namely, to charged hydrogen-like ions, so that similar datasets for e.g. He II [81] can be independently verified and extended, to partially shielded atoms for description of scattering in dense Debye plasmas [82], or to atoms with higher number of electrons (helium, lithium, etc.). Both the Kronecker product approximation preconditioner and the channel reduction method introduced in this work are promising tools to face the so-called "curse of dimensionality"—the exponential increase of computational work needed to solve higher-dimensional (many-electron) problems.

Appendices

Appendix A

Chebyshev integration

On several places in this thesis an integration or approximaton of an oscillating function is needed. A useful tool for this are the Chebyshev polynomials. Every function can be expanded in a basis of Chebyshev polynomials,

$$f(r) = \sum_{k=0}^{N} C_k T_k(t(r)) \ , \tag{A.1}$$

with the standard definition $T_n(t) = \cos(n \arccos(t))$. The polynomials are defined for $t \in \langle -1, 1 \rangle$, so first of all one has to compactify the interval of allowed coordinates r. A useful form of compactification of radial coordinates is the mapping

$$r(t) = L\frac{1+t}{1-t}, \qquad t \in \langle -1, 1 \rangle \to r \in \langle 0, +\infty \rangle \ , \tag{A.2}$$

$$t(r) = \frac{r-L}{r+L}, \qquad x \in \langle 0, +\infty \rangle \to t \in \langle -1, 1 \rangle \ . \tag{A.3}$$

The parameter L can be used to set the range of the compactification, i.e. which distances will be considered "far". The Chebyshev polynomial coefficients for the approximation of the function f defined on $\langle -1, 1 \rangle$ can be easily computed as [83]

$$C_j = \sum_{k=1}^{N-1} f(\cos(x_k)) T_j(j x_k), \qquad x_k = \pi \frac{k + \frac{1}{2}}{N} \tag{A.4}$$

due to the special orthogonality

$$\sum_{k=1}^{N} T_j(j x_k) T_{j'}(j x_k) = \delta_{jj'} \tag{A.5}$$

with x_k given in (A.4). The coefficients C_j for large index j with sufficient N decrease exponentially and thanks to the boundedness of the function value of the Chebyshev polynomials in the interval $\langle -1, 1 \rangle$ the magnitude of the last coefficient is a good measure of the approximation accuracy.

Evaluation of the integral, as all evaluations of any Chebyshev approximation in the code, is done by the fast *Clenshaw algorithm*, which is summarized in the figure A.1. Indefinite integral of the Chebyshev expansion can be written again as a Chebyshev expansion without any further loss of accuracy. Moreover, the expansion of the primitive function can be trivially derived from the original expansion, see e.g. [83]. The integration

by means of Chebyshev approximation is also called the (*first*) *Fejér quadrature*. It is not "nested", i.e. the evaluation points cannot be reused when the former evaluation point count is (e.g.) doubled. A modification exists, though, called the *Clenshaw-Curtis quadrature*, which can be nested in exchange for the necessity of evaluating the integrand at the end points. That can be numerically difficult like in the case of compactified functions. Nevertheless, in Hex the Clenshaw-Curtis quadrature has been used and actually reimplemented from scratch to enable integrating complex-valued functions as well.

The Clenshaw-Curtis (or second Fejér) quadrature is

$$\int_a^b f(x)\mathrm{d}x = (b-a)\left(\frac{1}{2}a_0 - \frac{a_2}{3} - \frac{a_4}{15} - \cdots - \frac{a_{2k}}{(2k)^2-1} - \cdots - \frac{1}{2}\frac{a_N}{N^2-1}\right) , \qquad \text{(A.6)}$$

with the coefficients

$$a_j = \frac{1}{2}(f(y_0) + (-1)^j f(y_N)) + \sum_{k=1}^{N-1} f(y_k)\cos(jk\pi/N) , \qquad y_k = \cos(k\pi/N) . \qquad \text{(A.7)}$$

There is N function evaluations in (A.7) and N^2 evaluations of the cosine function. For large N the cosine evaluation can be the bottleneck of the algorithm. Fortunately, the mapping $\{f(y_k)\} \to \{a_j\}$ in (A.7) is precisely the DCT-I (discrete cosine transform of the first kind), that can be implemented using the FFT (fast Fourier transform) algorithm by doubling the array and mirroring the samples $\{f(y_k)\}$ about $k = N$,

$$\textsc{dct-i}\,\{f_0, f_1, \ldots, f_{N-1}\} = \textsc{fft}\,\{f_0, f_1, \ldots, f_{N-1}, 0, f_{N-1}, \ldots, f_1\} . \qquad \text{(A.8)}$$

FFT has only $O(N \log N)$ time complexity, thus is much faster than $O(N^2)$. For computation of the fast Fourier transform the routines from GSL [68] are used. Very similarly, the computation of Chebyshev expansion coefficients (A.4), or in other form

$$C_j = \sum_{k=1}^{N-1} f(x_k)\cos\left(\pi j\left(k+\tfrac{1}{2}\right)/N\right) , \qquad x_k = \cos(\pi(k+\tfrac{1}{2})/N) , \qquad \text{(A.9)}$$

is, apart from the normalization factor of $2/N$, precisely DCT-II, the discrete cosine transform of the second kind, which can be, again, computed by FFT. The formula is now

$$\textsc{dct-ii}\,\{f_0, f_1, \ldots, f_{N-1}\} = \textsc{fft}\,\{0, f_0, 0, f_1, \ldots, 0, f_{N-1}, 0, f_{N-1}, \ldots, 0, f_0\} . \qquad \text{(A.10)}$$

Both in (A.8) and (A.10) only N leading samples are taken from the output of FFT; remaining chunks are mere reflections.

$d_{m+1} = d_m = 0$
for $j = m-1, m-2, \ldots, 1$
$\quad d_j = 2xd_{j+1} - d_{j+2} + c_j$
end
$f(x) = d_0 = xd_1 - d_2 + \frac{1}{2}c_0$

Figure A.1: Clenshaw's recurrent method adapted from [83] for evaluation of the function $f(x)$ given by its Chebyshev approximation $\{c_j\}$. The final index m can be equal to N or lower if the small trailing coefficients c_j fall below some limit.

Appendix B

Hex-ecs command line parameters

The program can be run from the command line and has many options that control the solution method and memory requirements. If the input file "*ecs.inp*" is present in the current working directory, it is sufficient to run the program without any arguments.

The input file contains all parameters that determine the solution. The command line options, on the contrary, control the way how the solution will be obtained.

- --help, -h : Displays a simple usage infromation.
- --example, -e : Creates a sample input file for a test calculation. This test run is suited for a common personal computer. The input file is full of comments that explain individual entries. It can be used to create other input files.
- --input *filename*, -i *filename* : Use the given file as the calculation input file. If this parameter is omitted, the filename "*ecs.inp*" is assumed and is searched for in the current working directory.
- --zip *filename xmin ymin xmax ymax xsamples ysamples*, -z ... : This will use the given B-spline expansion of the solution and produce a VTK surface (3D geometry) for visualization in ParaView.[1] Figures in this thesis come mostly from that program.
- --write-grid, -g : Write grid layout to a VTK file as a 2D mesh.
- --write-intermediate-solutions : After every finished iteration of the main PCOCG solver write the solution estimate to a disk file. These files have custom binary format, but can be converted to the universal HDF5 format using the utility hex-hdf2hdf.
- --stg-integ, -a : Execute only the first part of the whole solution process, i.e. calculate only the needed radial integrals.
- --stg-integ-solve, -b : Execute only the first two parts of the solution process, i.e. calculate only integrals and the solution.
- --stg-extract, -c : Execute only the third part of the solution process, i.e. extract only amplitudes. This option assumes that all needed solution files exist. If they do not, some data will be missing.

[1] VTK (*Visualization ToolKit*) and ParaView are open-source products of Kitware, Inc.

- --preconditioner *name*, -p *name* : Block preconditioner to use; default is ILU. Available preconditioners are: ILU (drop-tolerance incomplete LU factorization), KPA (Kronecker product approximation), GPU (essentially a KPA, run on OpenCL device; see below), HYB (combination of ILU and KPA for channel reduction mode; the former is used for angular states with non-zero number of asymptotic channels, the latter for the rest), DOM (domain decomposition).

- --list-preconditioners, -P : List available preconditioners with a short description of each. The availability of the preconditioners depends on the compile-time settings (available libraries etc.), so no all of them may be present in the binary.

- --tolerance *number*, -T *number* : Set tolerance for the conjugate gradients solver (default is 10^{-8}).

- --prec-tolerance *number*, -t *number* : Set tolerance for the conjugate gradients preconditioner (default is 10^{-8}).

- --drop-tolerance *number*, -d *number* : Set drop tolerance for the ILU preconditioner (default is 10^{-15}).

- --dom-x-panels *number* : Number of domain decomposition panels along the x-axis.

- --dom-y-panels *number* : Number of domain decomposition panels along the y-axis.

- --dom-preconditioner *name* : Preconditioner for solution on the sub-domain.

- --lu *name*, -F *name* : Factorization library to use, one of: lapack, umfpack, mumps, superlu and superlu_dist. Default is umfpack. Availability of the factorizers depends on the build options.

- --mumps-out-of-core : Use out-of-core mode for operation of the MUMPS LU decomposition library. Useful for large factorization.

- --mumps-verbose *number* : Verbosity level of the MUMPS LU decomposition library output, default is 0 and corresponds to no additional output.

- --fast-bessel : Use a faster (recurrent) formula for the Bessel functions when evaluating the right-hand side. If not used, the stable but slow Steed's formula is used.

- --channel-max-E *number* : Maximal energy (in Ry) of the states included in asymptotic expansion in the channel reduction mode.

- --mpi, -m : Use MPI, assuming that the program has been launched by mpiexec.

- --shared-scratch, -s : Assume a shared output directory for all processes of a MPI task. This will let every MPI process calculate only a subset of shared radial integrals and also prevent mutual overwriting of data by different processes of the task.

- --parallel-factorization : Factorize multiple blocks simultaneously. (One per OpenMP thread.)

- --no-parallel-extraction : Disallow parallel extraction of the T-matrices. This is useful when the whole solution does not fit into memory.

- --groupsize *number*, -G *number* : How many processes factorize single LU; only used for superlu_dist factorizer.
- --extract-rho-begin *number* : Distance where to start evaluating the scattering T-matrix.
- --extract-rho-end *number* : Distance where to end evaluating the scattering T-matrix.
- --extract-samples *number* : How many samples between the beginning and ending radius to evaluate when extracting the T-matrix.
- --extract-extrapolate : Use inverse power extrapolation instead of averaging of the samples.

The memory requirements of the program can be huge and it is often necessary to sacrifice some performance in exchange for memory saving. The tradeoff can be minimized by usage of fast storage, for example striped disk arrays (RAID 0) and/or solid state drives (SSD). The combination of RAID 0 and SSD has a throughput over 1 GiB/s, which is only about one order of magnitude slower than current RAM systems. The memory and storage requirements can be tuned by the following options:

- --own-radial-cache, -w : Keep two-electron radial integrals not referenced by the preconditioner only on disk (slows down only the initialization).
- --no-radial-cache, -r : Keep all two-electron radial integrals only on disk (slows down also the solution process).
- --out-of-core, -o : Use hard disk drive to store most of intermediate data and thus to save RAM (considerably slower).
- --out-of-core-continue, -O : Start solution from the existing intermediate files. This is only applicable if the previous solution has been run with the --out-of-core option, so that the files have been created.
- --whole-matrix, -W : In the above three cases: Always load the whole matrix from a scratch file when calculating dot products. In the absence of this option only small blocks are read. Application of this switch requires the matrix to fit in memory; however, it may speed up the calculation.
- --scratch *path* : Path to a directory, where all out-of-core data will be placed. When not set, but the environment variable `SCRATCHDIR` is defined, hex-ecs will use the path contained in that variable. Otherwise all out-of-core data will be written in the current working directory.
- --lightweight-full, -L : Avoid precalculating of all large matrices and only apply them on the fly. This is rather slow, but it allows huge systems to be solved.
- --kpa-simple-rad, -R : Use a simplified radial integral matrix for nested KPA iterations.

The program can be run on OpenCL platforms, for example on GPU units capable of double precision calculations. Successfully tested were graphical units with AMD Tahiti and NVidia Kepler chips and processors with Intel Haswell cores. GPUs are capable of achieving a high memory bandwidth, which speeds up the sparse matrix calculation, see the figure 4.11. Program options related to OpenCL are:

- --cl-list : List all OpenCL platforms and devices available.
- --cl-platform *index* : Use the given OpenCL platform for the GPU preconditioner.
- --cl-device *index* : Use the given OpenCL device for the GPU preconditioner.
- --cl-use-host-memory : Keep large data in RAM instead of copying everything to the compute device. This will slow down the solution on GPU.

If no OpenCL-related options are given and the GPU preconditioner is used, then the first device of the first platform will be used.

Appendix C

Hex-ecs input file

The input files are plain text files. Lines introduced by the hash symbol are comments for better orientation in the input data. Otherwise the division into separate lines is arbitrary; all data can be provided on a single line if desired. Only the order of the values (characters) matters. A sample input file is given below:

```
# B-spline order.
   4

# ECS rotation angle in radians.
   0.63

# B-spline knots.
# a) Real knots of the basis that is common to atomic and projectile electron.
  L  0.0  0.0   4
  G  0.1 10.0  0.1  1.01
  L   11  200  190
 -1
# b) Knots of the real grid extension used for channel reduction, if desired.
  L    0  800  801
 -1
# c) Complex region knots.
  G    0   50   1  1.02
 -1

# Initial atomic states (ni, li, mi).
  1  2  3  -1
  *  *  *
  *  *  *

# Final atomic states (nf, lf, *).
  0  1  2  3  -1
  *  *  *  *

# Maximal energy of states included in asymptotic expansion.
  -1

# Angular momenta.
# L    S    Pi   nL  limit exchange
  0    *    0    4   -1    1

# Projectile charge.
  -1

# Atom + projectile total energies in Rydbergs.
  E   0.1  0.2  0.5  1.0   -1
 -1

# Weak magnetic field in atomic units.
 0
```

The individual parameters are:

- B-spline order : A number that sets the degree of the B-spline basis. It has a huge impact on the sparseness of the resulting matrices. Typical values are 4 or 5. For the calculation of the data in this work the order equal to 4 has been used and this value is generally recommended.

- ECS rotation angle : This is the parameter that controls how much the grid will be rotated into the complex plane. Recommended value is $\pi/5$, the influence of this parameter is rather weak.

- B-spline knots : This is a crutial section that defines layout of the knots and in turn also the whole B-spline basis. Altogether there are three groups of knot sequences to specify: (a) the real knot sequence for the inner problem, (b) additional knots for the outer problem (channel reduction), and (c) the complex knots. Each of these groups of sequences can be composed from multiple sub-sequences; their list is terminated by "-1". The subsequences can be either linear sequences (introduced by "L", followed by the starting knot position, ending knot position and number of knots), geometric sequences (introduced by "G", followed by the starting knot position, ending knot position, initial distance between the knots and expansion ratio of the knot distances) or simple explicit list of knots (introduced by "E", followed by the individual knot positions and terminated by "-1"). The first sub-sequence within the group must always start with zero; it will be automatically shifted so that its first knot coincides with the last knot of the last sub-sequence from the preceding group, if any. In contrast, the sub-sequences within the group should not share any knots. The example above ultimately builds a sequence that starts with four zeros, then it geometrically expands up to $r = 10$ a.u. and from that radius it continues with uniform spacing up to $R_a = 200$ a.u. and $R_0 = 1000$ a.u., and then again continues with geometrically increasing spacing in the complex grid part up to $R_{\max} = 1050$ a.u.

- Initial atomic states : A list of initial principal quantum numbers of the target terminated by "-1", followed by a list of the initial orbital quantum numbers (of the same count) and magnetic quantum numbers. Altogether these data can be arranged into vertical triplets. If the asterisk symbol "*" is used for the orbital or magnetic quantum number then all possible values will be assumed.

- Final atomic states : As for the initial atomic states, but without magnetic quantum numbers (all allowed magnetic sublevel transitions will be extracted).

- Maximal energy of states included in asymptotic expansion : This limits the number of asymptotic states used for expansion of the calculated wave function in the outer region when using channel reduction approach. If "-1" is given, the program will use all energetically allowed states for given impact energy. This parameter is not used when no grid extension (knot sequence "(b)") is set.

- Total angular momentum, total spin (or both if "*" is used), total parity and n_L control the setup of the angular basis.

- The parameters "limit" and "exchange" offer a way of further constraining the full angular basis. In the presentation of the method in the section 4.1.1 the parameter "limit" is denoted by n'_L. When "limit" > -1 then all coupled angular momentum

pairs (ℓ_1, ℓ_2) with $\ell_1 >$ "limit" and $\ell_2 >$ "limit" are omitted from the basis. This is useful for high L, when only low values of ℓ_1 and ℓ_2 substantially contribute to the physics of the atom. The other parameter "exchange" can be set to 0 or 1. Whereas 1 is used for normal operation, setting to 0 will make the program discard all angular states where $\ell_2 > \ell_1$, effectively ignoring exchange effects. This is, again, very useful for reduction of the computational work in calculation of high partial waves.

- Projectile charge can be either -1 for the electron, or $+1$ for the positron. While the normal operation assumes electron projectile, it is possible to let the program flip the sign in the proper places and possibly turn off exchange effects for simulation of positron scattering on hydrogen atom. However, hex-ecs implements only a simple single-centre method, which makes the positron scattering results work only for extremely low energies.

- Total energies : Sequences that compose the list of total energies, for which to solve the equations.

- Magnetic field : It is possible to add a first-order external magnetic field contribution $\Delta E = (m_i - m_f)B$ to the energy of the scattered electron. This parameter specifies the strength of the magnetic field.

The output of the program is a few text files with the T-matrices and partial integral cross sections. Apart from that, it also produces several binary files in a custom format with the *.hdf* extension ("Hex data file"). This is not to be confused with the universal HDF5 ("Hiearchical data format rev. 5") storage. Nevertheless, a part of the Hex package is the utility hex-hdf2hdf that can be used to convert the former to the latter and back. The HDF5 format is not used directly by hex-ecs due to restrictions on parallel access to the data file.

Bibliography

[1] M. Karlický *et al.*, "Collisional excitation and ionization of hydrogen by return current in solar flares", *Astron. Astrophys.*, vol. 416, pp. L13–L16, 2004.

[2] B. Kučerová *et al.*, "Time-dependent spectral-feature variations of stars displaying the B[e] phenomenon", *Astron. Astrophys.*, vol. 554, A143, 2013.

[3] J. Štěpán and P. Heinzel, "Scattering polarization in solar flares", *Astroph. J.*, vol. 778, p. L6, 2013.

[4] R. M. Sainz *et al.*, "Depolarizing collisions with hydrogen: Neutral and singly ionized alkaline earths", *Astroph. J.*, vol. 788, p. 118, 2014.

[5] S. R. Furlanetto and M. R. Furlanetto, "Spin-exchange rates in electron-hydrogen collisions", *Mon. Not. R. Astron. Soc.*, vol. 374, pp. 547–555, 2007.

[6] G. M. McCracken *et al.*, "Evidence for volume recombination in JET detached divertor plasmas", *Nucl. Fusion*, vol. 38, p. 619, 1998.

[7] V. S. Lisitsa *et al.*, "Hydrogen Spectral Line Shape Formation in the SOL of Fusion Reactor Plasmas", *Atoms*, vol. 2, pp. 195–206, 2014.

[8] J. Callaway, "Scattering of electrons by hydrogen atoms", *Phys. Rev. A*, vol. 26, p. 119, 1982.

[9] ——, "Electron-impact excitation of hydrogen atoms: Energies between the $n = 3$ and $n = 4$ thresholds", *Phys. rev. a*, vol. 37, pp. 3692–3696, 1988.

[10] K. M. Aggarwal *et al.*, "Electron collision cross sections at low energies for all transitions between the $n = 1$, 2, 3, 4 and 5 levels of atomic hydrogen", *J. Phys. B: At. Mol. Opt. Phys.*, vol. 24, pp. 1384–1410, 1991.

[11] J. Callaway, "Effective collision strengths for hydrogen and hydrogen-like ions", *At. Data Nucl. Data Tables*, vol. 57, pp. 9–20, 1994.

[12] K. Bartschat, Ed., *Computational atomic physics*. Berlin Heidelberg: Springer-Verlag, 1996, ISBN: 3-540-60179-1.

[13] I. Bray and A. T. Stelbovics, "Convergent close-coupling calculations of electron-hydrogen scattering", *Phys. Rev. A*, vol. 46, pp. 6995–7011, 1992.

[14] H. Anderson *et al.*, "An R-matrix with pseudostates approach to the electron-impact excitation of H I for diagnostic applications in fusion plasmas", *J. Phys. B: At. Mol. Opt. Phys.*, vol. 33, p. 1255, 2000.

[15] P. L. Bartlett *et al.*, "Differential and integrated cross sections for excitation to the $3s$, $3p$, and $3d$ states of atomic hydrogen by electron impact below the $n = 4$ threshold", *Phys. Rev. A*, vol. 74, p. 022 714, 2006.

[16] I. Bray and A. T. Stelbovics, "Calculation of Electron Scattering on Hydrogenic Targets", *Adv. At. Mol. Opt. Phys.*, vol. 35, p. 209, 1995, (data from Aladdin database).

[17] ——, "Calculation of Electron Scattering on Hydrogenic Targets", *Adv. At. Mol. Opt. Phys.*, vol. 35, p. 209, 1995.

[18] (16th Jun. 2017). LXcat, CCC database, [Online]. Available: `https://nl.lxcat.net/home/`.

[19] (3rd Jan. 2017). NIST Electron-impact cross sections for ionization and excitation database, [Online]. Available: `https://www.nist.gov/pml/electron-impact-cross-sections-ionization-and-excitation-database`.

[20] Y.-K. Kim, "Scaling of plane-wave Born cross sections for electron-impact excitation of neutral atoms", *Phys. Rev. A*, vol. 64, p. 032 713, 2001.

[21] P. M. Stone, Y.-K. Kim and J. P. Desclaux, "Electron-impact cross sections for dipole- and spin-allowed excitations of hydrogen, helium, and lithium", *J. Res. Natl. Inst. Stand. Technol.*, vol. 107, p. 327, 2002.

[22] (3rd Jan. 2017). NIST Electron Elastic-Scattering Cross-Section Database, SRD 64, [Online]. Available: `https://srdata.nist.gov/SRD64/Elastic`.

[23] F. Salvat, A. Jablonski and C. J. Powell, "ELSEPA – Dirac partial-wave calculation of elastic scattering of electrons and positrons by atoms, positive ions and molecules", *Comput. Phys. Commun.*, vol. 165, pp. 157–190, 2005.

[24] E. D. Bloom *et al.*, "High-energy inelastic e-p scattering at 6° and 10°", *Phys. Rev. Lett.*, vol. 23, no. 16, pp. 930–934, 1969.

[25] R. Pohl *et al.*, "Laser spectroscopy of muonic deuterium", *Science*, vol. 353, pp. 669–673, 2016.

[26] H. A. Bethe and E. E. Salpeter, *Quantum mechanics of one- and two-electron atoms*. New York: Academic Press, 1957, ISBN: 978-0-486-46667-5.

[27] F. W. J. Olver, D. W. Lozier, R. F. Boisvert and C. W. Clark, Eds., *NIST Handbook of Mathematical Functions*. New York, NY: Cambridge University Press, 2010.

[28] J. Zamastil and J. Benda, *Kvantová mechanika a elecktrodynamika*. Praha: Karolinum, 2016, ISBN: 978-80-246-3223-0.

[29] M. J. Seaton, "Strong coupling in optically allowed atomic transitions produced by electron impact", *Proc. Phys. Soc.*, vol. 77, p. 199, 1961.

[30] M. Gailitis and R. Damburg, "Some features of the threshold behaviour of the cross sections for excitation of hydrogen by electrons due to the existence of a linear Stark effect in hydrogen", *J. Exptl. Theoret. Phys.*, vol. 44, pp. 1644–1649, 1963.

[31] A. S. Kadyrov *et al.*, "Asymptotic behaviour of the Coulomb three-body scattered wave", *Phys. Rev. A*, vol. 68, p. 022 703, 2003.

[32] I. Bray *et al.*, "Electron- and photon-impact atomic ionisation", *Phys. Rep.*, vol. 520, pp. 135–174, 2012.

[33] J. Benda, "Cross sections of collisions of electrons with hydrogen atoms", Master thesis, Prague, 2012.

[34] M. Owens and G. Allen, *The Definitive Guide to SQLite*, 2nd ed. Apress, 2010.

[35] M. L. Dubernet *et al.*, "The virtual atomic and molecular data centre (VAMDC) consortium", *J. Phys. B: At. Mol. Opt. Phys.*, vol. 49, p. 074 003, 2016.

[36] J. Benda and K. Houfek, "Collisions of electrons with hydrogen atoms II. Low-energy program using the method of the exterior complex scaling", *Comput. Phys. Commun.*, vol. 185, pp. 2903–2912, 2014.

[37] ——, "New version of hex-ecs, the B-spline implementation of exterior complex scaling method for solution of electron-hydrogen scattering", *Comput. Phys. Commun.*, vol. 204, pp. 216–217, 2016.

[38] W. McCurdy and F. Martín, "Implementation of exterior complex scaling in B-splines to solve atomic and molecular collision problems", *J. Phys. B: At. Mol. Opt. Phys.*, vol. 37, pp. 917–936, 2004.

[39] W. McCurdy, M. Baertschy and T. N. Rescigno, "Solving the three-body Coulomb breakup problem using exterior complex scaling", *J. Phys. B: At. Mol. Opt. Phys.*, vol. 37, R137–R187, 2004.

[40] P. Bartlett, "Complete numerical solution of electrons-hydrogen collisions", PhD thesis, Perth, 2006.

[41] J. Nuttall and H. L. Cohen, "Method of complex coordinates for three-body calculations above the breakup threshold", *Phys. Rev.*, vol. 188, pp. 1542–1544, 4 1969.

[42] R. Lazauskas, "Application of the complex scaling method in solving three-body Coulomb scattering problem", *J. Phys. B.: At. Mol. Opt. Phys*, vol. 50, p. 055 201, 2017.

[43] S. Cools and W. Vanroose, "A fast and robust computational method for the ionization cross sections of the driven Schrödinger equation using an $O(N)$ multigrid-based scheme", *J. Comput. Phys.*, vol. 308, pp. 20–39, 2016.

[44] C. de Boor, *A Practical Guide to Splines*. Springer-Verlag, 1978.

[45] H. Bachau *et al.*, *Applications of B-splines in atomic and molecular physics*. 2001, vol. 64, pp. 1815–1942.

[46] R. K. Peterkop, *Theory of ionization of atoms by electron impact*. Denver, CO: Colorado Associated University Press, 1977.

[47] H. A. van der Vorst and J. B. M. Melissen, "A Petrov-Galerkin type method for solving $Ax = b$, where A is symmetric complex", *IEEE Trans. Magn.*, vol. 26, no. 2, 1990.

[48] J. R. Shewchuk, *An introduction to the conjugate gradient method without the agonizing pain*. Pittsburgh, PA: Carnegie Mellon University, 1994.

[49] M. Baertschy *et al.*, "Electron-impact ionization of atomic hydrogen", *Phys. Rev. A*, vol. 63, p. 022 712, 2000.

[50] P. Amestoy, I. Duff, J.-Y. L'Excellent and J. Koster, "MUMPS: A General Purpose Distributed Memory Sparse Solver", in *Applied Parallel Computing. New Paradigms for HPC in Industry and Academia*, ser. Lecture Notes in Computer Science, T. Sørevik, F. Manne, A. Gebremedhin and R. Moe, Eds., vol. 1947, Springer Berlin Heidelberg, 2001, pp. 121–130.

[51] C. G. Petra, O. Schenk, M. Lubin and K. Gärtner, "An augmented incomplete factorization approach for computing the Schur complement in stochastic optimization", *SIAM Journal on Scientific Computing*, vol. 36, no. 2, pp. C139–C162, 2014.

[52] T. A. Davis, "Algorithm 832: UMFPACK, an unsymmetric-pattern multifrontal method", *ACM Trans. Math. Softw.*, vol. 30, pp. 196–199, 2004.

[53] X. S. Li, "An overview of SuperLU: Algorithms, implementation, and user interface", *ACM Trans. Math. Softw.*, vol. 31, no. 3, pp. 302–325, 2005.

[54] X. S. Li and J. W. Demmel, "SuperLU_DIST: A scalable distributed-memory sparse direct solver for unsymmetric linear systems", *ACM Trans. Math. Softw.*, vol. 29, no. 2, pp. 110–140, 2003.

[55] I. Bar-On, Å. Edlund and U. Peskin, "Parallel solution of the multidimensional Helmholtz / Schroedinger equation using high order methods", *Appl. Num. Math.*, vol. 33, pp. 95–104, 2000.

[56] R. E. Plessix and W. A. Mulder, "Separation-of-variables as a preconditioner for an iterative Helmholtz solver", *Appl. Numer. Math.*, vol. 44, pp. 385–400, 2003.

[57] Z. Xianyi, W. Qian, Z. Yunquan and Q. Yi, "AUGEM: Automatically Generate High Performance Dense Linear Algebra Kernels on x86 CPUs", *International Conference for High Performance Computing, Networking, Storage and Analysis*, Nov. 2013.

[58] E. Yarevsky *et al.*, "Potential-splitting approach applied to the Temkin-Poet model for electron scattering off the hydrogen atom and the helium ion", *J. Phys. B: At. Mol. Opt. Phys.*, vol. 48, p. 115 002, 2015.

[59] M. V. Volkov *et al.*, "Potential splitting approach to the three-body Coulomb scattering problem", *Europhys. Lett.*, vol. 110, p. 30 006, 2015.

[60] E. Yarevsky, S. L. Yakovlev and N. Elander, "Potential splitting approach to e–H and e–He^+ scattering", *J. Phys. B: At. Mol. Opt. Phys.*, vol. 50, p. 055 001, 2017.

[61] J. Benda and K. Houfek, "Reducing the dimensionality of grid based methods for electron-atom scattering calculations below ionization threshold", *Comput. Phys. Commun.*, vol. 213, pp. 46–51, 2017.

[62] C. C. Stolk, "A rapidly converging domain decompostion method for the Helmholtz equation", *J. Comput. Phys.*, vol. 241, pp. 240–252, 2013.

[63] A. N. Grum-Grzhimailo, "MJK: A program to calculate observable quantities in electron-atom collisions", *Comput. Phys. Commun.*, vol. 152, 2003.

[64] K. A. Berrington, W. B. Eissner and P. H. Norrington, "RMATRX1: Belfast atomic R-matrix codes", *Comput. Phys. Commun.*, vol. 92, p. 290, 1995.

[65] J. Benda and K. Houfek, "Collisions of electrons with hydrogen atoms I. Package outline and high energy code", *Comput. Phys. Commun.*, vol. 185, pp. 2893–2902, 2014. [Online]. Available: `http://utf.mff.cuni.cz/data/hex`.

[66] I. S. Gradhsteyn and I. M. Ryzhik, *Table of integrals, series and products*, 7th ed. Elsevier Academic Press, 2007.

[67] G. W. F. Drake, Ed., *Springer handbook of atomic, molecular, and optical physics*. Springer, 2006.

[68] M. Galassi *et al.*, *GNU Scientific Library Reference Manual*, 3rd ed. Network Theory Ltd., 2009.

[69] H. Akima, "A new method of interpolation and smooth curve fitting based on local procedures", *J. ACM*, vol. 17, pp. 589–602, 1970.

[70] M. Gailitis and R. Damburg, "The influence of close coupling on the threshold behaviour of cross sections of electron-hydrogen scattering", *Proc. Phys. Soc.*, vol. 82, p. 192, 1963.

[71] A. K. Bhatia, "Hybrid theory of electron-hydrogen elastic scattering", *Phys. Rev. A*, vol. 75, p. 032 713, 2007.

[72] I. Bray, "Convergent close-coupling method for the calculation of electron scattering on hydrogenlike targets", *Phys. Rev. A*, vol. 49, pp. 1066–1082, 1994.

[73] G. J. Schultz, "Resonances in electron impact on atoms", *Rev. Mod. Phys.*, vol. 45, pp. 378–422, 1973.

[74] A. Bürgers and E. Lindroth, "Doubly excited states in the negative hydrogen ion", *Eur. Phys. J. D*, vol. 10, pp. 327–340, 2000.

[75] A. Pathak, A. E. Kingston and K. A. Berrington, "Resonances in H^- associated with the $n = 2$, 3 and 4 hydrogenic thresholds", *J. Phys. B: At. Mol. Opt. Phys.*, vol. 21, pp. 2939–2951, 1988.

[76] M. Bylicki and C. A. Nicolaides, "Theoretical resolution of the H^- resonance spectrum up to the $n = 5$ threshold: States of $^3P^o$ symmetry", *Phys. Rev. A*, vol. 65, p. 012 504, 2001.

[77] M. Biaye *et al.*, "The doubly excited states description of the negative hydrogen ion using special forms of the Hylleraas type wave functions", *Chin. J. Phys.*, vol. 47, pp. 166–172, 2009.

[78] J. Benda and K. Houfek, "Converged and consistent high-resolution low-energy electron-hydrogen scattering. I. Data below n = 4 threshold for applications in stellar physics", *At. Data Nucl. Data Tables*, vol. 117?, ?–?, 2017.

[79] T. T. Scholtz *et al.*, "Effective collision strengths for $1s - 2s$ and $1s - 2p$ electron-hydrogen atom scattering", *Mon. Not. R. astr. Soc.*, vol. 242, pp. 692–697, 1990.

[80] J. F. Williams, "Resonance structure in inelastic scattering of electrons from atomic hydrogen", *J. Phys. B: At., Mol. Opt. Phys.*, vol. 21, p. 2107, 1988.

[81] K. M. Aggarwal *et al.*, "Radiative Rates and Electron Impact Excitation Rates for Transitions in He II", *Atoms*, vol. 5, 2 2017.

[82] J. Li *et al.*, "Low energy electron-impact ionization of hydrogen atom for coplanar equal-energy-sharing kinematics in Debye plasmas", *Plasma phys.*, vol. 23, 2016.

[83] W. H. Press *et al.*, *Numerical recipes*, 3rd ed. Cambridge university press, 2007.

Index

angle
  Euler, 22
  scattering, 19, 76

boundary condition, 24, 27, 36, 40

channel
  forbidden, 53
  scattering, 55
Clebsch-Gordan coeffcients, 22
Clenshaw algorithm, 99
collision strength, 67
computer program, 28
conjugate gradients, 42
conservation
  of energy, 29
  of parity, 34
Coulomb wave, 41
cross section, 19, 27
  differential, 19, 76
curse of dimensionality, 95

database, 15, 28, 67
degeneracy
  accidental, 23
deuterium, 17
discrete cosine transform, 100
domain decomposition, 55

electromagnetism, 57
equation
  Helmholtz, 19, 47
  Schrödinger, 14, 23, 33

floating-point operations, 44
flux
  of probability, 60

hamiltonian, 18

interpolation, 66

Jacobi coordinates, 24

length
  scattering, 68
LU decomposition, 42, 44

magnetic quantum number, 22
mass polarization, 18
matrix
  T-matrix, 19, 27
  banded, 42
  block structure, 34
  of tensor product, 42
method
  CCC, 15
  ECS, 15, 36
  R-matrix, 15
model
  Temkin-Poet, 68

plasma, 13
polarizability, 18
polynomial
  Laguerre, 18
potential
  multipole, 23, 36, 47
preconditioning, 44
principal quantum number, 18
process communication, 47
proton, 18

quadrature
  Clenshaw-Curtis, 64, 100
  Fejér, 100
  Gauss-Legendre, 39
quantization axis, 22

relativistic effects, 17, 22
resonance, 46, 70
  Feshbach, 70
Rydberg state, 13

S-matrix, 71
S-model, 48

scattering amplitude, 19
solar flare, 13
solver
    iterative, 55
spectroscopical notation, 22
spherical harmonics, 18, 33
spin, 20
    averaging, 21
    polarization, 22
    total, 21
spin singlet, 20
spin triplet, 20
spin-flip, 13
spline
    Akima, 66
    B-spline, 33, 36
state
    parent, 70
surface integral, 41

theorem
    detailed balance, 65, 71
    optical, 65, 72
thermonuclear fusion, 13
threshold
    excitation, 53, 55, 76
    ionization, 55, 76
transition
    dipole-allowed, 65

unitarity, 71

vector
    Runge-Lenz, 23

wave
    partial, 67, 76
wave function, 18
    antisymmetry, 20
    as complex field, 48
    in continuum, 18
Wigner 3j symbol, 34
Wigner matrix, 22